NORTHWESTERN UNIVERSITY

Simulation and Experimental Realization of Novel High Efficiency All-Optical and Electrically Pumped Nanophotonic Devices

A DISSERTATION

SUBMITTED TO THE GRADUATE SCHOOL
IN PARTIAL FULFILLMENT OF THE REQUIREMENTS

for the degree

DOCTOR OF PHILOSOPHY

Field of Electrical and Computer Engineering

By

Yingyan Huang

EVANSTON, ILLINOIS

June 2007

ABSTRACT

Simulation and Experimental Realization of Novel High Efficiency All-Optical and Electrically Pumped Nanophotonic Devices

Yingyan Huang

Next generation of high performance nano-optoelectronic integrated circuits will require an integral combination of highly efficient all-optical nanophotonic devices and electrically-pumped nanophotonic devices, which will enable the chip to process optical information all optically with ultrafast speed and electro-optically to interface with the electronic control plane. The realizations of such nano-OEIC still face various challenges, including: (1) the lack of integratable ultrafast all-optical devices; (2) The lack of efficient way to couple light from optical fiber into such nano-OEIC; (3) The lack of microlaser design that can be easily integrated to provide useful optical power; (4) The lack of sophisticated simulator for semiconductor nano-optoelectronic devices. This dissertation explores solutions to these challenges.

Firstly, current all-optical devices are often large in size and high in operating powers, making them unsuitable for integration. We propose a novel way of using gain and absorption

manipulation of optical interference (GAMOI) to realize integratable low-power all-optical photonic transistor type devices. Exemplary devices illustrate two complementary device types with high operating speed, micron size, and microwatt switching power. They can act in tandem to provide switching gain, wavelength conversion, pulse regeneration, and logical operations. These devices could have a Transistor Figure of Merits >100,000 times higher than $n^{(2)}$ approaches.

Secondly, we proposed a solution for light coupling between nanophotonic waveguide to optical fiber: a super-high numerical aperture gradient index (Super-GRIN) micro lens made from multiple nanolayers of two or more materials with large refractive index contrast. Super-GRIN lens with NA>1.5 and length<20micron was realized with thin-film deposition technique.

Thirdly, we show the first semiconductor laser using novel micro-loop mirror as end reflector to achieve ultra-compact laser size, which leads to higher output power and ease of integration with nanophotonic waveguides. We present the simulation and fabrication result for this microlaser with cavity length as small as 25micron with low lasing threshold of ~0.4 mA.

Fourthly, we introduce the first computational model of solid-state, molecular, atomic media for Finite Difference Time Domain simulation based on multi-level multi-electron system governed by Pauli Exclusion and Fermi-Dirac thermalization. We illustrated the advantages of the model for simulating semiconductor nano-optoelectronic devices.

ACKNOWLEDGMENT

I would like to thank, first and foremost, my advisor, Dr. Seng-Tiong Ho, for his guidance and support throughout my PhD study at Northwestern and during the completion of this dissertation. I have learned a great deal from his technical expertise. Moreover, I have realized the intricacies of conducting successful research and it has been a pleasure to be a member of his group.

I would like to thank the past and present members of the Ho groups. Dr. Songsik Chang for helping me to get my feet wet in FDTD simulation. He provided me with the initial version of the FDTD code with 4-level 2-electron model, which I could then work on and build the current multi-level multi-electron model. Dr. Guoyang Xu, who taught me how to process. He never hesitates to share with me his invaluable fabrication experience from many years of great work. Dr. Yegao Xiao for collaborating on the fabrication of the micro-loop mirror laser. Dr. Yiguang Zhao for helping on the measurement of the micro-loop mirror laser. Dr. Bo Liu for helping on the ultra fast optical measurement of the quantum well intermixed waveguides. Dr. Jing Ma for valuable discussions and being a good friend. Boyang Liu for helping me on so many aspects of the project, big and small, I cannot even count. And I would like to thank all past and present member of Dr. Ho's group, for making my life in Northwestern memorable and wonderful.

I would like to thank Dr. Boon Soo Ooi from Lehigh University for his invaluable advices and helps on the quantum well intermixing. I would also like to thank Dr. Yan Zhou and Dr. Shide Cheng from Phosistor Inc. for insightful discussions on the super high numerical aperture GRIN lens simulation.

As anyone who has done device processing would understand, the work in this dissertation will not be possible without the support from the staffs in various cleanrooms. They include the material research center cleanroom at Northwestern University, Prof. Ho's group's cleanroom, the nanotechnology core facility at University of Illinois at Chicago, the micro and nanotechnology laboratory at University of Illinois at Urbana-Champagne. This work was also performed in part at the Cornell Nanofabrication Facility, a member of the National Nanotechnology Infrastructure Network, which is supported by the National Science Foundation (Grant ECS 03-35765).

The work in this document was funded by NSF under Award No. ECS-0501589, by NSF MRSEC program under grant DMR-0076097, MRSEC Graduate Fellowship, and by the NASA Institute for Nanoelectronics and Computing under Award No. NCC 2-1363.

Last, but not the least, I would like to thank my parents Kejun and Weiyi, and my husband Peng for their unwavering support in all that I do. This truly would not have been possible without them.

TABLE OF CONTENTS

LIST OF TABLES

LIST OF FIGURES

Fig. 5.4 FDTD simulation of MLM-WGM laser: (a) device structure, where the light gray part is bandgap shifted to transparency for lasing wavelength and dark gray part is not bandgap shifted; (b) electromagnetic field pattern of MLM-WGM laser when lasing; (c) plot for output power vs. current.

Fig. 5.5 (a) Schematic diagram of the bandgap at different sections of the fabricated micro loop mirror laser. (b) PL result for the quantum well wafer before and after quantum well intermixing measured at room temperature.

Fig. 5.6. SEM picture of the ICP etched looped mirror laser.

Fig. 5.7. Schematic diagram of the laser cross-section in areas with contacts

Fig. 5.8. Experiment curve for output power vs. current for the micro loop laser and lasing spectrum measured by fiber spectrometer with 5nm resolution.

Fig. 6.1 (a) The parabolic refractive index profile (dashed line) of a 13μm thick GRIN lens and the approximate step refractive index profile of a SUPER-GRIN lens (solid line), (b) TiO_2 and SiO_2 layers (solid line) used to approximate a certain step refractive index (dashed line).

Fig. 6.2 (a) Layer structure used in estimation of the scattering loss using transfer matrix method. (b) Total scattering loss calculated by transfer matrix method for three total structure thickness: 3μm (straight line), 5μm (dotted line), and 7μm (dashed-dotted line).

Fig. 6.3 FDTD simulated field pattern for fiber mode propagating inside lenses (vertical size (V) 13μm, horizontal size (H) 25μm), (a) TE light (E field) in the continuous index GRIN lens, (b) TE light (E field) in the SUPER-GRIN lens with TiO_2 / SiO_2, (c) TM light (H field) in the

SUPER-GRIN lens with TiO_2 / SiO_2, (d) mode profile at the focusing point of the SUPER-GRIN lens and continuous GRIN lens, compared to mode profile of the matched III-V waveguide (core thickness 1.1μm, core / cladding refractive index 3 / 2.8).

Fig. 6.4 Focusing in SUPER-GRIN lens from optical fiber mode to III-V waveguide with air gap and AR coating, (a) structure, (b) FDTD simulated TE light E-field pattern (V×H=13μm×28μm).

Fig. 6.5 FDTD simulation of a SUPER-GRIN lens with n_R=1.45 and n_0=2.17. (a) Simulated TE light E-field pattern (V×H=13μm×22μm) showing optical fiber mode focused to 0.5μm III-V waveguide (core/cladding refractive index 3.35 / 3.2, core thickness 0.5μm). (b) Mode profile at the focusing point of the SUPER-GRIN lens and continuous GRIN lens, compared to mode profile of the matched III-V waveguide.

CHAPTER I INTRODUCTION

1.1 Motivation

While electronic devices are getting smaller and faster via the advancements in nanoscale electronics, they eventually will meet a bottleneck in terms of communications speed among transistors and across chips. The main advantage of photonics is its tremendous communications bandwidth and its lowloss optical transmission media enabling much larger bandwidth of data transfer (lowloss comparing to high-frequency RF transmission lines whose loss scales up quickly with frequency). It is envisioned that future chips will require a combination of electronic and photonic devices to take advantage of both the tremendous processing speed of electronics and the tremendous communication bandwidth of photonics. The recent advancements in nanophotonic devices have made such combination potentially possible, resulting in nanoscale optoelectronic integrated circuits (nano-OEICs) with enhanced functionalities.

However, in spite of the potential promise of nano-OEICs, many challenges still have to be overcome in terms of realizing the key nanophotonic or nano-optoelectronic components that could provide the functionalities needed with low enough operating power so that they can be efficiently integrated. The main focus of this dissertation is to address some of these challenges

in four inter-related areas of interest by recognizing that: (1) Such nano-OEIC will require all-optical devices on chip that can be used to process ultrafast optical pulses through switching or logical operations without converting them to electrical signals (and back to optical). This is because such electrical-to-optical (EO) or optical-to-electrical (OE) conversions can consume a lot of power. Currently, there are no viable all-optical devices that can be conveniently integrated. As discussed below, current all-optical devices are either too big in size or require very high peak optical power to operate; (2) Such nano-OEIC will require an efficient way to couple light in and out of the chip. While several schemes are available currently, they are still not ideal in terms of providing practical solutions; (3) Such nano-OEIC shall involve efficient laser light sources. While some nano or micro lasers have been demonstrated, their efficient integration on the chip to provide useful output powers into waveguides has yet to work out; (4) Such nano-OEIC shall require more sophisticated design and simulation of nanophotonic and nano-optoelectronic devices that can simulate both semiconductor based all-optical devices and electrically-pumped devices with reasonable precision.

In this dissertation, we will address these four main challenge areas by exploring innovative approaches that we believe will bring significant advancements in these areas. They include:

(1) **GAMOI Photonic Transistors**. A class of novel all-optical transistor devices based on a new approach of using optically-controlled gain and absorption to change optical interference resulting in efficient all-optical switching action with very low operating power and switching gain. We show that this class of device can be seen as close analogue of transistors for photons that can be used to provide a wide variety of all-optical operations including all-optical

switching, wavelength conversion, and logical operations. The device sizes are small, with device area of tens of square micrometers and high operating speed of 10-100Gb/s (or higher depending on design). This class of photonic transistors is referred to as GAMOI Photonic Transistors (GAMOI stands for Gain and Absorption Manipulation of Optical Interference).

(2) **Super-GRIN Optical Couplers.** A microscopic Graded-Refractive-Index (GRIN) lens with very high focusing power that can be fabricated directly on chip using deposition technique that will enable easy coupling of light beam from optical fibers into sub-micrometer waveguides. We refer to it as a Super-GRIN lens. The lens is amenable to precision fabrication process that can be used to correct for beam or wavefront distortion, and can achieved numerical aperture substantially higher than unity. It is based on a multi nano-layer thin-film deposition technique with only two different materials layer making it easy to manufacture.

(3) **Integratable Loop-Mirror Nanolasers.** Nanolasers or microlaser that can be more easily integrated with on-chip waveguides to provide the optical beam power needed to power various all-optical devices on the wafer. They can also be integrated with modulators for ultrafast data transfer. One type of microlaser we explore here has a linear microcavity with single-sided output. The single-sided output will increase the output power by two times compared to ring cavities with bi-directional outputs. To realize a linear cavity, a micro-size loop mirror is used as the end reflectors for the laser.

(4) **Dynamical-Semiconductor-Medium FDTD Nanophotonic Device Simulator.** A general computational model of complex material media for electrodynamics simulation using the Finite-Difference Time-Domain (FDTD) method that can be used to simulate semiconductor

materials for the first time. It is based on a multi-level multi-electron quantum system with electron dynamics governed by Pauli Exclusion Principle, state filling, and dynamical Fermi-Dirac Thermalization, enabling it to treat various solid-state, molecular, or atomic media. The formulation is valid at near or far off resonance as well as at high intensity. It can be applied to semiconductor in which the carriers' intraband and interband dynamics, energy band filling, and thermal processes can be all included in the model. The FDTD model is sufficiently complex and yet computationally efficient, enabling it to simulate all-optical or electrically pumped semiconductor nanophotonic devices with complex electromagnetic structures requiring simultaneous solution of the medium field dynamics in space and time.

With the above new developments, they can be applied to the realizations of various nano-OEICs with new functionalities. An exemplary application will be the realization of a nano-OEIC that can function as a fully integrated highly-efficient all-optical transistor device with integrated laser power source. Such an integrated nano-OEIC chip is shown schematically in Figure 1.1, showing a photonic transistor powered by two electrically-pumped integrated microlasers emitting continuous-wave laser beams. The chip has an optical input and an optical output ports with light coupled to optical fibers through integrated super-GRIN lenses. This nano-OEIC functions as an all-optical chip capable of processing ultrafast optical signals in the optical domain without OE-EO conversions.

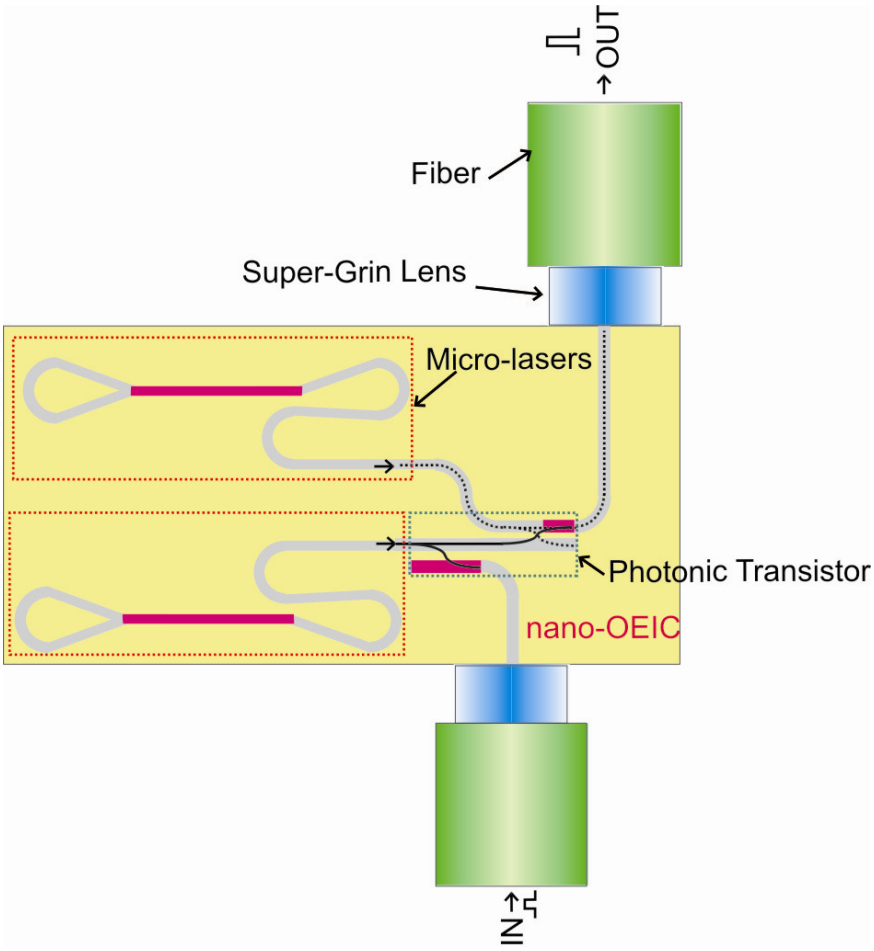

Fig. 1.1 a nanoscale optoelectronic integrated circuit (nano-OEIC) with nanophotonic component connecting to optical fiber.

1.2 Outline of the Dissertation

The work of this dissertation began with the idea of a new scheme for constructing semiconductor based all-optical switch with low power consumption (hopefully within several mW so on chip semiconductor lasers can be used), high switching speed of 10-100GHz and small footprint. The all-optical switch uses gain and absorption modification in semiconductor

material in combination with a directional coupler structure to change the optical interference. It was found that the all-optical switch can achieve switching gain and have linear or saturation regime, which make it to be an optical analogue of a transistor and can be called a photonic transistor. Along the way of exploring the photonic transistor, it turns out that in order to better study the coupling between electromagnetic field with the carrier dynamics in the active medium, it is necessary to have new simulation models to be used in conjunction with the finite difference time domain method, and in order to reach the final goal of constructing a complete nano-OEIC using such all-optical switch, we also studied other supplementary devices. For example, a new type of edge-emitting laser with micro-scale waveguide loop mirror is simulated and fabricated to be a potential candidate for on-chip optical power supply. A super high numerical aperture lens scheme is proposed and simulated, to offer a solution for chip to fiber connection. An ultra-compact optical mode order converter capable of converting zero and 1^{st} order optical mode is also simulated and fabricated, which can be used to increase the efficiency of the photonic transistors.

The dissertation is presented in the following manner:

We start with the definition of nanophotonic devices in Chapter II. The main advantages of nanophotonic devices compared to conventional structures are discussed. We then group the nanophotonic semiconductor devices into two main categories based on the scheme of vertical optical confinement: the tall structure and the thin-film structure. By tall structure we refer to those devices that the vertical optical confinement is provided by the refractive index difference between different types of semiconductor materials. By thin-film structure we refer to those devices that the vertical optical confinement is provided by the refractive index difference

between semiconductor materials and other types of low refractive index materials, such as SiO_2 (n~1.45), air (n~1), or BCB (n~1.53). Their pros and cons are discussed. We then introduce some typical fabrication techniques used in this dissertation. We first introduce the quantum well intermixing technique for passive and active area integration. We then discuss the BCB assisted thin-film wafer bonding technique used in fabrication of thin-film nanophotonic devices. Lastly, we summarize the typical fabrication steps for both the tall structures and the thin-film structures.

In chapter III we introduce a multilevel semiconductor model for FDTD simulation of electrically pumped and all-optical nanophotonic devices. We first discuss the essential structure of the multi-level multi-electron model for FDTD simulation of nanophotonic devices. The medium is described by a set of rate equations derived quantum mechanically. The formulation is based on the basic minimal-coupling Hamiltonian extended to incorporate multiple electrons via second quantization using Fermion creation and annihilation operators. The set of rate equations and dipole equation describing the model are obtained without the usual rotating-wave approximations and can be applied to the regimes at near or far off-resonance as well as high field intensity. The multi-electron system is then included into the equations and proper ways to calculate the medium number density for different semiconductor material is covered. Ways to include Fermi-Dirac thermalization is discussed and detailed equation for FDTD implementation of the model is listed. Lastly we showed several simulation examples using the proposed model, which include the band-filling effect of semiconductor, the decay of non-thermal equilibrium carrier distributions, and the coupling between optical field and carrier distribution for a microdisk semiconductor laser. This simulator is thus capable of simulating semiconductor medium dynamically and is referred to as Dynamical-Semiconductor-Medium FDTD (DSM-

FDTD). This part is a collaborative work with Dr. Seng-Tiong Ho, who has contributed on the derivation of the quantum mechanical equations.

In Chapter IV, we address the theory and simulation of the all optical photonic transistor device based on gain and absorption manipulation of optical interference. We first discuss the definition of a photonic transistor and its analogy to an electronic transistor. We show the limitation of optical switch scheme using $n^{(2)}$ and the power advantages of $\alpha^{(2)}$. We then introduce the basic principle of using the manipulation of $\alpha^{(2)}$ in optical interference structure to construct photonic transistors. The GAMOI based photonic transistor device in a direction coupler form is then simulated in details. First we show the idea case of using a 4-level 2-electron model to model the active material. The basic operation principles of the photonic transistors are illustrated and the main advantages are discussed. Exemplary devices illustrate two complementary device types with high operating speed, μm size, and μW switching power. They can act in tandem to provide a wide variety of operations including switching gain, wavelength conversion, pulse regeneration, and logical operations. We then used the more sophisticated 10-level semiconductor model to study the realistic implementation of the devices using III-V semiconductor materials. These devices could have a Transistor Figure of Merits $>10^5$ times higher than $\chi^{(3)}$ approaches and are highly attractive. Initial measurement result showing the saturation and pump-probe experiment result in semiconductor waveguide is also included. Finally in order to achieve the optimal performance of the GAMOI based photonic transistors it is necessary to use a combination of 1st order mode and 0th order mode in the optical coupler. We present an ultra compact mode converter capable of the easy conversion between 0 and 1st order mode using sub micron optical waveguide. The design theory of the

mode converter is discussed. The simulation result and the fabrication result of such mode converter are also presented. This part is a collaborative work with Dr. Seng-Tiong Ho.

For the power supply of the nano-OEIC, a novel type of linear-geometry micro-cavity laser is introduced in Chapter V. The laser uses nano-scale waveguide loops as end reflectors to achieve single directional output. The compact size and high reflectivity of the micro-loop mirror allows ultra-compact laser size, which leads to potential single mode operation. The design principle of the micro-loop mirrors is discussed. FDTD simulation is used to optimize the design of the mirror so maximum reflectivity can be achieved with minimal cavity length. The lasing behavior of the micro-loop mirror laser is also studied by using our dynamical-semiconductor-medium FDTD simulation. We then describe the main fabrication steps of the laser and present the measurement result. We show that microlaser with cavity length as small as 25μm can be achieved with low lasing threshold of ~0.4 mA. Method to obtain higher output power from the microlaser with widened gain medium is discussed. This part is a collaborative work with Dr. Yegao Xiao, Dr. Guoyang Xu, Dr. Seongsik Chang, Dr. Yiguan Zhao, Ruyu Wang, Dr. Boon Soo Ooi, and Dr. Seng-Tiong Ho.

One potential solution for the chip to optical fiber coupling is presented in Chapter VI. We describe a super-high numerical aperture gradient refractive index (Super-GRIN) lens scheme using multiple thin layers of two or more materials with large refractive index contrast. The Super-GRIN lens could facilitate the coupling from nanophotonic devices to conventional optical stricture such as single mode fibers. We first introduce the basic design theory of the Super-GRIN lens. We then give the specific examples of the Super-GRIN lens with SiO_2 and TiO_2 material system designed for fiber coupling to nano-waveguide. The loss from the lens is

estimated using transfer matrix methods and the results is compared to direct FDTD simulation. It is shown that for fiber mode to nano-waveguide focusing applications, to have focusing FWHM spot sizes of 0.53/0.7 μm at λ = 1.55 μm (corresponding to NA ~ 1.6/1.1), the Super-GRIN lens will only introduce 2.7/2.4% additional loss comparing to ideal continuous index profile GRIN lenses. Using the approach, Super-GRIN lens with NA>1.5 and length<20μm can be realized with current thin-film deposition technique. This part is a collaborative work with Dr. Seng-Tiong Ho.

Finally, In Chapter VII, we summarize the work of the dissertation and point out some possible directions for future research work.

Portions of this work have appeared in journal form in (Huang et al. 2006 [1]; Huang et al. 2006 [2]; Huang et al. 2006 [3]; Huang et al. 2005 [4]) and conference form in (Huang et al. 2006 [5]; Huang et al. 2006 [6]; Huang et al. 2005 [7]; Huang et al. 2005 [8]; Huang et al. 2005 [9]).

CHAPTER II NANOPHOTONIC SEMICONDUCTOR DEVICES

In this chapter, we will discuss the main advantages of nanophotonic devices compared to conventional structures. We will also summarize some main fabrication technique for realization of nanophotonic devices used throughout this dissertation.

2.1 Tall Structure and Thin Film Structures

In the case of semiconductor based nanophotonic devices, we define nanophotonic devices as those that has sub-micron feature in the plane perpendicular to the wafer growth direction. Based on the definition, we can then further group the nanophotonic devices into two categories based on their vertical optical confinement: namely the thin-film structure and tall structure.

2.1.1 The Tall structures

Before discussing at the difference between the tall structure and the thin-film structure, let us first look at the conventional semiconductor waveguide structure. Taking the commonly seen $Ga_xIn_{1-x}As_yP_{1-y}$ material system for example, which is widely used in devices operating around the wavelength of 1550nm, the refractive index can vary from 3.17 to around 3.57

depending on the choice of x and y. Vertical optical confinement can then be provided from the refractive index difference between different material compositions, forming weakly guided waveguide with optical mode size of several microns. In conventional structures, the horizontal optical confinement is typically provided by shallow etched ridge structure, which also can be viewed as waveguides with small refractive index difference between core and cladding. For the case of nanophotonic devices, the horizontal optical mode size is much smaller because of the strong refractive index difference between the core (semiconductor, n~3.2) and cladding material (air, SiO_2, BCB, etc., n<2).

The tall structures have strong confinement only in the horizontal direction. In the vertical direction, the structure is the same as the weakly guiding conventional devices, which is typically about 3 μm in height, leading to optical mode size of around 1 μm in the vertical direction. As the vertical structure size is much larger than the horizontal structure size, the resulting optical devices are referred to as "tall structure" as shown in Fig. 2.1. Because of the high refractive index contrast in the horizontal direction, the tall structures can make sharp horizontal bends and can be use to make various microcavity and photonic bandgap nanophotonic devices. For λ=1.55μm, the mode size (FWHM) in a photonic-well waveguide can be as small as 0.5μm (vertical) by 0.3μm (horizontal) for a physical structure of 0.4μm in thickness and 0.5μm in width. This gives a mode area of $0.15\mu m^2$

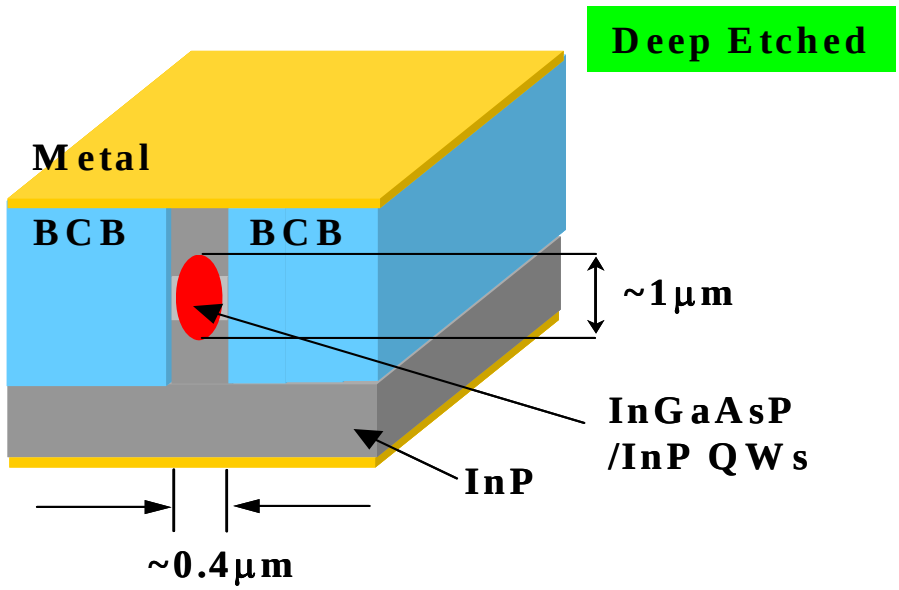

Fig. 2.1 Typical tall structure

2.1.2 The Thin Film Structures

The thin-film type structures refer to devices in which the thin high refractive index semiconductor core, typically with thickness ~ 0.2 micron, is sandwiched between low refractive index materials (Fig. 2.2). For example, the low refractive index material could be air (n=1) in micro disk and photonic bandgap lasers, or the low refractive index material could be polymer materials or silicon dioxides (n~1.4-1.5) such as photonic wire lasers and micro-ring resonators. The thin-film structures provide strong mode confinement in both the horizontal direction and the vertical direction. For 1.55μm wavelength, the mode size (FWHM) in a photonic-wire waveguide can be as small as 0.2μm (vertical) X 0.3μm (horizontal) for a physical structure of 0.2μm thick and 0.5μm wide. This gives a mode area of 0.06μm^2.

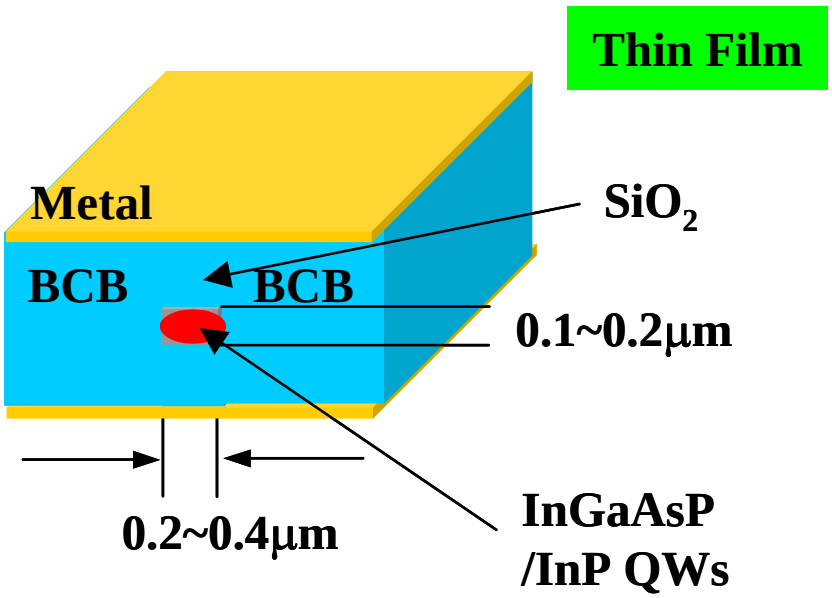

Fig. 2.2 Typical thin-film structure

2.1.3 Pro and Cons of Tall Structure and Thin-Film Structure

The pro and cons of tall structure and tin film structure can be analyzed from various aspects as follows. :

(1) The optical mode size

As discussed earlier, one main advantage of nanophotonic devices is the lower optical power requirement resulting from smaller optical mode size. In the case of the thin film structure, because of the strong optical confinement in the vertical direction, the mode size can be further reduced in the vertical direction, achieving the smallest possible optical mode, thus lower the optical power consumption even further.

(2) The etching quality consideration

In terms of fabrication, thin film structure gives us a lot of advantages in InP/InGaAsP etching. The InP/InGaAsP layer of thin film structure is only 0.2μm compared with 3-4μm thick of tall structure. When the etching depth reduces, the sidewall will expose to less lateral attack from etching gas, which is one of the major reason for sidewall roughness and bad verticality. Meanwhile, for the same thickness of the etching mask, mask erosion will be much less because of the shorter etching time. As a result, thin film etching is expected to yield smoother sidewall and better verticality, thus much less optical loss will present in the final devices.

(3) The fabrication complexity consideration

Thin-film nanophotonic structures have various advantages. First is the small mode size. The mode size of the conventional semiconductor device waveguide is about 0.5μm (vertical) X 3μm (horizontal) for a physical structure of 0.4μm thick and 3μm wide rib waveguide. This gives a mode area of $1.5\mu m^2$. We can see that the mode size of thin film nanophotonic devices is 30x smaller than that of conventional device. As will be discussed below, the small mode size translates to high beam intensity, which helps in increasing the device performances.

(4) Impact on nanofabrication resolution

Another critical step in the fabrication of the photonic transistors is defining the critical device dimensions, especially the width of the two waveguide, and the gap of the coupler. As those dimensions are defined by dry etching, the larger the etching depth, the more difficult it is to accurately control the size of the structure. The minimal etching depth possible will be the thickness of the quantum wells, which in our case will be ~400nm. If thin film wafer bonding is used, that will be all the thickness we will need to etch.

(5) Impact on electrically pumped nanophotonic devices

If we take laser as example, the tall structure and thin film structure has some additional pros and cons. The vertical mode size has significant effect on modulation speed. For the same current density, the reduction in the vertical mode size leads to higher photon intensity, which in turns gives higher stimulated decay rates. The higher simulated decay rates will lead to higher direct modulation rates. If we reduce the vertical mode size, the total output power per unit waveguide width will remain the same. This is because the same current per unit area supplied will be converted to a particular optical power per unit waveguide width (assuming the cavity structures such as mirror reflectivity is unchanged).

2.2 Quantum Well Intermixing

2.2.1 Quantum well intermixing background

The realization of integrated all-optical or optoelectronic nanophotonic devices often requires methods to allocate different area of the wafer with different bandgaps. By doing so, it is possible to integrate passive and active devices, active devices with different bandgap energies, or single devices with both active and passive parts. Fig. 2.3 illustrates two examples. In an absorption based micro-ring filter, it is desirable to make the ring part absorptive, while keep the input and output waveguide transparent at the operating wavelength. In a photonic band gap laser, in order to minimize the injection current, we should allocate active area only in the center of the optical mode, while keep the rest of the structure transparent.

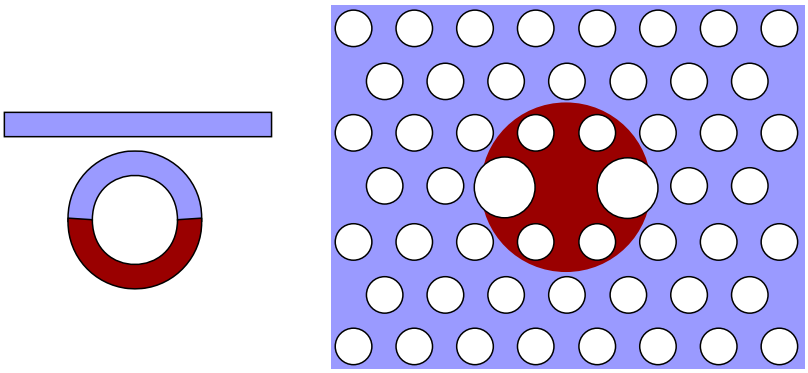

Fig. 2.3 Device examples need passive and active integration

Over the years many approaches has been investigated to realize different bandgap structure on the same wafer. Those approaches can be divided into two main categories: those involving more than one epitaxy growth and those with only one epitaxy growth.

The representative examples of the first category include selective area epitaxy [10] as well as etching and regrowth [11]. In selective area epitaxy, crystal growth is restricted to the dielectric windows formed on the substrate, which is defined by lithography. Similar effect can be achieved by etching away the epitaxy layer in selective area after whole wafer growth. Regrowth is then used to grow the rest of the areas with different quantum structures. Those approaches have the advantage of flexibility in choosing structures for different area, leading to higher material quality. However, multiple epitaxy growth also leads to high cost. In addition, the joints between adjacent areas are typically discontinues, leading to additional optical insertion and reflection loss.

In the second category, different bandgaps in selective areas are obtained by post-growth modification on the quantum wells. For example, quantum well intermixing (QWI) techniques utilizes the inter-diffusion effect between the quantum well and the barriers to alter the quantum

well bandgap energy. It offers the possibility to control heterostructure bandgap profiles at the post-growth level, and has the advantages of being low cost, since there will not be repeated use of epitaxial growth system. The joints between different areas will be smoother, and the areas involved can be very small, on the micron range.

Over the year, several approaches have been used to realize QWI. Among which the most important methods include the following. (1) Impurity induced disordering (IID), in which impurities such as dopants are used to enhance the III-V material self-diffusion in the crystal and promote intermixing. However, the dopants will also change the electrical characteristic of the structure dramatically, thus limits the application of this method. (2) Impurity free vacancy diffusion (IFVD), which commonly use a SiO2 layer to promote the outer diffusion of Ga. This method requires quite high annealing temperature compared to other approaches. (3) Photoabsorption induced disordering (PAID), in which high power laser pulses is used to produce transient heating in the crystal. The resulting thermal expansion will then cause bond breaking and lattice disruption that lead to a localized increase in the density of point defects. This method has been shown to give good spatial resolution and high material quality. The drawback lays in the fact that in complex device geometry, it will be time consuming to scan the laser beam through the wafer. (4) Ion implantation assisted QWI, which relies on the diffusion of point defects created during ion implantation. In this dissertation study, we will focus on the use of low energy ion implantation induced quantum well intermixing technique in the fabrication of nanophotonic devices.

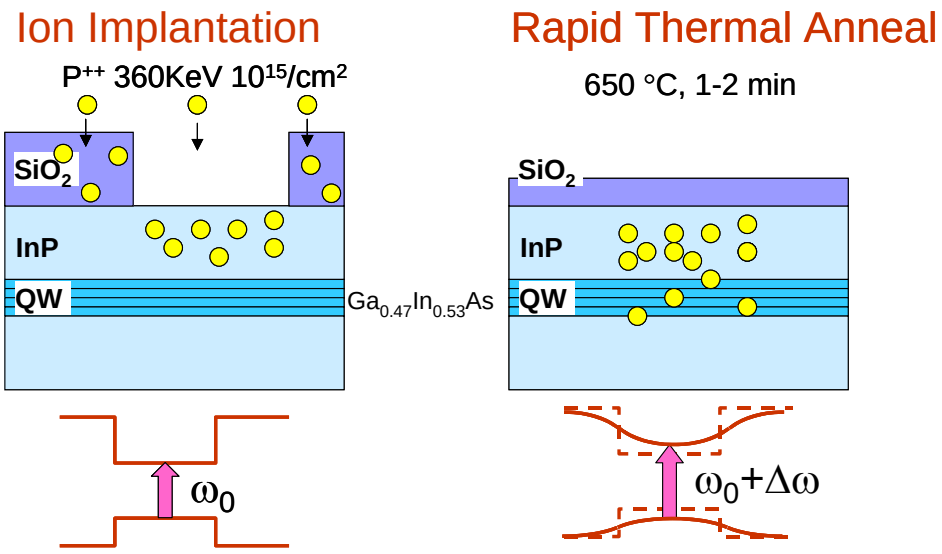

Fig. 2.4 Quantum well intermixing process

The low-energy ion-implantation induced quantum-well intermixing process used in this work was discussed in details in [12]. An exemplary process is shown in Fig. 2.4, which involves two steps. We start with a sample with selective areas covered by implantation mask (SiO_2 in this case). In the first step, the samples are implanted with phosphorus ions with ion energy of 360KeV. The energy of the ions is chosen so that in areas exposed to the implantation, the penetration depth of the ion will be much less than the cladding InP layer thickness, hence very little implantation damage is introduced in the active quantum well region. Meanwhile, in areas covered by SiO_2 mask, almost all ions will stopped within the SiO_2 mask layer. In the second step, the SiO_2 mask is removed and vacancies are then diffused through the structure during a rapid thermal anneal. The annealing time is about 2min at temperature of 650 degree C. During the anneal, the vacancies diffuse through the quantum-well region, the quantum-well and barrier interfaces are smeared, leading to an increase in quantized energy level in the well. As a result, the bandgap energy of the implanted region will undergo a blue-shift (>120nm) by inducing

inter-diffusion of atoms between the quantum wells and their barrier materials. Specifically, the well is InGaAs and phosphorus ions are diffused from the InGaAsP barrier into the well, causing the well to be effectively narrower, resulting in a blue shift of the bandgap energy. The large energy shift results in very good passive section with measured loss <1/cm (4dB/cm) including the free-carrier absorption of the p-side dopants.

One main question in design the QWI process is to decide the energy to use for the implantation ions, and the required thickness for the mask in order to block nearly all of the ions in regions where the original bandgap will remain. Fig. 2.5 shows a TRIM simulation of the P++ ion penetration depth in both InP and SiO_2 at different energy. Where the dot shows the mean vertical traveling distance D of the ion from surface and the error bar shows the average deviation from the mean value ΔD. In the case of N total ions with penetration depth of x_i (i=1..N), we have:

$$D = \sum_{i=1}^{N} x_i / N \; ; \; \Delta D = (\sum_{i=1}^{N} (x_i - D)^2 / N)^{1/2} .$$

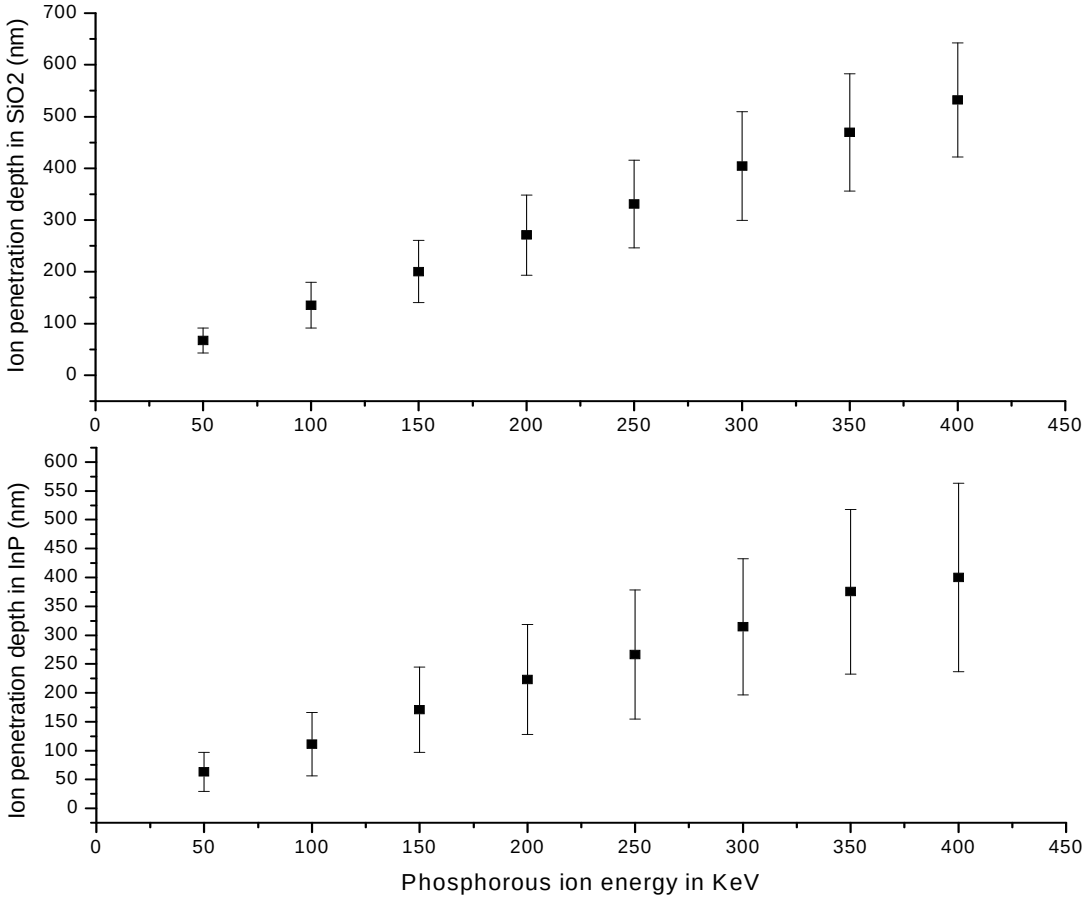

Fig. 2.5 Ion implantation depth at different implanting energy

2.2.2 Discussion on QWI Resolution

The lateral resolution of the quantum well intermixing is critical to the realization of the nanophotonic devices with different bandgap region in close proximity to each other. One such example is the case of the all-optical photonic transistor device to be discussed in Chapter IV, in which two arms of a nano waveguide coupler will need to have two different bandgap for the

photonic transistor to work properly. If quantum well intermixing technique is used to modify the bandgap in different regions after the epitaxy growth of the quantum well. The question brings down to the lateral resolution achievable by the quantum well intermixing.

There are two factors in determining the final resolution of the quantum well intermixing. The first factor in the resolution limit comes from the ion implantation process. The high-energy ions entering the wafer structure will collide with the atoms in the wafer and undergoes a Monte Carlo process. The final distribution of the ion is influenced by many factors. Among which the most important factors include: the type of the implanted ion, the energy of the implanted ion, the wafer structure (materials, thickness, etc.), and the implantation condition such as temperature and tilting. As the wafer structure for certain photonic device is mostly fixed, the type of implantation ion, which is typically chosen among the neutral species in the wafer system to eliminate free carrier absorption, will be fixed too. The next main parameter that can be adjusted is the implantation ion energy. TRIM simulation is used to estimate the mean vertical depth and mean lateral range of implanted ion, and the result is plotted out in Fig. 2.6. In this case, we choose the typical example of P++ ion implanted into InP based wafer structure with a tilt angle of 7 degree to reduce channeling effect.

From the simulation, we can see that both the depth of the ion and the lateral range increase with higher implantation energy. In order to minimize the lateral range of the implanted ion, it is necessary to minimize the implantation energy. However, reduced implantation energy leads to small vertical depth. If the wafer structure is fixed so the distance from the top of the wafer to the quantum well region is fixed, when the implantation depth is reduced, the traveling distance of the vacancies will need to be increased in order to reach the quantum wells. And this

can be achieved via either increasing the annealing temperature or lengthen annealing time. Unfortunately, both increased annealing temperature and longer annealing time will have an adverse effect on the resolution of the QWI, as the vacancies will smear out more both vertically and laterally at the same time.

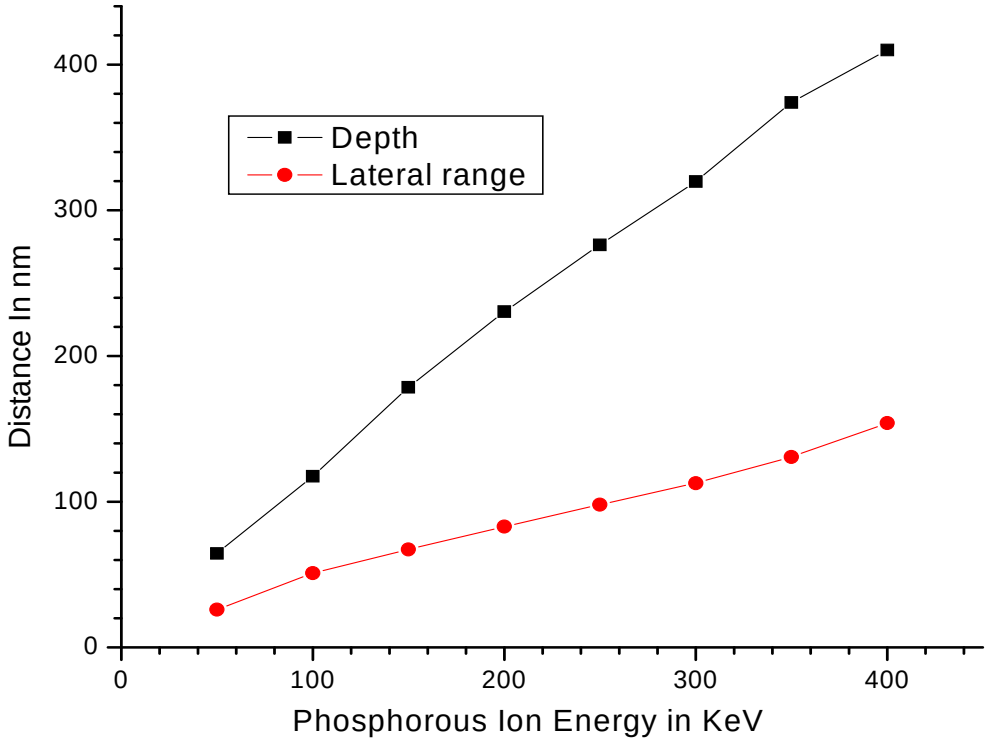

Fig. 2.6 TRIM simulation of the mean ion lateral range and depth at different ion energy (phosphorous ion implanted 7 degree into InP substrate)

As discussed above, the second part of the resolution limit comes from the annealing process. During the annealing, the elevated temperature causes the point defects to move around.

The defects type, the wafer structure involved, and the annealing condition, including temperature and time will all affect the traveling distance of the defects. The influence on the resolution of the QWI process is more difficult to analyze. However, intuitively, we can see that higher temperature and longer annealing time will compromise the resolution more as the traveling distance of the defects will be increased.

From the analysis above, we can see that in order to increase the QWI resolution, one key factor is to minimize the horizontal spreading of the implanted ions, as well as minimizing the necessary traveling distance of the point defects. There are several ways to achieve those. One possible approach is to increase the implanted ion energy so the ions will be directly implanted to the quantum well region. In this case, only minimum or no annealing at all in needed after the implantation. However, by implant directly to the quantum well region, direct material damage in introduced to the quantum wells and the optical loss of the structure will be very high.

While keeping this option open, in the initial fabrication, we choose to implant to the cladding layer instead of the quantum well region to avoid excessive optical loss from the ion bombardment. To minimize the traveling distance of the point defects, it is then necessary to make the ion implantation depth as close as possible to the quantum well region. Since the free carrier absorption loss increase as the ions gets closer the center of the optical mode, it will be highly desirable if after the quantum well intermixing, the top cladding layer can be removed, further eliminates the loss from the ion-induced damages, which lead to our interest in thin film wafer bonding process.

2.3 Fabrication Procedure for the Tall Structure with QWI

The devices been fabricated in this dissertation can be divided to two groups: the tall structure and the thin-film structure. Here we would like to summarized the basic fabrication procedures for both cases when quantum well intermixing is needed. In the case of the tall structure, the fabrication procedure is illustrated in Fig. 2.7. We start with an epitaxial grown quantum well wafer. Then SiO_2 implantation mask is deposited by PECVD. The SiO_2 mask will be patterned by either photolithography or ebeam lithography, depending on the accuracy of the QWI we are targeting. The SiO_2 layer is then etched to open window in selective areas where the bandgap will be shifted. After the ion implantation, the SiO_2 layer is removed and another layer of SiO_2 is deposited to protect the wafer surface during rapid thermal annealing. After the annealing and targeted bandgap shift is achieved, the wafer will be patterned according to the device requirement and by the device and optical structure will be formed by deep ICP etching.

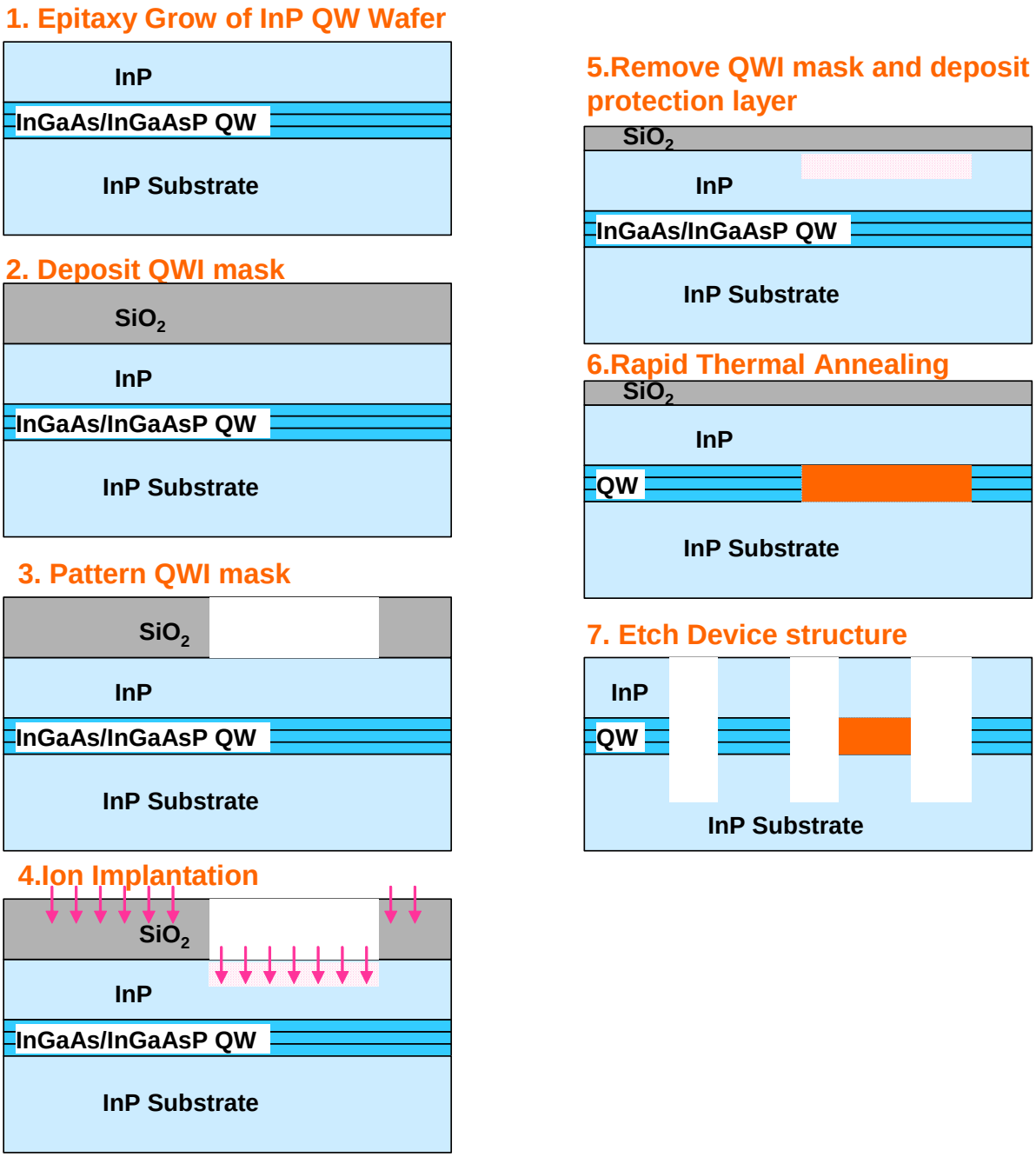

Fig. 2.7 Fabrication procedure of tall structure with QWI

2.4 BCB Based Thin Film Wafer Bonding Process

Above we have discussed some of the main advantages of having large vertical index contrast in photonic structures, such as reduced operation power and ease to achieve high quality etching. On way to achieve high refractive index contrast is to have the structure suspended in air, such as in the case of micro disk [13, 14] or photonic band-gap structure [15]. Another way to achieve high refractive index contrast is to utilize the low refractive index of certain polymer (BCB, n~1.56) [16] or dielectric material (SiO_2, n~1.45) compared to the high refractive index of III-V semiconductor material (n~3.2). In this section we will review the main processing steps of BCB assisted thin film wafer bonding process.

The typical process steps of thin film wafer bonding process for InGaAs/InGaAsP quantum well wafer is shown in Fig. 2.8. The first step is the epitaxy growth of the InGaAs/InGaAsP quantum well wafer on InP substrate. The wafer is then patterned with the device pattern and etched through the quantum well. BCB 3022-35 is spin onto the patterned wafer, as well as a GaAs carrier wafer. The quantum well wafer is then carefully flipped onto the GaAs wafer. The whole assembly is placed onto a hotplate (~120 degree C) and force is used to introduce pressure onto the top wafer and meanwhile one need to align the cleaved facet of the GaAs wafer and the InP wafer so the final device can be easily cleaved later on. After that, the whole assembly will be put into a nitrogen oven to cure the BCB. The temperature cycle should follow the recommendation of the BCB manufacturer. After curing, the top InP substrate is manually polished down to <50 micron (usually start with ~350 micron). Then the assembly is put into hydrochloric acid solution (2:1) to remove the remaining InP. Because of the high

etching selectivity of InGaAs/InGaAsP/GaAs versus InP in HCl, the InP top layer will be removed without affecting the quantum well and the GaAs carrier wafer.

In this dissertation, we are mainly interested in the InGaAs/InGaAsP material system that emits at wavelength around 1550nm. However, the BCB assisted thin-film wafer bonding process has no intrinsic constrain on the material system that can be used. The only requirement is that the substrate of the original wafer (InP in the example) can be removed selectively without affecting the carrier wafer (GaAs in the example) and the thin-film (InGaAs/InGaAsP).

In devices require quantum well intermixing, thin film wafer bonded structures have an addition advantage in that the ions can be implanted to locations very close to quantum well, thus improving the quantum well intermixing resolution. Implantation to very close proximity of the quantum well is usually avoided in more conventional structure because the ions will induce excessive free carrier absorption loss. However, for the thin-film structure, the top cladding containing the implanted ions will be removed after annealing, eliminating the absorption loss from the ion. It is not entirely impossible to implant close to quantum well and still have minimal loss in conventional structure. One proposed approach is to remove the top cladding after anneal and regrow the top cladding. Though theoretically possible, the involving of regrow in the process eliminates one of the main QWI advantage – the much lower cost.

Fig. 2.8 illustrates the typical fabrication procedure for a thin film structure when QWI is needed. The main difference as compared to the tall structure is that the ions can be implanted to location very lose to the quantum well. So the top cladding InP can be thin. And the annealing time will be shorter, or annealing temperature will be relatively lower. After QWI, the Top InP

cladding is removed, the device structure will be etched into the quantum well, and BCB wafer bonding will be carried out.

Compared to the typical BCB wafer bonding process discussed before, here the semiconductor thin film is sandwiched between SiO_2 films. This is done by depositing SiO_2 film after the III-V etch in step 8, and deposit another layer of SiO_2 after wafer bonding in step 13. Although the processes involved will be more complex, the addition of the SiO_2 layer offers stronger mechanic support to the nanoscale structures inside.

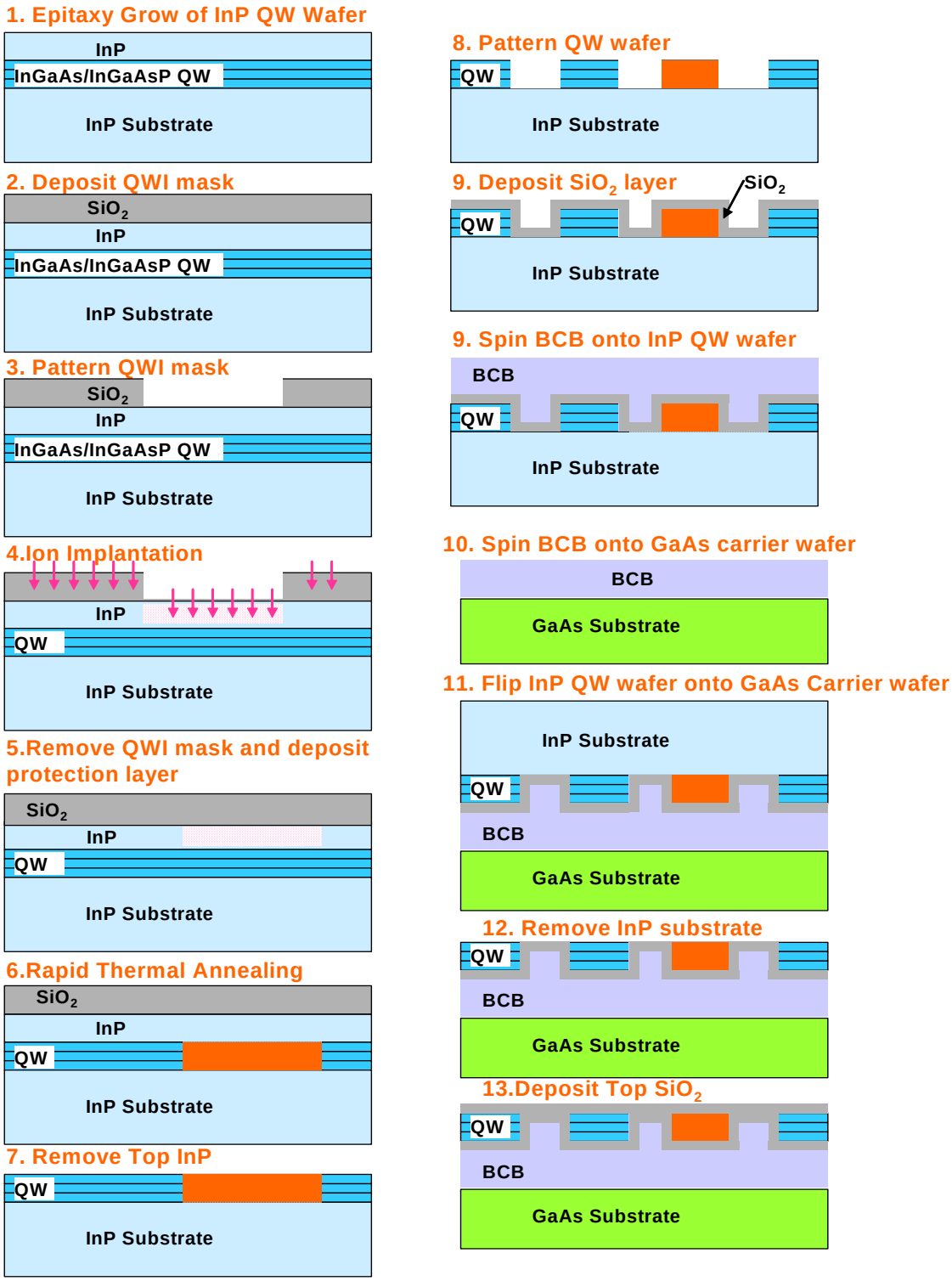

Fig. 2.8 General procedure for thin film device fabrication with QWI

CHAPTER III A FDTD MODEL BASED ON MULTI-LEVEL MULTI-ELECTRON SYSTEM

In chapter II we discussed some of the main advantages of nanophotonic devices, as well as typical fabrication techniques. In this chapter we will deal with the simulation method of nanophotonic devices. Numerical computation for electrodynamics capable of providing full spatial-temporal solution for the electromagnetic field interacting with material media using Finite Difference Time Domain (FDTD) [17,18] method has attracted much interest in photonic and optoelectronic device simulation, especially in situations where conventional device simulation methods are inadequate or cannot cope with the complex device geometry. An example is the case of photonic bandgap or microcavity structures with active semiconductor medium as part of the structure to provide gain or ultrafast optical nonlinearities. In this case, the spatial variations of the medium's refractive index, gain, or absorption could be dependent transiently on the varying lightwave intensity while the mode profile that determines the intensity could in turn be affected by the medium's refractive index, gain, absorption, and the optical nano-structure. Another example is the case of a laser cavity with multiple longitudinal or transverse modes in which multi-frequency lasing, instability, or laser pulsing behaviors could develop. These behaviors could be dependent on the carrier band-filling effect and the spatial or

spectral hole burning of the carrier distribution, which in turn could be affected by the transient and local interaction of the electromagnetic field mode with the gain medium.

In actual implementation, the dynamics of the active media in the devices must be modeled with reasonable physical realism in order for the potentials of the FDTD method to be fully realized. The medium involved typically has complicated internal electron dynamics. For example, the dynamics of multiple electrons could be involved and the quantum energy level structure for the electrons in the medium must be accounted for. Furthermore, these devices often operate at room temperature, and the thermal process of the electrons must be considered. It would be of substantial interest to develop a FDTD computational model for complex dynamical media that is sophisticated enough to encompass the essential physics of such media and yet computationally efficient. We will show that with use of a multi-level multi-electron quantum system having the electron dynamics governed by Pauli Exclusion Principle, state filling, and dynamical Fermi-Dirac Thermalization, the essential physics of many complex media, including semiconductor, can be encompassed in FDTD simulation. We will refer to this FDTD computational model as dynamical-thermal-electron quantum-medium FDTD (DTEQM-FDTD). The dynamical-thermal-electron nature of the model refers to the explicit inclusion of thermal processes dynamically for the electrons. The quantum nature of the model refers to the explicit inclusion of energy level structure and the Pauli Exclusion Principle. We will show how a simple thermal hopping model dictated by the Pauli Exclusion Principle automatically resulted in Fermi Dirac Statistics for the electron state filling in the steady state. The broad applicability of the model methodology relies on the fact that the interaction of electromagnetic field with material media is via a collection of oscillating electric dipoles governed by the electron dynamics and the

DTEQM-FDTD model shows how the complex electron dynamics in multiple energy levels can be efficiently treated.

The model methodology shall be generally applicable to a wide range of solid-state, molecular, or atomic media, by employing the treatment of electron dynamics described here with the appropriate medium-specific effective carrier rate equations and effective multi-energy-level structure needed for obtaining the medium polarization density. One of the most complex material media for photonic devices is direct bandgap semiconductor. We will illustrate the powerful capability of the model methodology by specifically developing it for modeling semiconductor medium as an example to show how the effective carrier rate equations and multi-energy-level structures are formulated, making them computationally efficient. Its applications to other solid-state, molecular, or atomic media will involve similar approaches and in many cases will be simpler than the semiconductor example.

In applying to semiconductor, we show that this model could take into account the transient intraband and interband electron dynamics, the semiconductor band structure, and the carrier thermal equilibrium process. The model automatically incorporates the required band filling effect. It also incorporates the typical nonlinear optical effects associated with carrier dynamics. Our approach enables the model to treat thermally activated carrier scattering process under transient excitation spatial-temporally. These capabilities enable the model to treat sophisticated semiconductor optoelectronic and nanophotonic devices having complex device geometries and medium dynamics with full spatial-temporal solutions at the microscopic level. We will show that although the model is complex enough to include all the essential physical effects, it is simple enough to achieve fast computational time.

In this chapter, we present the basic formulation of this powerful general model with applications to direct bandgap semiconductor, ultrafast optical phenomena, and multimode microdisk semiconductor laser as illustrations, which also validate the computational stability and efficiency of the model.

3.1 General Approach

In the past, various methods have been proposed to model active medium in FDTD simulation. They can be grouped into two main categories: the macroscopic approach [19] and the microscopic approach [20]. The macroscopic approach models the medium gain by introducing a negative frequency-dependent conductivity term into Maxwell equations and solve for the imaginary part of the polarization, while the microscopic approach explores rate equations. The rate equation approach in [20] employed a modified classical electron model to describe the gain and absorption dynamics of an atomic system with a single electron. Recently, we have introduced a quantum mechanical model of a 4-level 2-electron atomic system with the incorporation of the Pauli Exclusion Principle for FDTD simulation [21-24]. The employment of two electrons enabled us to provide a simplified model for semiconductor, which took into account a simple picture of electron-hole pumping dynamics from the lower valence band to the upper conduction band. Our quantum-medium model [21-24] with four energy levels and two electrons governed by the Pauli Exclusion Principle is an advancement over the previous models. However, the model is still too simple to properly encompass the complex physical effects in the medium such as the semiconductor energy band structure, band filling effect with Fermi Dirac

statistics, carrier induced gain and refractive index change, and carrier relaxation to thermal equilibrium after excitation. As a result, much of the transient and nonlinear behaviors in the medium were not included.

The typical approach to modeling carriers in semiconductor band structure involves solving Bloch equations at many energy states in the momentum space (k-states) [25, 26]. In FDTD simulation, the structure to be simulated is first discretized spatially, then the electromagnetic field at each spatial point is updated at each time step, making FDTD an intrinsically numerically intensive method. Now in addition to all that, if we use the typical approach of semiconductor modeling, then for each grid, we will have to update the carrier distribution function in many k-states at each time step [27], making the computational time forbiddingly long. The original k-states are quantized states given by $k_x=2\pi n_x/L_x$, which is dependent on the size of the medium L_x. As these k-states are energy broadened by the spontaneous decay time, we may combine the original k-states into energy-broadened k-states that are interspaced by the spontaneous decay width. With a typical spontaneous decay time of ~ 3ns for direct bandgap III-V semiconductors, there will be $\sim 10^5$ energy broadened k-states within a typical 50nm wavelength spectral width of interest at the optical communication wavelength of λ=1550nm. This is still a large number for FDTD simulation.

In our 4-level 2-electron FDTD model treatment [21-24], it is pointed out that due to the short dipole de-phasing time of excited dipoles in semiconductor (~100fsec), comparing to the spontaneous decay lifetime of 3nsec, one can further represent many energy-broadened k states by one effective k state, provided the electron-scattering process that affect the dipole phase is

lumped into an effective dipole dephasing time. For, example, a dipole dephasing time (T_2) of ~50fsec will result in a spectral broadening of $\Delta\lambda$~50nm (FWHM) at λ=1550nm. Thus, only a few such dipoles are needed to cover a wavelength range of 100-300nm, which is sufficient for various optoelectronic and photonic device applications.

It turns out that the dipole dephasing is due mainly to the thermally activated carrier scattering. At room temperature, the thermal energy of k_BT (k_B is the Boltzman constant and T is the Kelvin temperature) corresponds to a FWHM energy broadening of $\hbar\Delta\omega$ =18meV ($\Delta\lambda$=35nm at λ=1550nm). For a solid-state medium with strong electron interaction, the dipole dephasing may correspond to the thermal energy, giving a thermally-induced dipole dephasing time of $T_2=2/\Delta\omega$=75fsec at 300K. Thus, although the effective values for T_2 in different media may depend on the actual dephasing mechanisms (the T_2 value can be experimentally obtained from the homogeneously-broadened linewidth), they will be in the order of ~100fsec [25, 26]. Hence, the fast dipole dephasing is generally applicable to all solid-state media with strong electron interactions. This means that most solid-state media can also be modeled with only a few dipoles to cover a wide wavelength range. While illustrated for the case of semiconductor, the DTEQM-FDTD modeling approach developed here can be adapted for modeling a wide range of solid-state, molecular, and atomic media.

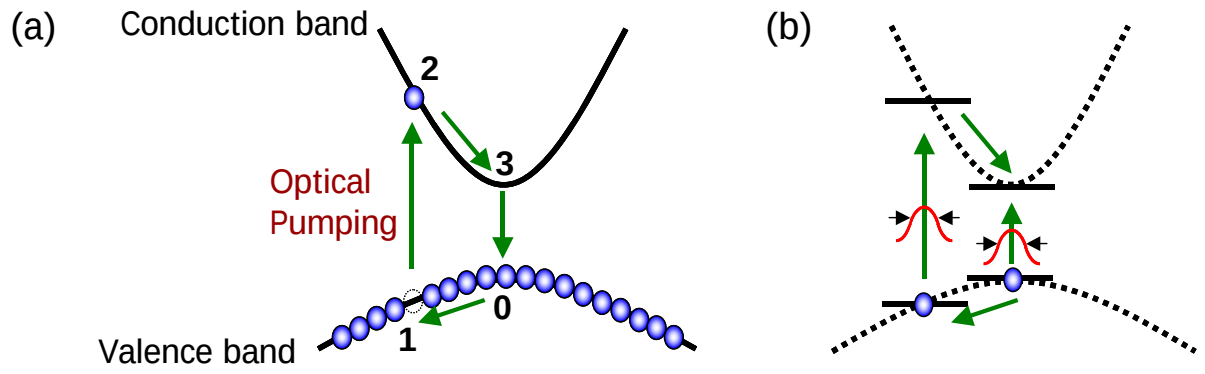

Fig. 3.1 electron dynamics in our 4-level 2-electron model: (a) electron interband and intraband dynamics in semiconductor medium under excitation of photon with above-bandgap energy; (b) representation by four energy levels and two electrons.

To set up the model, let us first consider a simple case for which a semiconductor medium is under optical excitation with above-bandgap energy, as shown in Fig. 3.1(a). The medium is at ground state initially. Under excitation of the photons, the electron at the corresponding energy (position 1) will undergo interband excitation to the conduction band (position 2), leaving a hole at the valence band. The electron at position 2 and the hole at position 1 in Fig. 3.1(a) will then undergo intraband decay to the band edge positions 3 and 0, respectively, through phonon-assisted processes. The hole position moving from 1 to 0 in the valence band is equivalent to electron moving from position 0 to 1. Subsequently, the electron and hole will recombine via radiative or nonradiative decay and the medium will return to its original ground state. Current injection via p-i-n junction can likewise be modeled by pumping electrons electrically from the lowest valence-band level to the topmost conduction-band level. In this example, we can see that the broad dynamics for the electron transition can be described

by having two electrons resting in four energy levels, as shown in Fig. 3.1(b). To ensure that the electron will not decay to the lower level unless there is an energy-state vacancy, Pauli Exclusion term was implemented. This forms the basis of our earlier 4-Level 2-Electron Model with Pauli Exclusion Principle [21-24].

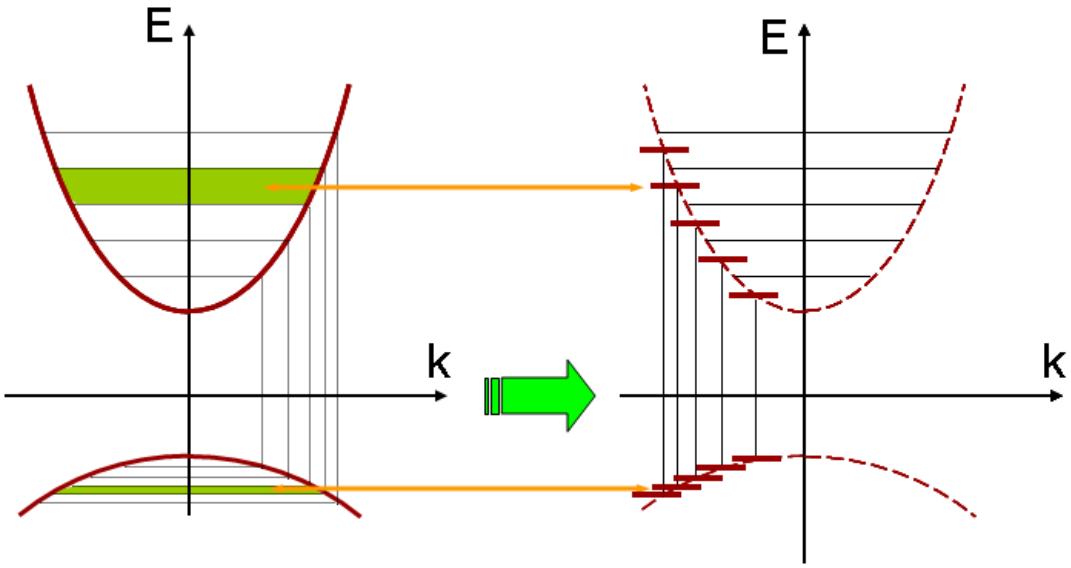

Fig. 3.2 the multi-level multi-electron model for FDTD simulation of semiconductor material.

To more accurately model semiconductor medium dynamics, additional energy levels and electron dynamics are needed. The main idea of our multi-level multi-electron model discussed recently [28] is to divide the conduction and valence band states to several groups, and then represent each group by a single dipole with broadened width, as shown in Fig. 3.2.

By doing so, the semiconductor medium dynamics included are: interband carrier radiative or nonradiative decays, intraband carrier relaxation, and interband transition (gain or

absorption). The semiconductor density of states is accounted for in the multiple energy level structure. Implementation of Pauli Exclusion Principle for the transitions between any two levels will result in carrier band-filling effect but would not account for finite temperature.

In our model, finite temperature is accounted for by a temperature-dependent intraband carrier-hopping dynamics that ensures Fermi-Dirac thermal distribution for the electron/hole occupation in the steady state, which we refer to as dynamical Fermi-Dirac thermalization. As will be seen below, this multi-level multi-electron model gives the expected band-filling behavior for a direct bandgap semiconductor. In a more sophisticated situation not shown here, by using temperature as a spatial-temporally varying parameter, this approach will enable the FDTD model to treat thermally activated carrier scattering process and carrier heating or cooling under transient excitation in both space and time, while solving for the interaction of the electromagnetic field modes with the medium. The spatial movement of carriers is also not shown here but can be built on top of the FDTD model [25-26].

Thus, the basic DTEQM-FDTD model developed here, when combined with a lattice temperature diffusion model and/or a spatial carrier diffusion model, will result in a powerful device model with sophisticated spatial-temporal solutions for both the medium and electromagnetic field. When applied to semiconductor, we will simply refer to the DTEQM-FDTD model as “dynamical-semiconductor-medium FDTD” (DSM-FDTD) model.

3.2 The Dynamical-Semiconductor-Medium (DSM) FDTD Model

The energy-level structure for the DSM-FDTD model considered below is shown in Fig. 3.3. The continuous semiconductor band structure is simplified to discrete levels. The conduction band levels are labeled as *i_c* and the valence band levels are labeled as *i_v*, where *i*=1,2,…,*M* and *M* is the total number of levels used in the model. E_i represents the transition energy between levels *i_c* and *i_v* and obeys $E_i = \hbar\omega_i = 2\pi\hbar c/\lambda_i$. Levels *i_c* and *i_v* are used to represent the conduction and valence band states, respectively, with optical transition energy between $E_{i-}^B = E_i - (E_i - E_{i-1})/2$ and $E_{i+}^B = E_i + (E_{i+1} - E_i)/2$, so the densities of states per unit volume (volume densities of states) N_{Ci}^0 and N_{Vi}^0 in *i_c* and *i_v*, respectively, will be the sum of all the volume densities of states with energy in the bracketed interval [E_{i-}^B , E_{i+}^B] as $N_{(C,V)i}^0 = \int_{E_{i-}^B}^{E_{i+}^B} \rho_{c,v}(E)dE$, where $\rho_{c,v}(E)$ is the number of states per unit volume per unit energy at the optical transition energy *E* for conduction band (C) and valance band (V).

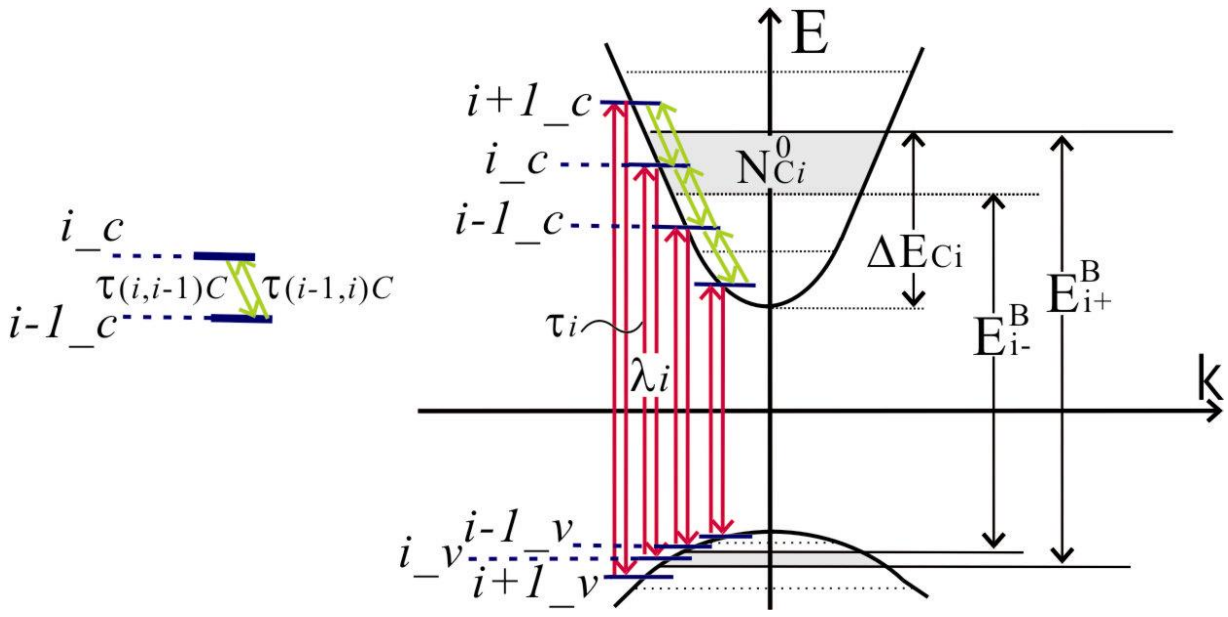

Fig. 3.3 The multi-energy-level model for the FDTD simulation of semiconductor material

If we take level *i_c* as example, the semiconductor carrier dynamics we considered in the model include: (1) interband radiative and nonradiative decays between conduction band levels *i_c* and *i_v* with decay time τ_i; (2) interband transition (stimulated decay or absorption) governed by dipole matrix element; (3) intraband down-transition (phonon-assisted decay) from *i_c* to *i*-1_*c* with transition time $\tau_{(i,i\text{-}1)C}$; (4) intraband up-transition (thermally activated) from *i*-1_*c* to *i_c* with transition time $\tau_{(i\text{-}1,i)C}$; (5) Intraband down-transition from *i*+1_*c* to *i_c* with transition time $\tau_{(i+1,i)C}$; (6) intraband up-transition (thermally activated) from *i_c* to *i*+1_*c* with transition time $\tau_{(i,i+1)C}$. Note that intraband transitions are between adjacent levels with times labeled by $\tau_{(i,f)C,V}$, where indices *i* and *f* label the initial and final levels, respectively.

3.3 Quantum derivation of the basic set of equations with minimal approximation

To obtain the basic set of equations governing the multi-level system quantum mechanically, let us first consider the optical interaction that occurred between interband levels. All the carrier dynamics below are described by electrons, including the hole carrier dynamics in the valence band. However, the electrons in the conduction and valence bands are characterized by different effective masses and intraband transition rates. The equations governing the transitions can be derived as follows.

We first start with the following exact minimal-coupling non-relativistic Hamiltonian describing atom-field interactions for a collection of N_0 single-electron atoms [29]:

$$\hat{H} = \frac{1}{2m_e}\sum_{j=1}^{N_0}[\hat{\mathbf{p}}_{ej}(t) - e\hat{\mathbf{A}}(\hat{\mathbf{r}}_{ej}(t),t)]^2 + \sum_{j=1}^{N_0}\hat{H}_{Cj}$$

$$+\frac{1}{2}\int_{V_Q} d^3\mathbf{r}\sum_{m\sigma}\frac{1}{2}[\frac{\mathrm{d}(\Omega_m\varepsilon_m)}{\mathrm{d}\Omega_m}\hat{\mathbf{E}}^2_{m\sigma}(\mathbf{r},t) + \mu_0\hat{\mathbf{H}}^2_{m\sigma}(\mathbf{r},t)] + \hat{H}_{\mathrm{ph}}, \tag{3.1}$$

where $\hat{\mathbf{r}}_{ej}$ is the position operator of the electron in the j^{th} atom, $\hat{\mathbf{p}}_{ej}$ is the canonical momentum operator of the electron in the j^{th} atom, m_e is the electron mass, $e = -|e|$ is the electron charge. The second term $\sum_{j=1}^{N_0}\hat{H}_{Cj}$ is the Coulomb interaction energy. The last term $\hat{H}_{\mathrm{ph}}$ is a dipole dephasing reservoir Hamiltonian similar to that given in [29]. The dynamics of the heavy nucleus has been neglected. $\hat{\mathbf{E}}_{m\sigma}$ and $\hat{\mathbf{H}}_{m\sigma}$ are the mode amplitudes of the electric and magnetic field operators and the field operators are given by:

$$\hat{\mathbf{A}}(\hat{\mathbf{r}}_{ej}(t),t)=\sum_{m\sigma} g_m \mathbf{e}_{m\sigma}[\hat{a}_{m\sigma}(t)e^{i\mathbf{k}_m\cdot\hat{\mathbf{r}}_{ej}(t)}+\hat{a}^{\dagger}_{m\sigma}(t)e^{-i\mathbf{k}_m\cdot\hat{\mathbf{r}}_{ej}(t)}],$$

$$\hat{\mathbf{E}}(\hat{\mathbf{r}}_{ej}(t),t)=\sum_{m\sigma} i\Omega_m g_m \mathbf{e}_{m\sigma}[\hat{a}_{m\sigma}(t)e^{i\mathbf{k}_m\cdot\hat{\mathbf{r}}_{ej}(t)}-\hat{a}^{\dagger}_{m\sigma}(t)e^{-i\mathbf{k}_m\cdot\hat{\mathbf{r}}_{ej}(t)}]=\sum_{m\sigma}\hat{\mathbf{E}}_{m\sigma}(\hat{\mathbf{r}}_{ej}(t),t),$$

$$\mu_0\hat{\mathbf{H}}(\hat{\mathbf{r}}_{ej}(t),t)=\sum_{m\sigma} ig_m(\mathbf{k}_{m\sigma}\times\mathbf{e}_{m\sigma})[\hat{a}_{m\sigma}(t)e^{i\mathbf{k}_m\cdot\hat{\mathbf{r}}_{ej}(t)}+\hat{a}^{\dagger}_{m\sigma}(t)e^{-i\mathbf{k}_m\cdot\hat{\mathbf{r}}_{ej}(t)}]=\sum_{m\sigma}\hat{\mathbf{H}}_{m\sigma}(\hat{\mathbf{r}}_{ej}(t),t),$$

(3.2)

where $g_m \equiv [\hbar v_m/(2\varepsilon_0 V_Q n_m \Omega_m c)]^{1/2}$ in which $n_m = \varepsilon_m^{1/2}$ is the refractive index of the embedded medium at frequency Ω_m, $\Omega_m = |k_{m\sigma}|c/n_m$ is the angular frequency of m^{th} field mode, and $v_m = \partial\Omega_m/\partial k_m$ is the group velocity. V_Q is the volume of quantization. The constant g_m given is valid for quantized field operators in a dispersive dielectric medium [30]. The operator $\hat{a}_{m\sigma}(t)$ and $\hat{a}^{\dagger}_{m\sigma}(t)$ are the annihilation and creation operators of the m^{th} field mode with polarization σ (σ=1, 2), and $\mathbf{e}_{m\sigma}$ is the unit vector representing the σ polarization of mode m. The mode number $m = \{m_x, m_y, m_z\}$ can be indexed by its m_x, m_y, m_z components with $\mathbf{k}_m = k_{mx}\mathbf{e}_x + k_{my}\mathbf{e}_y + k_{mz}\mathbf{e}_z$ and $|k_{mx}| = 2\pi m_x/L_x$, $|k_{my}| = 2\pi m_y/L_y$, $|k_{mz}| = 2\pi m_z/L_z$, so that L_x, L_y, L_z are the x, y, and z dimensions for an arbitrarily large volume of quantization V_Q ($V_Q = L_xL_yL_z$). The mode numbers take on positive and negative integer values as $m_{x,y,z} \in \{0, \pm1, \pm2, \pm3, \ldots\}$. Using Heisenberg equation of motion, we obtain:

$$\frac{d\hat{a}_{m\sigma}(t)}{dt}=\frac{i}{\hbar}[H(t),\,\hat{a}_{m\sigma}(t)]=-i\Omega_m\hat{a}_{m\sigma}(t)+ig_m\sum_j\frac{e}{m_e}[\hat{\mathbf{p}}_{ej}(t)-e\hat{\mathbf{A}}(\hat{\mathbf{r}}_{ej}(t),t)]\cdot\mathbf{e}_{m\sigma}e^{-i\mathbf{k}_m\cdot\hat{\mathbf{r}}_{ej}(t)},$$

$$\frac{\mathrm{d}e\hat{\mathbf{r}}_{ej}(t)}{\mathrm{d}t}=\frac{i}{\hbar}[H(t),e\hat{\mathbf{r}}_{ej}(t)]=\frac{e}{m_e}[\hat{\mathbf{p}}_{ej}(t)-e\hat{\mathbf{A}}(\hat{\mathbf{r}}_{ej}(t),t)]=\frac{\mathrm{d}\hat{\boldsymbol{\mu}}_j(t)}{\mathrm{d}t}\ , \tag{3.3}$$

where $\hat{\boldsymbol{\mu}}_j(t)\equiv e(\hat{\mathbf{r}}_{ej}(t)-\mathbf{r}_{nj})$ is the atomic dipole moment operator ($\mathbf{r}_{nj}$ is the nucleus position). This gives:

$$\frac{\partial\hat{a}_{m\sigma}(t)}{\partial t}=-i\Omega_m\hat{a}_{m\sigma}(t)+ig_m\sum_j\frac{\partial\hat{\boldsymbol{\mu}}_j(t)}{\partial t}\cdot\mathbf{e}_{m\sigma}e^{-i\mathbf{k}_m\cdot\hat{\mathbf{r}}_{ej}(t)}\ . \tag{3.4}$$

To show how to incorporate three-dimensional (3D) polarization vector, we consider a simple case where a two-level system has three upper levels $|E_{u_s}\rangle_j$ with $s\in\{x,y,z\}$ and one lower level $|E_g\rangle_j$. $\hat{n}_{gj}(t)$ and $\hat{n}_{u_sj}(t)$ are the atomic number operators in ground (g) level and upper (u_s) levels, respectively [31]. We have the atomic energy down transition operator $\hat{V}_{gu_sj}=|E_g\rangle_{jj}\langle E_{u_s}|$, the atomic energy up transition operator $\hat{V}^{\dagger}_{gu_sj}=|E_{u_s}\rangle_{jj}\langle E_g|$, and the dipole matrix element $\boldsymbol{\mu}_{gu_sj}\equiv{}_j\langle u_s|\hat{\boldsymbol{\mu}}_{ej}|g\rangle_j$. For simplicity, we will represent u_s by s and drop subscribes g in gu_s, so that $\hat{V}_{gu_sj}\equiv\hat{V}_{sj}$, $\hat{V}^{\dagger}_{gu_sj}\equiv\hat{V}^{\dagger}_{sj}$ and $\boldsymbol{\mu}_{gu_sj}\equiv\boldsymbol{\mu}_{sj}$. Under electric dipole approximation, $\hat{\mathbf{A}}(\hat{\mathbf{r}}_{ej}(t),t)$ is replaced by $\hat{\mathbf{A}}(\mathbf{r}_{nj},t)$, where $\mathbf{r}_{nj}$ is the classical position of the nucleus [32].

The Hamiltonian can then be expressed in terms of these atomic and field operators (referred to as second quantization), which becomes $\hat{H}=\hat{H}_{Atom}+\hat{H}_{Field}+\hat{H}_{AF}$ with

$$\hat{H}_{Atom}=\sum_{jg}\hbar\omega_g\hat{n}_{gj}(t)+\sum_{js}\hbar\omega_s\hat{n}_{sj}(t)\,, \tag{3.5}$$

$$\hat{H}_{AF}=-\sum_{js}i\omega_a[\boldsymbol{\mu}_{sj}\hat{V}^{\dagger}_{sj}(t)-\boldsymbol{\mu}^{*}_{sj}\hat{V}_{sj}(t)]\cdot\hat{\mathbf{A}}(\mathbf{r}_{nj},t)+\sum_j\frac{e^2}{2m_e}\hat{\mathbf{A}}^2(\mathbf{r}_{nj},t)\,, \tag{3.6}$$

$$\hat{H}_F = \sum_{m\sigma} \hbar\Omega_m [\hat{a}^{\dagger}_{m\sigma}(t)\hat{a}_{m\sigma}(t) + \frac{1}{2}], \tag{3.7}$$

where ω_a=ω_s-ω_g. The 3D atomic dipole moment operator vector $\hat{\boldsymbol{\mu}}_j(t)$ can be expressed in $\hat{V}_{sj}$ and $\hat{V}^{\dagger}_{sj}$ as $\hat{\boldsymbol{\mu}}_j(t) = \sum_s [\boldsymbol{\mu}_{sj}\hat{V}^{\dagger}_{sj}(t) + \boldsymbol{\mu}^{*}_{sj}\hat{V}_{sj}(t)] = \sum_s \hat{\boldsymbol{\mu}}_{sj}(t)$. From the second quantized Hamiltonian, we can derive the following equations for the atomic operators using the Heisenberg equation of motion:

$$\frac{\mathrm{d}\hat{V}_{sj}(t)}{\mathrm{d}t} = -i\omega_a \hat{V}_{sj}(t) + \frac{\omega_a \mu_{sj}}{\hbar}(\hat{n}_{sj}(t) - \hat{n}_{gj}(t))\hat{A}_s(\mathbf{r}_{nj}, t),$$

$$\frac{\mathrm{d}\hat{V}^{\dagger}_{sj}(t)}{\mathrm{d}t} = i\omega_a \hat{V}^{\dagger}_{sj}(t) + \frac{\omega_a \mu^{*}_{sj}}{\hbar}(\hat{n}_{sj}(t) - \hat{n}_{gj}(t))\hat{A}_s(\mathbf{r}_{nj}, t),$$

$$\frac{\mathrm{d}\hat{n}_{sj}(t)}{\mathrm{d}t} = -\frac{\omega_a}{\hbar}[\mu^{*}_{sj}\hat{V}_{sj}(t) + \mu_{sj}\hat{V}^{\dagger}_{sj}(t)]\hat{A}_s(\mathbf{r}_{nj}, t) = -\frac{\omega_a}{\hbar}\hat{\mu}_{sj}(t)\hat{A}_s(\mathbf{r}_{nj}, t),$$

$$\frac{\mathrm{d}\hat{n}_{gj}(t)}{\mathrm{d}t} = \sum_s \frac{\omega_a}{\hbar}[\mu^{*}_{sj}\hat{V}_{sj}(t) + \mu_{sj}\hat{V}^{\dagger}_{sj}(t)]\hat{A}_s(\mathbf{r}_{nj}, t) = \sum_s \frac{\omega_a}{\hbar}\hat{\mu}_{sj}(t)\hat{A}_s(\mathbf{r}_{nj}, t), \tag{3.8}$$

where $\hat{A}_s(\mathbf{r}_{nj}, t) = \sum_{s \in \{x,y,z\}} \hat{\mathbf{A}}(\mathbf{r}_{nj}, t)\cdot\mathbf{e}_s$. For a single electron system, we have the completeness relation $\hat{n}_{gj}(t) + \sum_s \hat{n}_{sj}(t) = 1$.

3.4 Multi-Electron Treatment

In the case of a system with multiple (2 or more) electrons, following the usual multi-electron treatment, the atomic number operators $\hat{n}_{gj}$ and $\hat{n}_{sj}$ shall be expressed in terms of the Fermionic electron creation operators ($\hat{c}_g^\dagger$, $\hat{c}_s^\dagger$) and annihilation operators ($\hat{c}_g$, $\hat{c}_s$) as $\hat{n}_{gj}(t) = \hat{c}_{gj}^\dagger(t)\hat{c}_{gj}(t)$ and $\hat{n}_{sj}(t) = \hat{c}_{sj}^\dagger(t)\hat{c}_{sj}(t)$ [25, 26], where these operators obey the equal-time Fermion anti-commutation relations:

$$\{\hat{c}_{k_1 j}^\dagger(t), \hat{c}_{k_2 j}(t)\} = \hat{c}_{k_1 j}^\dagger(t)\hat{c}_{k_2 j}(t) + \hat{c}_{k_2 j}(t)\hat{c}_{k_1 j}^\dagger(t) = \delta_{k_1,k_2} ,$$

$$\{\hat{c}_{k_1 j}^\dagger(t), \hat{c}_{k_2 j}^\dagger(t)\} = \{\hat{c}_{k_1 j}(t), \hat{c}_{k_2 j}(t)\} = 0 ,$$

where $k_1,\ k_2 \in \{g,\ s\}$. The atomic transition operators are then replaced by $\hat{V}_{sj}(t) = \hat{c}_{gj}^\dagger(t)\hat{c}_{sj}(t)$ and $\hat{V}_{sj}^\dagger(t) = \hat{c}_{sj}^\dagger(t)\hat{c}_{gj}(t)$ [33]. This procedure is valid in the free carrier limit in which the many-body Coulomb interaction effects associated with multiple electrons and other many-body effects are neglected [25]. The many-body effects often manifested themselves as effective shift in bandgap energy, dipole relaxation behavior (e. g. Markovian vs. non-Markovian) [27], density-dependent broadening and saturation, excitation-induced dephasing, or scattering of carrier and polarization [25]. These effects could be incorporated phenomenologically by effectively fitting the relevant parameters and in some cases by modifying the parameters in the DTEQM-FDTD model dynamically and using the time-dependent carrier density distributions as state parameters. The Hamiltonians in Eqs. (3.5) and (3.6) then become:

$$\hat{H}_{Atom} = \sum_{jg} \hbar\omega_g \hat{c}_{gj}^\dagger(t)\hat{c}_{gj}(t) + \sum_{js} \hbar\omega_s \hat{c}_{sj}^\dagger(t)\hat{c}_{sj}(t) , \tag{3.9}$$

$$\hat{H}_{AF} = -\sum_{js} i\omega_a[\boldsymbol{\mu}_{sj}\hat{c}^{\dagger}_{sj}(t)\hat{c}_{gj}(t) - \boldsymbol{\mu}^{*}_{sj}\hat{c}^{\dagger}_{gj}(t)\hat{c}_{sj}(t)]\cdot\hat{\mathbf{A}}(\mathbf{r}_{nj},t) + \sum_{j}\frac{e^2}{2m_e}\hat{\mathbf{A}}^2(\mathbf{r}_{nj},t)\,. \tag{3.10}$$

Using the usual derivation of quantum Langevin equations of motion from the Hamiltonian [34] by tracing over the thermal field reservoir states, which is equivalent to solving (using Eqs. (3.8)) for the atom-field operator evolutions to the first order under Markov's (memory-free) approximation, we will obtain the spontaneous decay terms. It turns out that with use of the Fermion anticommutation relations of the electron creation and annihilation operators, the decay terms for the electron upper-level population operator $\hat{n}_{sj}(t)$ will be in the form of $\hat{n}_{sj}(t)(1-\hat{n}_{gj}(t))$, which gives the Pauli Exclusion Principle [21-24]. This is because the electron transition rate term proportional to $\hat{n}_{sj}(t)(1-\hat{n}_{gj}(t))$ will reduce to zero when the lower level population $\hat{n}_{gj}(t)$ becomes 1 or fully occupied. The equations of motion for the atomic operators then become the followings:

$$\frac{\mathrm{d}\hat{V}_{sj}(t)}{\mathrm{d}t} = -i\omega_a\hat{V}_{sj}(t) - \gamma_{Vs}\hat{V}_{sj}(t) + \frac{\omega_a\mu_{sj}}{\hbar}(\hat{n}_{sj}(t)-\hat{n}_{gj}(t))\hat{A}_{\mathrm{s}}(\mathbf{r}_{nj},t) + \hat{\Gamma}_{V_{sj}}(t)\,,$$

$$\frac{\mathrm{d}\hat{V}^{\dagger}_{sj}(t)}{\mathrm{d}t} = i\omega_a\hat{V}^{\dagger}_{sj}(t) - \gamma_{Vs}\hat{V}^{\dagger}_{sj}(t) + \frac{\omega_a\mu^{*}_{sj}}{\hbar}(\hat{n}_{sj}(t)-\hat{n}_{gj}(t))\hat{A}_{\mathrm{s}}(\mathbf{r}_{nj},t) + \hat{\Gamma}^{\dagger}_{V_{sj}}(t)\,,$$

$$\frac{\mathrm{d}\hat{n}_{sj}(t)}{\mathrm{d}t} = -\gamma_{Ns}\hat{n}_{sj}(t)[1-\hat{n}_{gj}(t)] - \frac{\omega_a}{\hbar}\hat{\mu}_{sj}(t)\hat{A}_{\mathrm{s}}(\mathbf{r}_{nj},t) + \hat{\Gamma}_{n_{sj}}(t)\,,$$

$$\frac{\mathrm{d}\hat{n}_{gj}(t)}{\mathrm{d}t} = \sum_{s}\gamma_{Ns}\hat{n}_{sj}(t)[1-\hat{n}_{gj}(t)] + \sum_{s}\frac{\omega_a}{\hbar}\hat{\mu}_{sj}(t)\hat{A}_{\mathrm{s}}(\mathbf{r}_{nj},t) - \hat{\Gamma}_{n_{sj}}(t)\,, \tag{3.11}$$

where $\hat{\Gamma}$'s are the Langevin noise operators with zero mean [34], γ_{Ns} is the decay rate for upper-level population $\hat{n}_{sj}(t)$, and γ_{Vs} is the dipole dephasing rate for operators $\hat{V}_{sj}(t)$ and

$\hat{V}_{sj}^{\dagger}(t)$ that constitute the atomic dipole moment operator vector $\hat{\boldsymbol{\mu}}_j(t)$. Note that $\gamma_{Vs} = \gamma_{Ns}/2 + \gamma_{ph}$ where γ_{ph} is the additional dephasing rate due to $\hat{H}_{ph}$ [29]. Taking the mean values of these equations will give us a set of mean-valued equations for the electron variables, which are used in the next section. The top two equations of Eqs. (3.11) can be used to derive a second-order differential equation for the dipole [21-24]. If we specialize to only the two-level transition between one of the $\hat{n}_{sj}(t)$ and $\hat{n}_{gj}(t)$ for simplicity, we will obtain the following equation:

$$\frac{\partial^2 \hat{\mu}_{sj}(t)}{\partial t^2} + 2\gamma_{Vs}\frac{\partial \hat{\mu}_{sj}(t)}{\partial t} + [\omega_a^2 + \frac{(2\omega_a)^2}{\hbar^2}\left|\mu_{sj}\right|^2 \hat{A}_s^2(\mathbf{r}_{nj}, t)]\hat{\mu}_{sj}(t)$$

$$= -2\frac{\omega_a}{\hbar}\left|\mu_{sj}\right|^2 [\hat{n}_{sj}(t) - \hat{n}_{gj}(t)]\hat{E}_s(\mathbf{r}_{nj}, t), \tag{3.12}$$

where we have dropped small terms by assuming that $\Omega_m >> \gamma_{Vs}, \gamma_{Ns}$. The $\hat{A}_s^2$ term in Eq. (3.12) will affect Rabi oscillation but can be neglected at low intensity. Eq. (3.12) and the bottom two equations of Eqs. (3.11) together forms the complete set of equations for the medium variables.

3.5 Summary of medium-field equations for the Multi-Level Multi-Electron FDTD Model

Using the equations derived in sections 3.3 and 3.4 to describe the interband transitions, we further include the intraband transitions phenomenologically in the rate equations with the corresponding Pauli Exclusion decay terms [21-24] and obtain the full set of mean-valued

equations describing the multi-level multi-electron model below. For simplicity, we consider only one polarization direction (z) from now on and consider only *s*=z in all equations.

To begin with, we start with the Maxwell equations in which the electromagnetic field is coupled to the macroscopic polarization density $\mathbf{P}(\mathbf{r},t)$.

$$\frac{\mathrm{d}\mathbf{H}(\mathbf{r},t)}{\mathrm{d}t} = -\frac{1}{\mu_0}\nabla\times\mathbf{E}(\mathbf{r},t)\ ;\ \frac{\mathrm{d}\mathbf{E}(\mathbf{r},t)}{\mathrm{d}t} = \frac{1}{\varepsilon_0 n^2}\nabla\times\mathbf{H}(\mathbf{r},t) - \frac{1}{\varepsilon_0 n^2}\frac{\mathrm{d}\mathbf{P}(\mathbf{r},t)}{\mathrm{d}t}. \tag{3.13}$$

Let the z-component of $\mathbf{P}(\mathbf{r},t)$ be given by $P_z(\mathbf{r},t) = \mathbf{e}_z\cdot\mathbf{P}(\mathbf{r},t)$. The macroscopic polarization density $P_z(\mathbf{r},t)$ represents the total dipole moment per unit volume. In FDTD, the spatial region is subdivided into volume δV that is small compared to the wavelength of interest. The atomic dipole moment μ_{zj} (t) at $\mathbf{r}_{nj}$ multiplied by the total number of dipoles N_0 (in volume δV) divided by δV will give $P_z(\mathbf{r},t)$. Let the spatial region centered at $\mathbf{r}_{nj}$ with volume δV be denoted as ($\mathbf{r}_{nj}$, δV), we can then express $P_z(\mathbf{r},t)$ as follows:

$$P_z(\mathbf{r},t)\,|_{\mathbf{r}\in(\mathbf{r}_{nj},\delta V)} = \frac{N_0\mu_{zj}(t)}{\delta V} = \mu_{zj}(t)N_{\text{dip-}i}(\mathbf{r}), \tag{3.14}$$

where $N_{\text{dip-}i}(\mathbf{r})$ is the dipole volume density given by the number of dipoles N_0 divided by volume δV. We will assign one macroscopic polarization density variable $P_z(\mathbf{r},t)$ for each of the transition energy E_i between the levels *i_c* and *i_v*. Thus N_0 will include the dipoles describing transitions centered at transition energy E_i within energy width δE and volume δV, so $N_{\text{dip-}i}(\mathbf{r})$ will be the volume density of dipoles for level *i* within energy width δE. We may thus further label $P_z(\mathbf{r},t)$ with subscript *i* as $P_{iz}(\mathbf{r},t)$. Let us denote the volume densities of states for level *i* in

the conduction band and valence band by $N_{Ci}^{0}(\mathbf{r})$ and $N_{Vi}^{0}(\mathbf{r})$, respectively. We can then express the carrier volume densities $N_{Ci}(\mathbf{r},t)$ and $N_{Vi}(\mathbf{r},t)$ (within energy width δE) at levels *i_c* and *i_v*, respectively, in terms of $n_{zj}(t)$ and $n_{gj}(t)$ as $N_{Ci}(\mathbf{r},t)=n_{zj}(t)\cdot N_{Ci}^{0}(\mathbf{r})$ and $N_{Vi}(\mathbf{r},t)=n_{gj}(t)\cdot N_{Vi}^{0}(\mathbf{r})$. In general, $N_{Ci}^{0}(\mathbf{r})$ and $N_{Vi}^{0}(\mathbf{r})$ are not equal, but we will show below that they are equal for a simple parabolic band case. Furthermore, in a more complex semiconductor medium, not all the states are involved in the dipole transitions. Let $N_{Ci}^{A}(\mathbf{r})$ and $N_{Vi}^{A}(\mathbf{r})$ be the active states involving in the dipole transitions having similar dipole transition strengths, the volume density of dipoles $N_{\mathrm{dip}-i}(\mathbf{r})$ will be given by the larger one of $N_{Ci}^{A}(\mathbf{r})$ and $N_{Vi}^{A}(\mathbf{r})$ [35].

Using these relations, the polarization equation can be obtained from Eq. (3.12) by multiplying both sides of the equation with $N_{\mathrm{dip}-i}(\mathbf{r}_{nj})$ so that the microscopic dipole moment variable μ_{zj}(t) is replaced by the macroscopic polarization $P_z(\mathbf{r}_{nj},t)$, labeled as $P_{iz}(\mathbf{r}_{nj},t)$ (*i*=1, 2, …, *M* is the level number). Generalizing it to any position $\mathbf{r}\in(\mathbf{r}_{nj},\delta V)$ and we obtain:

$$\frac{d^2P_{iz}(\mathbf{r},t)}{dt^2}+\gamma_i\frac{dP_{iz}(\mathbf{r},t)}{dt}+[\omega_{ai}^2+\frac{(2\omega_{ai})^2}{\hbar^2}|\mu_{zi}|^2A_z^2(\mathbf{r},t)]P_{iz}(\mathbf{r},t)$$

$$=\frac{2\omega_{ai}}{\hbar}|\mu_{zi}|^2[\frac{N_{dip-i}(\mathbf{r})}{N_{Vi}^{0}(\mathbf{r})}N_{Vi}(\mathbf{r},t)-\frac{N_{dip-i}(\mathbf{r})}{N_{Ci}^{0}(\mathbf{r})}N_{Ci}(\mathbf{r},t)]E_z(\mathbf{r},t)\,, \tag{3.15}$$

where μ_{zi} is the z-dipole moment matrix element ${}_j\langle E_{i\_c}|\hat{\mu}_{zj}|E_{i\_v}\rangle_j$ between levels *i_c* and *i_v* and is given by $|\mu_{zi}|^2=(3\pi\hbar\varepsilon_0c^3)/(\omega_{ai}^3\tau_i)$. The rate equations for $N_{Ci}(\mathbf{r},t)$ and $N_{Vi}(\mathbf{r},t)$ in the conduction and valence bands are then given by:

$$\frac{\mathrm{d}N_{Ci}(\mathbf{r},t)}{\mathrm{d}t} = -\Delta N_i(\mathbf{r},t) - \Delta N_{(i,i-1)C}(\mathbf{r},t) + \Delta N_{(i+1,i)C}(\mathbf{r},t) + W_{\mathrm{pump}}(\mathbf{r},t),$$

$$\frac{\mathrm{d}N_{Vi}(\mathbf{r},t)}{\mathrm{d}t} = \Delta N_i(\mathbf{r},t) + \Delta N_{(i+1,i)V}(\mathbf{r},t) - \Delta N_{(i,i-1)V}(\mathbf{r},t) - W_{\mathrm{pump}}(\mathbf{r},t), \tag{3.16}$$

where the ΔN terms on the right hand side describe:

1. Intraband transition for conduction band in which $\Delta N_{(i,i-1)C}(\mathbf{r},t)$ is the number of electrons per unit volume transferred from conduction band level *i_c* to $i-1$_*c* given by:

$$\Delta N_{(i,i-1)C}(\mathbf{r},t) = \frac{N_{Ci}(\mathbf{r},t)[1 - N_{C(i-1)}(\mathbf{r},t)/N^0_{C(i-1)}(\mathbf{r})]}{\tau_{(i,i-1)C}} - \frac{N_{C(i-1)}(\mathbf{r},t)[1 - N_{Ci}(\mathbf{r},t)/N^0_{Ci}(\mathbf{r})]}{\tau_{(i-1,i)C}}.$$

(3.17)

2. Intraband transition for valence band in which $\Delta N_{(i,i\text{-}1)V}$ is the number of electrons per unit volume transferred from valence band level *i_v* to *i*-1_*v* and is given by:

$$\Delta N_{(i,i-1)V}(\mathbf{r},t) = \frac{N_{Vi}(\mathbf{r},t)[1 - N_{V(i-1)}(\mathbf{r},t)/N^0_{V(i-1)}(\mathbf{r})]}{\tau_{(i,i-1)V}} - \frac{N_{V(i-1)}(\mathbf{r},t)[1 - N_{Vi}(\mathbf{r},t)/N^0_{Vi}(\mathbf{r})]}{\tau_{(i-1,i)V}}.$$

(3.18)

3. Interband driven transition (gain or absorption) and spontaneous decay in which ΔN_i is the number of electrons per unit volume transferred from level *i_c* to *i_v* and is given by:

$$\Delta N_i(\mathbf{r},t) = \frac{\omega_{ai}}{\hbar} A_z(\mathbf{r},t) \cdot P_{iz}(\mathbf{r},t) + \frac{N_{Ci}(\mathbf{r},t)[1 - N_{Vi}(\mathbf{r},t)/N^0_{Vi}(\mathbf{r})]}{\tau_i}. \tag{3.19}$$

In Eq. (3.16) we have a pumping term W_{pump} on the right hand side, which allows us to describe electrical pumping. If the current density going into an active material of thickness d is $J(\mathbf{r},t)$ (A/m^2), then W_{pump} is given by $W_{\text{pump}}(\mathbf{r},t) = J(\mathbf{r},t)/(ed)$, where e=1.6×10^{-19}C is the electron charge. The pumping terms are applied to only the largest E_i level to simulate current injection in semiconductor. Optical pumping can be simulated by introducing an optical pumping beam, which will excite carriers from $N_{Vi}(\mathbf{r},t)$ to $N_{Ci}(\mathbf{r},t)$ via the first term in Eq. (3.19).

Note that Eqs. (3.16)-(3.19) conserve the total number of electrons in the conduction band plus the valence band so that the "total density" $N_T(\mathbf{r},t) \equiv N_{CT}(\mathbf{r},t) + N_{VT}(\mathbf{r},t) = N_T(\mathbf{r},0)$ for electrons is time-independent, where $N_{CT}(\mathbf{r},t) = \sum_i N_{Ci}(\mathbf{r},t)$ and $N_{VT}(\mathbf{r},t) = \sum_i N_{Vi}(\mathbf{r},t)$. The field driven transition term in Eq. (3.19) is in the $A \cdot P$ form (instead of the $-E(dP/dt)$ form) valid at far off resonance [21-24]. The A_z^2 term in Eq. (3.15) is important for high field intensity case.

3.6 Discussion on number density

In this section, we discuss the procedure to obtain the corresponding volume density of states in each of the discrete energy levels. To obtain the correct volume density of states, we sum up all the available states within an energy width δE at the particular energy level in the original band structure. In the multi-level model, energy level i will encompass all the optical transitions between energy levels $E_{i-}^B = E_i - (E_i - E_{i-1})/2$ and $E_{i+}^B = E_i + (E_{i+1} - E_i)/2$ as shown in Fig. 3.3. For a parabolic band structure, the volume density of states at each energy level is calculated from the number of states per unit energy per unit volume $\rho(E)$:

$$\rho(E)\mathrm{d}E = \frac{1}{2\pi^2}[\frac{2m^*}{\hbar^2}]^{3/2}\Delta E^{1/2}dE\,, \tag{3.20}$$

where ΔE is the energy measured from the band edges and are denoted as ΔE_{Ci} and ΔE_{Vi} for the conduction band and valence band, respectively. In a standard parabolic band structure, ΔE_{Ci} and ΔE_{Vi} are given by:

$$\Delta E_{Ci} = (E_{i+}^B - E_G)\frac{m_V}{m_V + m_C},\ \Delta E_{Vi} = (E_{i+}^B - E_G)\frac{m_C}{m_V + m_C}, \tag{3.21}$$

where m_C and m_V are the electron and hole effective masses, respectively, and E_G is the bandgap energy. Hence, the volume density of states for energy level *i*, which is the number of states per unit volume with interband transition energy between E_{i-}^B and E_{i+}^B, will be

$$N_{\mathrm{dip}-i}(\mathbf{r}) = N_{C,Vi}^0(\mathbf{r}) = \int_{\Delta E_{C,V(i-1)}}^{\Delta E_{C,Vi}} \rho(\Delta E)\mathrm{d}E = \frac{16\sqrt{2}m_C^{3/2}m_V^{3/2}[(E_{i+}^B - E_G)^{3/2} - (E_{i-}^B - E_G)^{3/2}]}{3\pi^2\hbar^3(m_C + m_V)^{3/2}}$$

.

(3.22)

In this case we have $N_{Ci}^0(\mathbf{r}) = N_{Vi}^0(\mathbf{r}) = N_{Ci}^A(\mathbf{r}) = N_{Vi}^A(\mathbf{r})$ and hence can set the volume density of dipoles $N_{\mathrm{dip}-i}(\mathbf{r}) = N_{Vi}^0(\mathbf{r})$. It is interesting to see that in this case the volume density of states for level *i_c* is equal to the volume density of states for level *i_v*. However, because of the difference in the intraband relaxation rates for the electrons in the conduction band and valence band due to their different effective masses [36], the number of electrons and holes in the corresponding levels *i_c* and *i-v* may not be equal.

3.7 Modeling the Fermi-Dirac Thermalization Dynamics

At finite temperature, non-equilibrium electrons will transfer between intraband states through phonon-assisted processes to achieve a quasi-equilibrium distribution, which is referred to as the conduction band or valence band Fermi-Dirac thermalization. This effect is often modeled by calculating the quasi-equilibrium Fermi energy levels for both electrons and holes. In a time-domain numerical method, the Fermi energy levels will need to be updated temporally, resulting in complicated calculations. In our model, we will show that the Fermi-Dirac thermalization can be accurately achieved by assigning the right ratio between the upward and downward intraband transition rates between two neighboring levels. The upward transition mimics thermally excited carrier hopping. It turns out that the ratios between the upward and downward intraband transition rates are independent on the Fermi energy levels, which greatly simplify the simulation. To show that, let us illustrate using the intraband transition rate equation between the conduction band levels *i*_*c* and *i*-1_*c* given by Eq. (3.17) as follows:

$$\Delta N_{(i,i-1)C}(\mathbf{r},t)=\frac{N_{Ci}(\mathbf{r},t)[1-N_{C(i-1)}(\mathbf{r},t)/N^{0}_{C(i-1)}(\mathbf{r})]}{\tau_{(i,i-1)C}}-\frac{N_{C(i-1)}(\mathbf{r},t)[1-N_{Ci}(\mathbf{r},t)/N^{0}_{Ci}(\mathbf{r})]}{\tau_{(i-1,i)C}}. \tag{3.23}$$

When the intraband transition between those two levels reaches steady state, we can set $\Delta N_{(i,i-1)C}=0$. The ratio for the upward transition rate $\tau_{(i-1,i)C}$ and downward transition rate $\tau_{(i,i-1)C}$ between levels *i*_*c* and *i*-1_*c* is then given by:

$$\frac{\tau_{(i-1,i)C}}{\tau_{(i,i-1)C}}=\frac{N_{C(i-1)\_S}(\mathbf{r})[1-N_{Ci\_S}(\mathbf{r})/N^{0}_{Ci}(\mathbf{r})]}{N_{Ci\_S}(\mathbf{r})[1-N_{C(i-1)\_S}(\mathbf{r})/N^{0}_{C(i-1)}(\mathbf{r})]}, \tag{3.24}$$

where N_{Ci_S} and $N_{C(i-1)\_S}$ are the steady-state carrier densities in levels *i_c* and *i*-1_*c* that shall obey the Fermi-Dirac thermal distribution function as follows:

$$N_{Ci\_S} = f(\Delta E_{Ci}) \cdot N_{Ci}^{0}(\mathbf{r}) = \frac{1}{e^{[(E_{Ci}-E_{F_C})/k_B T]}+1} \cdot N_{Ci}^{0}(\mathbf{r}), \tag{3.25}$$

where E_{Ci} is the energy of level *i_c* and E_{F_C} is the Fermi energy for the conduction band, both measured with respect to conduction band edge. This gives:

$$\frac{\tau_{(i-1,i)C}}{\tau_{(i,i-1)C}} = \frac{\dfrac{1}{e^{((E_{C(i-1)}-E_{F_C})/k_B T)}+1} \cdot N_{C(i-1)}^{0}(\mathbf{r}) \dfrac{e^{((E_{Ci}-E_{F_C})/k_B T)}}{e^{((E_{Ci}-E_{F_C})/k_B T)}+1}}{\dfrac{1}{e^{((E_{Ci}-E_{F_C})/k_B T)}+1} \cdot N_{Ci}^{0}(\mathbf{r}) \dfrac{e^{((E_{C(i-1)}-E_{F_C})/k_B T)}}{e^{((E_{C(i-1)}-E_{F_C})/k_B T)}+1}} = \frac{N_{C(i-1)}^{0}(\mathbf{r})}{N_{Ci}^{0}(\mathbf{r})} e^{(E_{Ci}-E_{C(i-1)})/k_B T}. \tag{3.26}$$

Similar relations can be obtained for the valence band case. Thus, we see that the ratio between any adjacent pair of the up and down intraband transition times is only dependent on the energy difference between the two levels involved, the temperature, and the ratio between the volume densities of states for the two levels. It is independent on the Fermi energy levels E_{F_C} and E_{F_V}. This leads to a significant simplification of the simulation as there will be no need to update the Fermi energy level at each spatial grid point. The temperature *T* describes the local crystal lattice temperature of the medium and, if necessary, can be treated as a spatial-temporal parameter $T(\mathbf{r},t)$ determined separately by thermal diffusion equation. This thermalization also applies to interband but large energy gap makes its contribution negligible.

3.8 FDTD implementation

In order to implement FDTD simulation, we divide the spatial region of interest into discrete spatial grid points [17]. We assume the dipole to be all in the z-direction. In this case only E_z will be interacting with the medium. We use v, u, w to label the spatial grid points in the x, y, z coordinate directions, respectively. The set of discrete difference equations for the carrier's volume-density variables are then given by:

$$N_{Ci}\,|^{n+1}_{u-1/2,v+1/2,w} = N_{Ci}\,|^{n-1}_{u-1/2,v+1/2,w} + 2\Delta t(-\Delta N_i\,|^{n}_{u-1/2,v+1/2,w} - \Delta N_{(i,i-1)C}\,|^{n}_{u-1/2,v+1/2,w} + \Delta N_{(i+1,i)C}\,|^{n}_{u-1/2,v+1/2,w} + W_{\text{pump}}),$$

$$N_{Vi}\,|^{n+1}_{u-1/2,v+1/2,w} = N_{Vi}\,|^{n-1}_{u-1/2,v+1/2,w} + 2\Delta t(\Delta N_i\,|^{n}_{u-1/2,v+1/2,w} - \Delta N_{(i,i-1)V}\,|^{n}_{u-1/2,v+1/2,w} + \Delta N_{(i+1,i)V}\,|^{n}_{u-1/2,v+1/2,w} - W_{\text{pump}}),$$

$$\Delta N_i\,|^{n}_{u-1/2,v+1/2,w} = \frac{\omega_{ai}}{\hbar} A_z\,|^{n}_{u-1/2,v+1/2,w} \cdot P_{iz}\,|^{n}_{u-1/2,v+1/2,w} + \frac{N_{Ci}\,|^{n}_{u-1/2,v+1/2,w}\,(1 - N_{Vi}\,|^{n}_{u-1/2,v+1/2,w} / N^{0}_{iV}\,|_{u-1/2,v+1/2,w})}{\tau_i},$$

$$\Delta N_{(i,i-1)C}\,|^{n}_{u-1/2,v+1/2,w} = \frac{N_{Ci}\,|^{n}_{u-1/2,v+1/2,w}\,[1 - N_{C(i-1)}\,|^{n}_{u-1/2,v+1/2,w} / N^{0}_{(i-1)C}\,|_{u-1/2,v+1/2,w}]}{\tau_{(i,i-1)C}} - \frac{N_{C(i-1)}\,|^{n}_{u-1/2,v+1/2,w}\,[1 - N_{Ci}\,|^{n}_{u-1/2,v+1/2,w} / N^{0}_{iC}\,|_{u-1/2,v+1/2,w}]}{\tau_{(i-1,i)C}},$$

$$\Delta N_{(i,i-1)V}\,|^{n}_{u-1/2,v+1/2,w} = \frac{N_{Vi}\,|^{n}_{u-1/2,v+1/2,w}\,[1 - N_{V(i-1)}\,|^{n}_{u-1/2,v+1/2,w} / N^{0}_{(i-1)V}\,|_{u-1/2,v+1/2,w}]}{\tau_{(i,i-1)V}} - \frac{N_{V(i-1)}\,|^{n}_{u-1/2,v+1/2,w}\,[1 - N_{Vi}\,|^{n}_{u-1/2,v+1/2,w} / N^{0}_{iV}\,|_{u-1/2,v+1/2,w}]}{\tau_{(i-1,i)V}},$$

$$\sum_{i=1}^{M} N_{Ci}\,|_{u-1/2,v+1/2,w}^{n+1} + \sum_{i=1}^{M} N_{Vi}\,|_{u-1/2,v+1/2,w}^{n+1} = \sum_{i=1}^{M} N_{iC}^{0}\,|_{u-1/2,v+1/2,w} = \sum_{i=1}^{M} N_{iV}^{0}\,|_{u-1/2,v+1/2,w} \,. \tag{3.27}$$

For the macroscopic polarization, we have:

$$\begin{aligned} & P_{i,z}\,|_{u-1/2,v+1/2,w}^{n+1} \\ & = \frac{4-2\Delta t^2(\omega_{ai}^2 + 4\frac{\omega_{ai}^2}{\hbar^2}|\mu_i|^2 A_z^2\,|_{u-1/2,v+1/2,w}^{n})}{2+\Delta t\cdot\gamma_i} P_{i,z}\,|_{u-1/2,v+1/2,w}^{n} + \frac{\Delta t\cdot\gamma_i - 2}{2+\Delta t\cdot\gamma_i} P_{i,z}\,|_{u-1/2,v+1/2,w}^{n-1} \\ & - \frac{4\Delta t^2\omega_{ai}}{\hbar(2+\Delta t\cdot\gamma_i)}|\mu_i|^2 (N_{Ci}\,|_{u-1/2,v+1/2,w}^{n} - N_{Vi}\,|_{u-1/2,v+1/2,w}^{n}) E_z\,|_{u-1/2,v+1/2,w}^{n} \quad . \end{aligned} \tag{3.28}$$

The update of the electrical field components in z direction will be:

$$\begin{aligned} E_z\,|_{u-1/2,v+1/2,w}^{n+1} &= E_z\,|_{u-1/2,v+1/2,w}^{n} - \frac{1}{\varepsilon}\sum_{i=1}^{M}(P_{i,z}\,|_{u-1/2,v+1/2,w}^{n+1} - P_{i,z}\,|_{u-1/2,v+1/2,w}^{n}) \\ &+ \frac{\Delta t}{\varepsilon\Delta x}(H_y\,|_{u,v+1/2,w}^{n+1/2} - H_y\,|_{u-1,v+1/2,w}^{n+1/2}) - \frac{\Delta t}{\varepsilon\Delta y}(H_x\,|_{u-1/2,v+1,w}^{n+1/2} - H_x\,|_{u-1/2,v,w}^{n+1/2}) \,. \end{aligned} \tag{3.29}$$

All other electric and magnetic field components (E_x, E_y, H_x, H_y, H_z) follow the usual updating scheme in Yee's algorithm [17].

3.9 FDTD simulation examples

In order to validate the DTEQM approach for FDTD computation of complex media, we will give several simulation examples using the model discussed above. We assume a semiconductor bulk medium with bandgap wavelength of 1550nm and model it with the simple

parabolic band case. The effective masses for the conduction and valence bands are $0.046m_e$ and $0.36m_e$, respectively, with m_e being the free electron mass. The energy levels E_i's are spaced by constant wavelength spacing $\Delta\lambda$. If we use 5 energy levels for conduction and valence band and let $\Delta\lambda$=50nm, then the optical transition wavelengths for the discrete levels will be 1525nm, 1475nm, 1425nm, 1375nm, and 1325nm. The interband decay rate τ_i for typical direct-gap semiconductor bulk medium and quantum well of interest ranges from hundreds of picoseconds to nanoseconds [37]. In the simulation below we use τ_i=1nsec.

For illustration purpose, we set the downward intraband transition time $\tau_{(i,i\text{-}1)C}$ for conduction band electrons to be about one picosecond and set the downward intraband transition time $\tau_{(i\text{-}1,\ i)V}$ for valence band electrons to be about 100fs, which are within the range of values given in the literature [36]. The upward intraband transitions for conduction and valence bands are then set to follow the ratio given in Eq. (3.26). The initial random distribution of carriers will relax to the quasi-steady-state Fermi-Dirac distribution within the time scale given by the intraband transition rates. The dipole dephasing time is set to be ~50fsec. As those medium time-constants are several orders of magnitude larger than the optical period, it will not affect the choice of the FDTD time step (typically 1-2 orders of magnitude smaller than the optical period).

Application to stead- state absorption spectrum – band filling effect

To show the band-filling effect, we used the semiconductor medium parameters discussed above and studied its steady-state absorption spectrum. We simulated the same medium using both 5 energy levels and 10 energy levels. The total valence band volume density of states N_{VT}^0 obtained by summing over all levels in the valence band are kept to be the same at

N_{VT}^{0} ~7×10^{23} m^{-3} to give reasonable bulk absorption coefficient. We electrically pumped a 2 μm long semiconductor medium along a 1 μm wide waveguide to different carrier densities. After a time period of constant pumping, the carrier density in the medium will reach steady state. A weak and short optical pulse (300fs FWHM) is then launched into the semiconductor waveguide and propagated through the medium as a probing signal to obtain medium information such as the absorption spectrum.

The absorption spectrum is calculated from the Fourier Transform of the output pulse comparing to the input pulse. The result is plotted in Fig. 3.4, where Fig. 3.4(a) shows the spectrum when 5 energy levels are used for the conduction and valence bands and Fig. 3.4(b) shows the spectrum when 10 energy levels are used with $\Delta\lambda$=25nm. Comparing the result of Fig. 3.4 with the typical semiconductor gain/absorption spectrum [38], we see the expected gain spectrum broadening and the shift in the peak wavelength of the gain spectrum with increasing carrier density. The gain spectrum broadening is a result of band filling and is the main reason why it is it difficult to get high inversion in semiconductor amplifiers. Although the 10-level case gives much smoother spectrum, the 5-level case can already show the essential effect covering a broad wavelength range from 1300nm to 1600nm. In many device applications, the spectral coverage does not have to be that broad and fewer levels covering ~ 100 nm can be used.

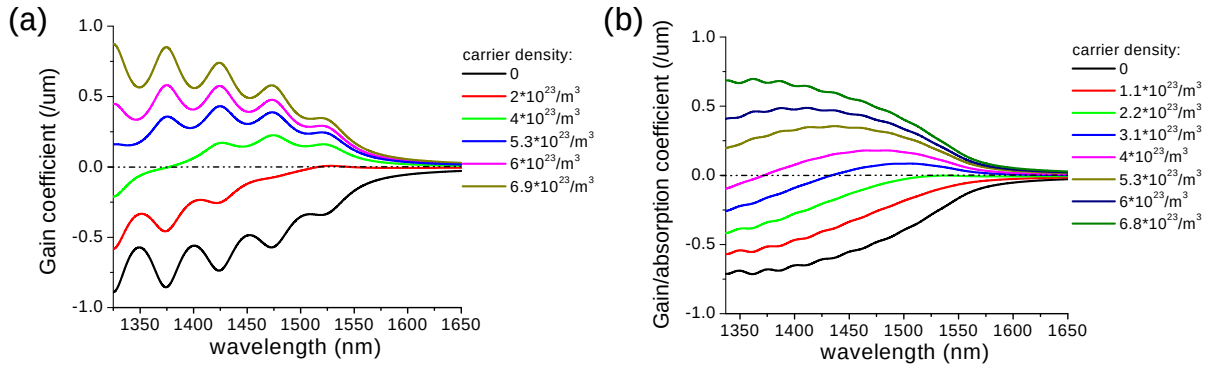

Fig. 3.4 Absorption spectra at different carrier densities obtained by using different number of energy level pairs: (a) 5 level pairs, (b) 10 level pairs.

Application to ultrafast transient response

The absorption of a short laser pulse with an optical frequency above the bandgap in a semiconductor creates free electrons and holes with an initial energy distribution that is essentially determined by the optical spectrum of the laser pulse. Within a very short time scale, this non-thermal energy distribution is transformed by carrier-carrier scattering into a quasi-equilibrium Fermi-Dirac distribution [25, 26]. This process of spectral hole burning and subsequent thermalization is a representative example of ultrafast phenomena in semiconductor [39]. Fig. 3.5 shows the normalized number density in the discrete energy levels as a function of time when the semiconductor waveguide is pumped by a 300fs Gaussian pulse with a peak intensity of 200MW/cm^2 and a center wavelength of 1425nm. We see that the electrons in the valence band relax to quasi equilibrium much faster than the electrons in the conduction band,

exemplified by the steeper slope of the valence band electron relaxation curves. The transient evolution of the entire absorption spectrum can also be obtained [28].

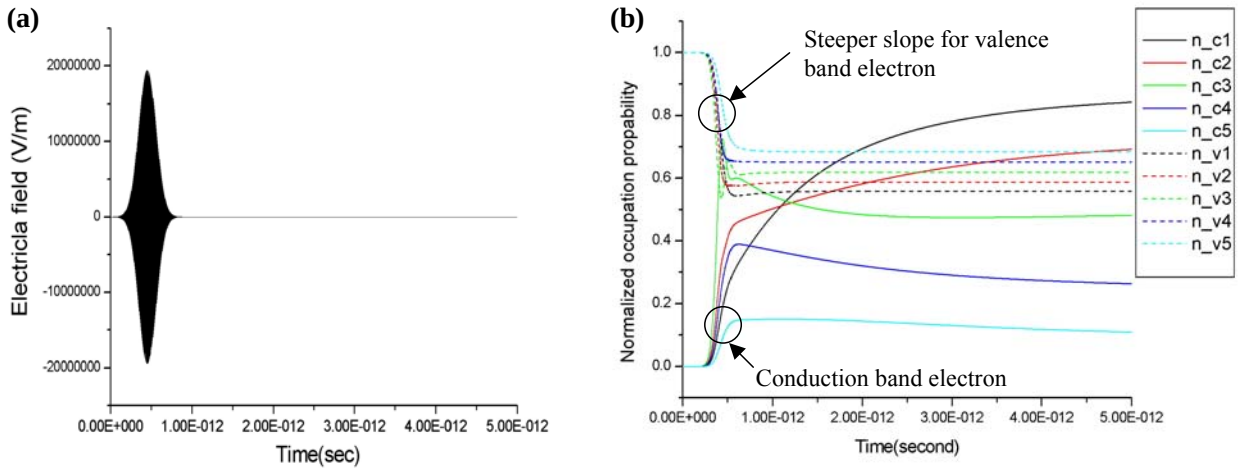

Fig. 3.5 Medium's transient response under strong optical pumping: (a) input optical pulse; (b) normalized volume density of states at each of the 5 energy levels in the conduction and valence band as a function of time.

Application to simulation of multimode microdisk laser

Next we apply the DSM-FDTD model to simulate the lasing behavior of a microdisk semiconductor laser [40-42] using 2-dimensional FDTD with the 5-level model on a 2GHz cpu Pentium PC. The laser gain medium is a semiconductor bulk medium given by the example above in Fig. 3.4(a). Let us consider a 2-μm diameter (Fig. 3.6(a)) microdisk for which the effective waveguiding refractive index of the disk is n=2.7 and the disk is held in air (n=1) by a pillar at the center of the disk. Here we assume the optical mode has 40% overlapping with the active medium in the vertical direction.

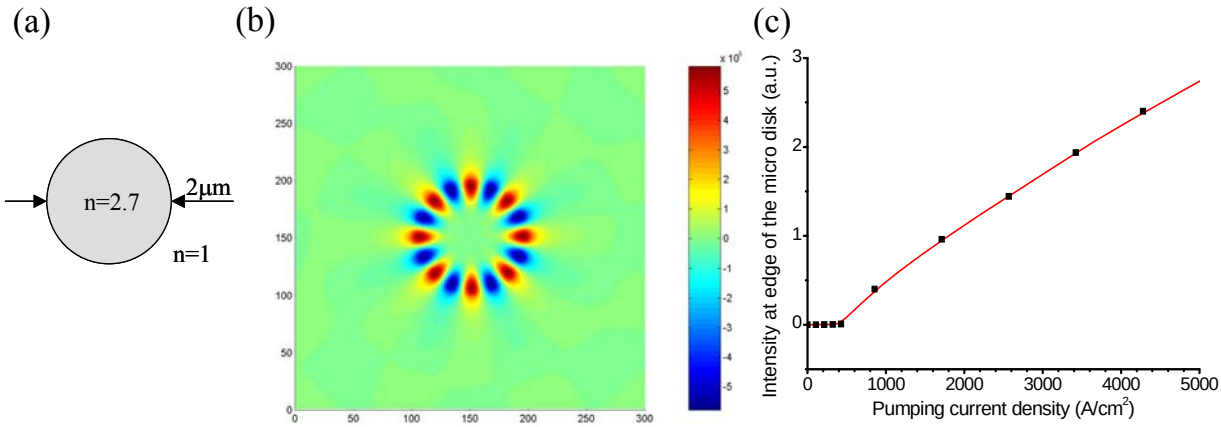

Fig. 3.6 Simulation of microdisk laser: (a) dimension and refractive index of the microdisk laser; (b) simulated electrical field pattern when lasing; (c) optical intensity inside the microdisk laser at different injection current densities.

We pumped the disk with different electrical current densities and plotted the optical intensity inside the disk as a function of the injection current density (Figs. 3.6(b) and 3.6(c)). As spontaneous emission noise is not yet included in the theory, the medium is hit with an optical pulse to initiate lasing. After that self-sustained lasing behavior can be achieved at above threshold. In our simulation, we ran for ~2000 cavity round trips to achieve the steady state and used a FDTD spatial grid resolution of ~λ/30. The laser simulated showed a threshold current density of ~400A/cm^2, which corresponded to a carrier density of 2.5×10^{23} m^{-3}. This carrier density is above the transparent carrier density of 2×10^{23} m^{-3} shown in Fig. 3.4. The lasing spectrum inside the cavity is plotted at four different current levels above threshold as shown in Fig. 3.7(a). At current just above threshold, only one lasing mode is present. At pumping current density 48kA/cm^2, the second mode starts to appear. The two modes are the $TM0_{8,1}$ and $TM0_{9,1}$ whispering gallery modes of the microdisk cavity. Note that the lasing spectral width shown here

is not the real laser linewidth as noise is not included in the current model. The "linewidth" here is actually transform-limited linewidth and is resulted from the limited time period in which we performed Fourier transform on the laser cavity field.

Another interesting effect is that as the pumping level increases, the carrier level increases inside the microdisk due to band filing. This leads to a change in the refractive index ($\Delta n \sim 0.003$) of the microdisk cavity, which then leads to a change in the lasing wavelength. Fig. 3.7(b) shows the slight shift in the lasing wavelength as the injection current level increases. The intensity-induced lasing wavelength change as well as the multi-mode lasing effect would be difficult to simulate without the sophisticated semiconductor model introduced here.

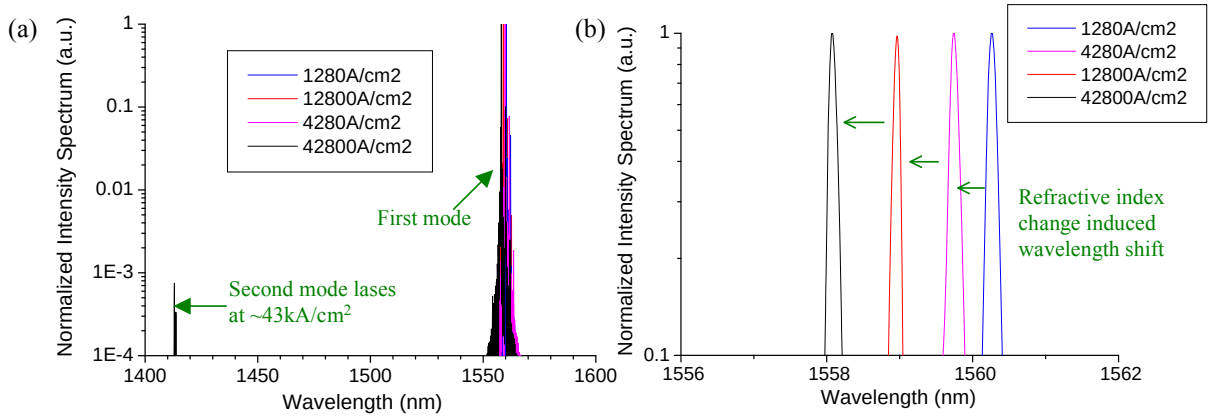

Fig. 3.7 (a) lasing spectra of the 2μm diameter microdisk laser at different injection current densities showing multimode lasing at high current of 43kA/cm^2 (b) zoom in to show the wavelength shift in the first lasing mode.

3.10 Computational overhead and FDTD medium model extension

Perhaps the most important criteria in evaluating the feasibility of a FDTD semiconductor model is its computational complexity, which resulted in long computational time. The DSM-FDTD model illustrated in this dissertation gives a semiconductor model with minimal computational complexity that can still take into account the essential semiconductor carrier dynamics such as band filling, carrier transient effects, and carrier induced refractive index change. When using 5 energy-level pairs for the conduction band and valence band, the total computational time for a simulation where the entire geometry is filled with the semiconductor medium is 8 times of the same code without the medium. In a typical geometry, the active medium may occupy only a small fraction of the entire area of simulation, which can be on the order of 10%. In that case the computational overhead is only ~ 1x. This makes the model useful for a wide range of FDTD simulations.

Although the current model has taken into account most of the essential semiconductor carrier dynamics, there are other effects that could potentially be included in the model depending on the particular device simulation requirements. For example, carrier diffusion could be include into the FDTD equation straight-forwardly by adding a spatial carrier transportation term in Eq. (27). Noise term can be included to give the spontaneous emission linewidth and the lasing linewidth. Carrier heating and cooling can be more accurately described by allowing the carrier temperature to evolve in time. Also, non-radiative and higher-order Auger recombination effects can be included [25, 26]. Furthermore, quantum well and dot and their carrier capture dynamics can be modeled. However, one should only include the most essential effects sufficient for simulating the device behaviors of interest to reduce the computational burden.

3.11 Reduced Medium Method

The simulation of structure with active medium is much more computationally complex than a passive structure. We may try to use coarser resolution for numbers of the dipoles representing the active medium. The idea is that instead of assigning active dipole to every grid, we just assign one active dipole in every n*n grid region. Several tests have been done to examine the validity of this approach.

The speed-up by using reduced medium method for simulation of a region that consists of all active mediums is illustrated in Fig. 3.8. Even only use a reduced medium factor of 2 will reduce the total simulation time drastically.

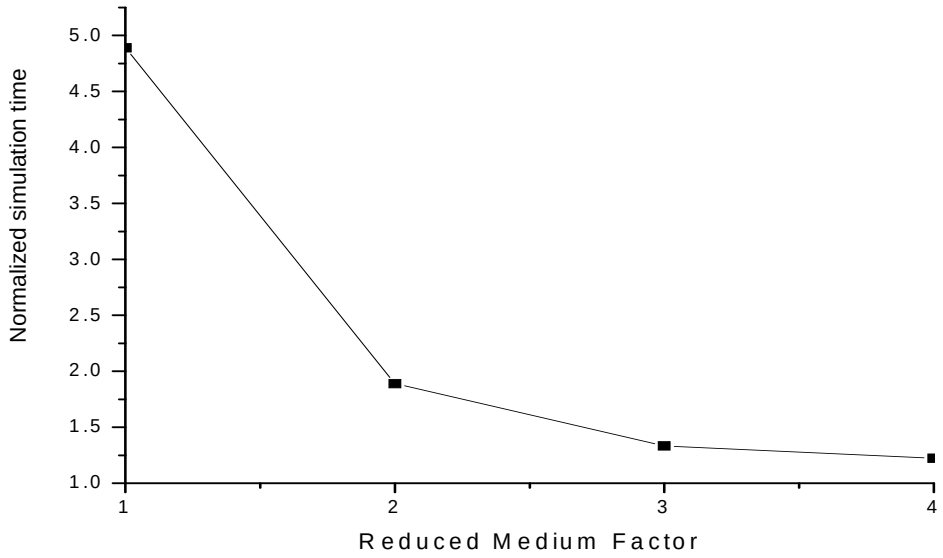

Fig. 3.8 Speed-up by using reduced medium method

3.12 Discussion and summary

In summary, we report a new computational model of material media capable of modeling the nanostructure and electronic dynamics of sophisticated active materials often needed in photonic device simulations. The media that can be modeled include solid-state and semiconductor type media, as well as molecular and atomic type media. This model is computationally efficient for incorporating into the FDTD electrodynamics simulation.

The model is based on a multi-energy-level multi-electron quantum system in which the electron dynamics is governed by the Pauli Exclusion Principle and the dynamical Fermi-Dirac Thermalization. The medium is described by a set of rate equations derived quantum mechanically. The formulation is based on the basic minimal-coupling Hamiltonian extended to incorporate multiple electrons via second quantization using Fermion creation and annihilation operators. The set of rate equations and dipole equation describing the model are obtained without the usual rotating-wave approximations and can be applied to the regimes at near or far off-resonance as well as high field intensity.

We refer to this model as the Dynamical-Thermal-Electron Quantum-Medium FDTD (DTEQM-FDTD) model. It is built on top of our earlier 4-level 2-electron model with Pauli Exclusion Principle [21-24] but extended to multiple levels and multiple electrons with the important inclusion of dynamical Fermi Dirac thermalization. We show that the Fermi-Dirac thermalization can be incorporated via a temperature-dependent carrier hopping process, which mimics thermal carrier excitations. This dynamical process enables the simulation of carrier

decay from non-thermal equilibrium after excitation to a quasi equilibrium carrier distribution governed by the quasi Fermi-Dirac distribution.

In application to semiconductor, this DTEQM-FDTD model takes into account the transient intraband and interband electron dynamics, the semiconductor band structure, and carrier thermal equilibrium process for the first time in FDTD simulation, and is referred to as the Dynamical-Semiconductor-Medium FDTD (DSM-FDTD) model. The DSM-FDTD model automatically incorporates energy-state filling effect. It also incorporates the typical nonlinear optical effects associated with carrier dynamics and thermally activated carrier scattering process under transient excitation spatial-temporally. The model also allows separate electron dynamics in the conduction and valence bands. These capabilities empower the model to treat sophisticated optoelectronic and nanophotonic devices having complex geometries with full spatial-temporal solutions at the microscopic level under electrical or optical excitation. A further extension of the FDTD model to include spatial diffusion of carriers, lattice temperature heating or cooling, and carrier dependent medium parameter shifts due to many-body effects will make it a highly powerful optoelectronic and photonic device simulator.

Most importantly, we show that the FDTD model is sophisticated enough to incorporate the essential multi-physical effects in complex media and yet is simple enough to achieve fast computational time. We illustrated the application of this powerful new model to FDTD computation with the simulation of the entire gain and absorption spectra of a direct-bandgap semiconductor medium, showing the carrier band filling effects with Fermi-Dirac statistics. We then illustrated the application of the FDTD model to simulating spectral hole burning of carriers under a strong optical pulse with subsequent decay to thermal equilibrium representative of

ultrafast phenomena in semiconductor. To illustrate its applications to photonic devices, we simulated a microdisk laser in which a second lasing mode is excited due to gain bandwidth broadening at high medium excitation. We also show the shift in the lasing frequency with increased excitation due to carrier-induced refractive index change.

CHAPER IV ALL-OPTICAL PHOTONIC TRANSISTOR DEVICES BASED ON GAIN AND ABSORPTION MANIPULATION OF OPTICAL INTEFERENCE (GAMOI)

4.1 Introduction

4.1.1 What is A Photonic Transistor?

To further increase the speed of optical networks, there are substantial interests in exploring the use of all-optical devices to realize 10-100Gbit/s all-optical switching. Beside their high speed, all-optical devices could help to substantially reduce the power consumption of current optical network equipments involving optical-electrical-optical (OEO) conversions [43].

The all-optical devices of interest for high-speed networks include all-optical wavelength converters, all-optical switches, and all-optical logic gates. These all-optical devices will also enable ultrafast all-optical signal processing and computing. The reason why all-optical devices have not yet seen large insertion in practice is because they are still marginal in performance for the desired device properties. The desired properties for an all-optical switching device include:

High speed: High operating speed of 10-100Gbit/s or faster.

Low switching power: Low switching power of several mW so that on-chip semiconductor lasers can be used.

Low throughput loss: Low throughput loss or signal gain (the output or "switched" signal is of comparable or higher power than input signal), which is important for multiple device cascadability.

Switching gain: Switching gain (the control signal or "pump" is of lower power than the input signal being switched), which is important for efficient wavelength conversions or logic gates.

Small device size: Device size of <500μm so that integration density can reach 10-100 device/cm^2.

Pulse reshaping: Some form of pulse reshaping so that the output pulse will not be worse than the input pulse in terms of pulse shape and frequency chirp.

All optical switching devices with switching gain are often compared to electronic transistors and may be called photonic transistors. Fig. 4.1 and Fig. 4.2 show the basic scheme of a photonic transistor. The device operates with two input port and one output port. The two input port include one power supply port and one input signal port, and the output port is where the output signal is drawn. The device can have two different operation modes. In the first operation mode, the power supply beam will be a continues-wave optical beam, which we will refer to as the "DC" mode of operation for the photonic transistor. The power supply beam will be switched out to the output signal port when the input signal pulse is present. In the second mode of operation, he power supply beam itself is in pulse form. Only when both the power supply beam

and the input signal beam are present, the power supply beam will be switched out to the output signal port.

The difference between the photonic transistor and a typical all-optical switching device is that in both operation modes, the optical power of the input signal beam is less than that of the power supply beam and the output signal beam. So the device will have net signal gain, making the resulting optical circuit having high cascadability.

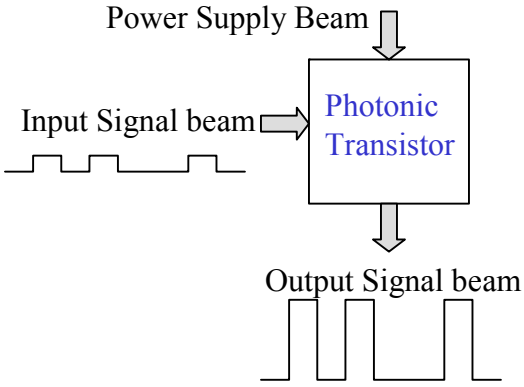

Fig. 4.1 Schematics of a photonic transistor in DC mode

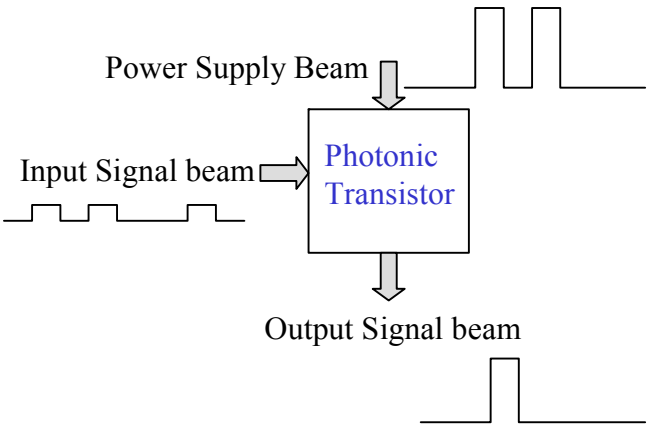

Fig. 4.2 Schematics of a photonic transistor in pulse mode

4.1.2 A comparison between $n^{(2)}$ and $\alpha^{(2)}$ based Optical Switching Devices

While ultrafast all-optical operations can be realized using materials with third-order optical nonlinearity $\chi^{(3)}$ (or nonlinear refractive index $n^{(2)}$), the lack of materials with high enough $\chi^{(3)}$ gives rise to the requirement of needing either very high optical intensity (~10^{10} W/cm^2), long device length (~ km), or narrowband high-Q cavity to compensate the low $\chi^{(3)}$ [44, 45]. The desire for integration makes it even more demanding as it further restricts the class of materials suitable. For example, III-V semiconductors such as GaAs at below half the bandgap energy are suitable for integration and have comparatively high $n^{(2)}$, but as shown experimentally [44, 45], a 1cm-long device still needs switching peak power of ~10W for the control beam even with the use of a strongly confined waveguide with <0.5μm^2 mode area (at λ=1500 nm). While the use of a nano-waveguide similar to that in a photonic-wire laser [42] could reduce the mode area to 0.04 μm^{2}or switching power to ~1W, it would still be 100× higher than the ~10 mW power available from typical semiconductor lasers. Recently, there has also been interest in using the higher though slower $n^{(2)}$ of semiconductor optical amplifiers (SOAs) for 10-100 Gb/s operations, resulting in mm-size devices [46-48]. However, similar problems remain, as each SOA pair requires high electrical power (~0.5W) and careful biasing to operate.

In addition, there are two basic problems with $\chi^{(3)}$ or $n^{(2)}$ materials. First, non-square pulses will experience frequency chirping because the nonlinear phase shift induced will vary with the pulse intensity profile, resulting in spectral broadening under self- or cross- phase modulation. Second, while it is desirable to achieve switching gain so that a weak control beam

can switch a strong signal beam, in practice when the control beam induces π phase shift, the much stronger signal beam will experience self-phase modulation of multiple π, resulting in serious spectral broadening as well as encountering multi-photon absorption. These problems make the devices not very cascadable, which is essential for complex photonic circuits.

Compared to $\chi^{(3)}$, the second order nonlinear gain and absorption coefficient $\alpha^{(2)}$ requires much less optical intensity, thus lead to much less optical power requirement given the same optical mode size. However, while optical gain and absorption have been considered for all-optical operations, they are typically limited by the slow free-carrier decay and lack of switching gain [49]. For example, a straight-forward way to switch an optical beam at a cross-waveguide junction with active medium, as illustrated in Fig. 4.3, is the use of a control-signal beam to pump the medium to gain (or saturate it) and switch the beam through. The medium gain, however, has slow decay time governed by the carrier spontaneous decay. In addition, the optical beam to be switched cannot be of higher power than the control-signal beam, or it would compete with the control-signal beam in saturating the medium. In fact, it would saturate the medium by itself and self-switched through. This makes it impossible to achieve signal switching gain, which will be an essential feature to qualify it as a Photonic Transistor. Nevertheless, the substantial advantage of using gain or absorption is that the switching can be achieved at much lower optical intensity than $\chi^{(3)}$ or $n^{(2)}$.

In fact, it is interesting to compare various types of optical switches to the case of electronic transistors. Electronic transistor is based on the control of electrical resistance closely

analogous to absorption in the case of photons. Electronic transistors do not use higher-order electron nonlinearity to realize transistor action.

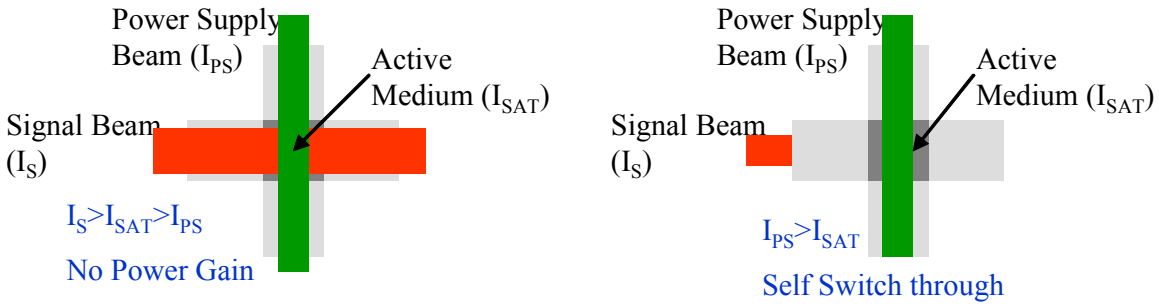

Fig. 4.3 $\alpha^{(2)}$ based all optical switching schemes using cross waveguide.

As can be seen from the example above, the straightforward pump-probe scheme employing an active medium at the cross-section does not work well because of the limitation in switching speed and switching gain. To circumvent these limitations while still keep the low power advantage of gain and absorption, we propose a new all-optical switching device scheme utilizing the modulation of optical interference with changes in medium gain and absorption coefficient. To the best of the author's knowledge, this is the first detailed investigation on how to use absorption and gain changes in active medium to act as all optical photonic transistor devices. As will be shown in details later, this new scheme can achieve highly efficient photonic transistor action, lead to photon energy up or energy down conversion in novel ways. The main innovation in our approach can be summarized as follows:

First of all, optical interference structure is used in combination with the active medium gain and absorption change. The interference structure prevents the power supply beam from self

switching even if the intensity of the power supply beam need to be much higher than the saturation intensity of the medium.

Secondly, two different wavelengths are used for the power supply beam and the input signal beam. Both the power supply beam and the input signal beam can have intensity several orders of magnitude higher than the saturation intensity of the active medium, thus eliminate the device speed limitation imposed by slow carrier decay. Instead, much fast processes such as saturation and stimulated emission is used to switch the device from "on" to "off", and vise verse.

Finally, because it is necessary to use optical beam with two different wavelengths, we propose ways to structure both wavelength up-conversion and down-conversion photonic transistors. Having wavelength up and down conversion capability is essential in all-optical circuits, as one main advantage of an all-optical system compared to an electronic system is its huge bandwidth capability. However, to fully utilize the advantage of optical bandwidth, the system should be able to work with multiple wavelength signals, and realize wavelength conversion between different operating wavelengths when necessary. Thus, the inherent wavelength conversion capability of the photonic transistor devices we proposed here is highly desirable.

We illustrate the new approach here using the case of an optical-interference based directional coupler, in the form of two coupled waveguides, as the interference device. However, the readers should keep in mind that couplers are definitely not the only choice available to introduce the optical interference. As a matter of fact, various other structures, such as multi-mode waveguide interferometers, etc, can be used. Here we focus on the case of the directional

coupler, simply because its familiarity for most researchers in the field, and that it is relatively easy to analyze.

In a directional coupler, the interference of the two symmetric and anti-symmetric guided eigenmodes results in complete energy transfer from one waveguide to another [50]. The optically induced gain and absorption in the coupler can change the interference, resulting in beam switching. We show that for efficient all-optical operations, a novel single active-medium-arm geometry has to be used, and various power-supply beams have to be appropriately introduced to provide the energy needed for achieving high operating speed and signal amplification. For example, it turns out that to induce gain or absorption efficiently, the control-signal beam cannot be at the same wavelength as the power-supply beam.

4.1.3 Photonic Transistors based on Gain and Absorption Manipulation of Optical Interference (GAMOI)

The directional coupler is an interesting device that has been studied quite thoroughly over the past several decades [50]. The most basic form of a directional coupler is two identical waveguides lay in parallel to each other, and separated by certain distance. The optical field entering one waveguide will be coupled to the other waveguide, and vise versa. As a result, the optical power enter one waveguide will be exchanged between the two waveguides periodically. And the length over which the power is exchange complete from one waveguide to another is referred to as one full coupling length.

When the two waveguides in the coupler are non-identical, typically, the power exchange between the two waveguides can no longer be complete. Meanwhile, gain and absorption in one

or both of the waveguides will also drastically change the coupling characteristics, as will be shown later in this chapter. As a result, if either the refractive index or the gain/absorption coefficient of the coupler can be modified in some way, the coupler can act as an optical switching device. This idea is not new and a lot of research efforts have been focused on the directional coupler as optical switching devices [51, 52]. However, most of them are either trying to use the change of refractive index in the coupler through $n^{(2)}$ [52], or employing electrical current to alter the gain and absorption of certain sections of the coupler [51].

We proposed here a new scheme that uses optical pulse to alter the gain or absorption coefficient of the coupler by stimulated emission or saturation, which in turns alters the coupling characteristics of the coupler and lead to the switching. The layout of the device can take various forms. However, we find that the following two schemes are especially of interest and we will discuss them briefly before going into the details of the mathematics.

The energy up photonic transistor

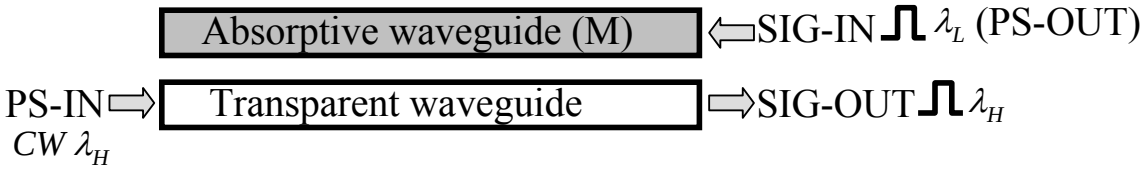

Fig. 4.4 Schematics of energy up photonic transistor

The energy up photonic transistor gets its name from the fact that photons entering the device with lower energy (or longer wavelength λ_L) will be converted to photons with higher energy (or shorter wavelength λ_H). The basic working principle of the device is as follows (Fig. 4.4):

A continues wave (CW) optical beam with wavelength λ_H, enters the coupler from the lower arm (port *PS-IN*). The beam has high enough optical power to saturate the absorptive medium in the upper arm of the coupler so the medium will appear to be transparent to the beam. The length of the coupler is designed to be on full coupling length for wavelength λ_H, so the beam will exit fully from the upper arm (port *PS-OUT*). For a semiconductor material with bandgap energy less than λ_H, transparency at λ_H means gain at the bandgap energy λ_L. When a short signal pulse with wavelength λ_L enters the coupler from the upper arm (port *SIG-IN*), it will see gain and de-excite the medium via stimulated emission. This causes the upper arm to become lossy for λ_H and the $P_{PS\text{-}IN}$ beam will see loss in the upper waveguide. Because of the loss, the small energy leakage to the top waveguide has no chance to build up constructively; resulting in little energy transfer to the top waveguide and a pulse at λ_H will exit the lower arm from port *SIG-OUT*. The net result is an optical pulse at wavelength λ_L is converted to a pulse at wavelength λ_H.

The energy down photonic transistor

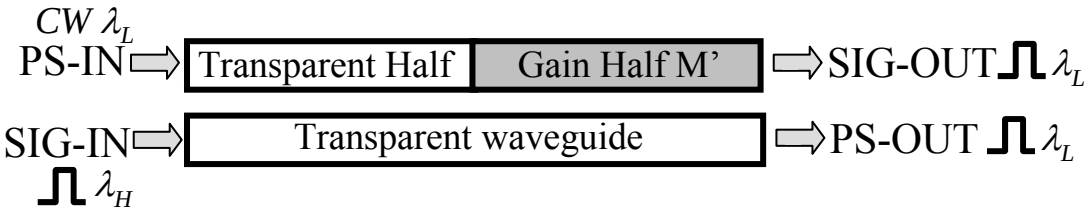

Fig. 4.5 Schematics of energy down photonic transistor

Similarly, the energy down photonic transistor gets its name from the fact that photons entering the device with higher energy (or shorter wavelength λ_H) will be converted to photons with lower energy (or longer wavelength λ_L). The basic working principle of the device is as follows (Fig. 4.5):

A continues wave (CW) optical beam with wavelength λ_L, enters the coupler from the upper arm (port *PS-IN*). The length of the coupler is designed to be on full coupling length for wavelength λ_L, so the beam will exit fully from the lower arm (port *PS-OUT*). When a short signal pulse with wavelength λ_H ($\lambda_H < \lambda_L$) enters the coupler from the lower arm (port *SIG-IN*), it will excite the medium via stimulated emission, causing the right half of the upper arm (the active medium part) to become amplifying for λ_L and part of the beam at wavelength λ_L will exit the upper arm from port *SIG-OUT*. The net result is an optical pulse at shorter wavelength λ_H is converted to a pulse at longer wavelength λ_L.

In the next section, we will discuss in more detail the principle of the gain and absorption manipulation of the coupler interference and how they are used in the design of photonic transistors. As will be shown below, the involvements of optical interference, stimulated decay, and saturation are key factors for achieving fast operation and signal amplification that cannot be achieved otherwise via the conventional geometry of Fig. 4.3.

4.2 Gain and Absorption manipulation of optical Interference

In this section, we will first discuss the basic ideas of the gain and absorption manipulation of optical interference, and then we will explain the operation principle of the energy-up photonic transistor and energy down photonic transistor.

4.2.1 The Coupled Mode Equations

The gain and absorption manipulation of coupler interference (GAMOI) principle we proposed is an expansion of the typical coupled mode theory [44].

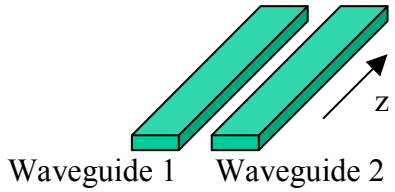

Fig. 4.6 Coupled waveguide structure.

Consider two waveguides in close proximity to each other such that the evanescent field from one waveguide may couple into the other and vice versa, as shown in Fig. 4.6. Let a_1 be the instantaneous field amplitude in one waveguide and a_2 be the instantaneous field amplitude in the other waveguide. The field amplitudes are defined here in terms of power: eg. the power flow in waveguide 1 is given simply by $P_1 = |a_1|^2$.

If we assume that the waveguide 2 has a lossy medium with field absorption coefficient α. As the field propagates a distance Δz in waveguide, the amplitude will change because of the

change in phase of the field, power coupled from the neighboring waveguide, and the medium absorption:

$$\frac{da_2}{dz} = -j\beta_2 a_2 - \alpha a_2 + k_{21} a_1 \tag{4.1}$$

Similarly the field amplitude in the waveguide 1 satisfies:

$$\frac{da_1}{dz} = -j\beta_1 a_1 + k_{12} a_2 \tag{4.2}$$

Equation (4.1) and (4.2) are the coupled mode equations. The constants k_{12} and k_{21} are the coupling coefficients describing the rate that power is transferred from waveguide 1 to waveguide 2 and vice-versa. The coupling coefficients can be estimated using perturbation theory for specified waveguide geometries.

Typical studies on coupled waveguides often assume that power conserves in the system. We investigated the modifications introduced by the gain or absorptive medium, where power conversation no longer holds. Since the change of the optical power comes from the absorption or amplification of the medium, we can write the total power flow along wave propagation direction *z* as follows:

$$\frac{d}{dz}(a_1 a_1^* + a_2 a_2^*) = -2\alpha a_2 a_2^* \tag{4.3}$$

From (1) and (2) we have:

$$a_2 \frac{\partial a_2^*}{\partial z} + a_2^* \frac{\partial a_2}{\partial z} = a_2(j\beta_2 a_2^* - \alpha a_2^* + k_{21}^* a_1^*) + a_2^*(-j\beta_2 a_2 - \alpha a_2 + k_{21} a_1) \tag{4.4}$$

$$a_1 \frac{da_1^*}{dz} + a_1^* \frac{da_1}{dz} = a_1(j\beta_1 a_1^* + k_{12}^* a_2^*) + a_1^*(-j\beta_1 a_1 + k_{12} a_2) \tag{4.5}$$

Substitute (4) & (5) into (3), we will get:

$$a_1 a_2^*(k_{12}^* + k_{21}) + a_2 a_1^*(k_{21}^* + k_{12}) = 0 \tag{4.6}$$

For (6) to hold at any field amplitude, we need $k_{21}^* + k_{12} = 0$.

This result is the same as the power conservation case!

For optical circuits with reciprocity, $k_{21} = k_{12} = K$, so $K^* + K = 0$. K is pure imaginary.

Let $K = -jk$, then (1) & (2) becomes:

$$\frac{da_2}{dz} = -j\beta_2 a_2 - \alpha a_2 - jka_1 \tag{4.7}$$

$$\frac{da_1}{dz} = -j\beta_1 a_1 - jka_2 \tag{4.8}$$

Using the standard Laplace transform, we can obtain the solution for (7) & (8) as

$$a_1(z) = e^{-j\beta_0 z}[a_1(0)\cos(\gamma z) - \frac{j(ka_2(0) + \Delta\beta a_1(0))}{\gamma}\sin(\gamma z)] \tag{4.9}$$

$$a_2(z) = e^{-j\beta_0 z}[a_2(0)\cos(\gamma z) - \frac{j(ka_1(0) - \Delta\beta a_2(0))}{\gamma}\sin(\gamma z)] \tag{4.10}$$

for $\gamma^2 = k^2 + (\Delta\beta)^2 > 0$.

Or

$$a_1(z) = e^{-j\beta_0 z}[a_1(0)ch(|\gamma|z) - \frac{j(ka_2(0) + \Delta\beta a_1(0))}{|\gamma|} sh(|\gamma|z)] \quad (4.9')$$

$$a_2(z) = e^{-j\beta_0 z}[a_2(0)ch(|\gamma|z) - \frac{j(ka_1(0) - \Delta\beta a_2(0))}{|\gamma|} sh(|\gamma|z)] \quad (4.10')$$

for $\gamma^2 = k^2 + (\Delta\beta)^2 < 0$.

where

$$\beta_0 = \frac{\beta_1 + \beta_2 - j\alpha}{2}$$

$$\Delta\beta = \frac{\beta_1 - \beta_2 + j\alpha}{2}.$$

The power exchange between the two waveguides when a unit power input is launched into waveguide 1 at position z=0 can be calculated as follows:

Let $a_1(0) = 1$, $a_2(0) = 0$, $k = \pi/(2L_{cp})$, $\beta_1 = \beta_2$,

Then $\Delta\beta = \frac{j\alpha}{2}$, $\gamma^2 = (\pi/2L_{cp})^2 - \alpha^2/4$

When $\gamma^2 = k^2 + (\Delta\beta)^2 > 0$

$$a_1(z) = e^{-j\beta_1 z} e^{-\alpha z/2}[\cos(\gamma z) + \frac{\alpha/2}{\gamma}\sin(\gamma z)]$$

$$a_2(z) = e^{-j\beta_2 z} e^{-\alpha z/2}[-\frac{jk}{\gamma}\sin(\gamma z)]$$

Power exiting at length Z is:

$$P_1(z) = e^{-\alpha z}[\cos(\gamma z) + \frac{\alpha/2}{\gamma}\sin(\gamma z)]^2 \tag{4.11}$$

$$P_2(z) = e^{-\alpha z}[\frac{k}{\gamma}\sin(\gamma z)]^2 \tag{4.12}$$

When $\gamma^2 = k^2 + (\Delta\beta)^2 < 0$

$|\gamma|^2 = \alpha^2/4 - (\pi/2L_{cp})^2 > 0$

$$a_1(z) = e^{-j\beta_1 z} e^{-\alpha z/2}[ch(|\gamma|z) + \frac{\alpha/2}{|\gamma|} sh(|\gamma|z)]$$

$$a_2(z) = e^{-j\beta_2 z} e^{-\alpha z/2}[-\frac{jk}{|\gamma|} sh(|\gamma|z)]$$

Power exiting at length z is:

$$P_1(z) = e^{-\alpha z}[ch(|\gamma|z) + \frac{\alpha/2}{|\gamma|} sh(|\gamma|z)]^2 \tag{4.11'}$$

$$P_2(z) = e^{-\alpha z}[\frac{k}{|\gamma|} sh(|\gamma|z)]^2 \tag{4.12'}$$

G. H. B. Thompson gave a detailed analysis on optical directional coupler that includes gain or loss in his 1986 paper [53].

So far we have derived the optical power propagation in waveguide couplers with either gain or absorptive sections. Next we will concentrate on some specific scenarios that will be used later in the photonic transistor devices. The first case we investigated is shown in Fig. 4.7. The

coupler structure is designed such that when both waveguides are transparent, the total length will be one full coupling length for the optical beam at certain wavelength. We assume that the top waveguide is filled with absorptive material with a given refractive index. The beam output power from top and bottom waveguide at the output end of the coupler can be plotted out as a function of the product (αL) of absorption coefficient (α) and the coupler length (L). Using the equation we derived above, the result is shown in Fig. 4.8(a). We also used FDTD to simulate the same scenario and the result is shown in Fig. 4.8(b). Excellent agreement between the coupled-mode equation and FDTD simulation is achieved.

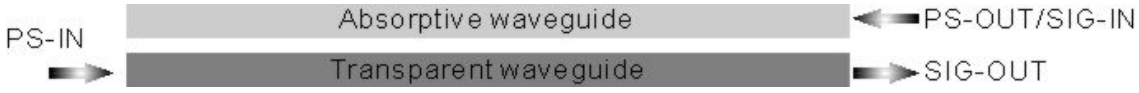

Fig. 4.7 Coupler structure with one waveguide absorptive.

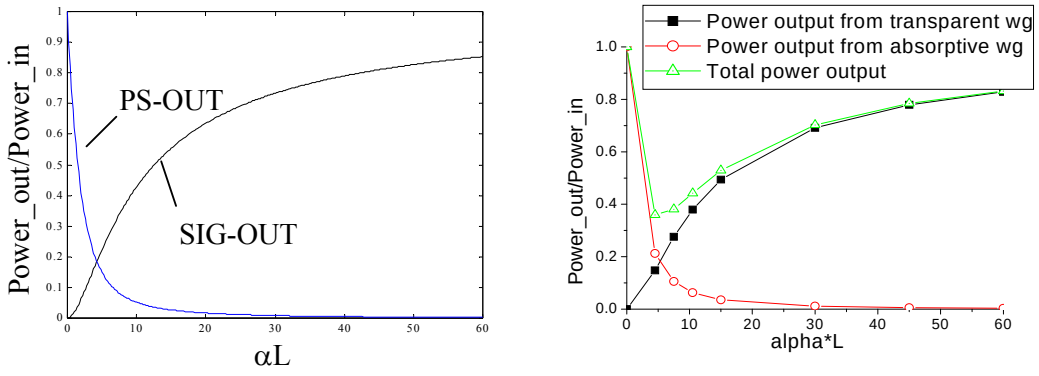

(a) (b)

Fig. 4.8 Beam's normalized output power as function of absorptive coefficient using (a) coupled mode equation and (b) FDTD simulation. All the plots in case I, II, and III has the same definition of axis: Y-axis is the normalized output power, defined as the ratio between the output power and the input power. X-axis is the product (αL) of absorption coefficient (α) and the coupler length (L).

The second case we investigated is shown in Fig. 4.9. The coupler structure is design such that when both waveguides are transparent, the total length will be one full coupling length. We assume that half of the top waveguide is filled with gain material with a given refractive index. The beam output power from top and bottom waveguide at the output end of the coupler can be plotted out as a function of αL. Using the equation we derived above, the result is shown in Fig. 4.10 (a). We also used FDTD to simulate the same scenario and the result is shown in Fig. 4.10 (b).

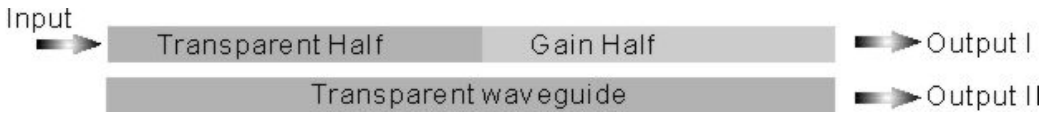

Fig. 4.9 Coupler structure with one waveguide absorptive.

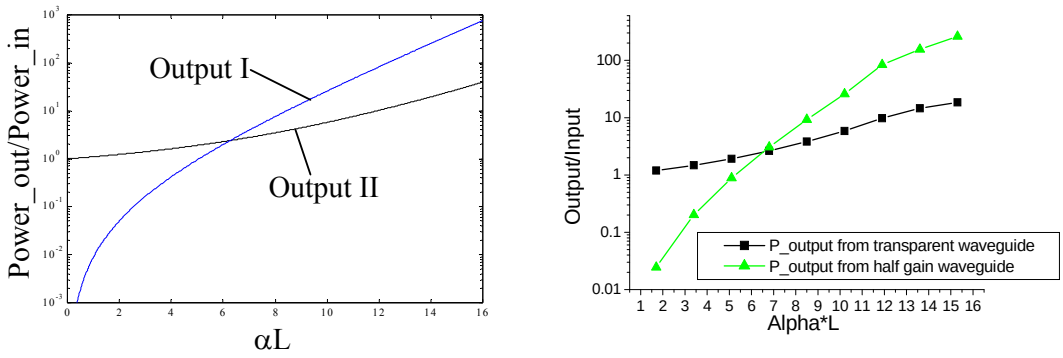

(a) (b)

Fig. 4.10 Normalized beam output power as function of gain coefficient using (a) coupled mode equation and (b) FDTD simulation.

B. Gain length=1/3 total length & Gain length=2/3 total length

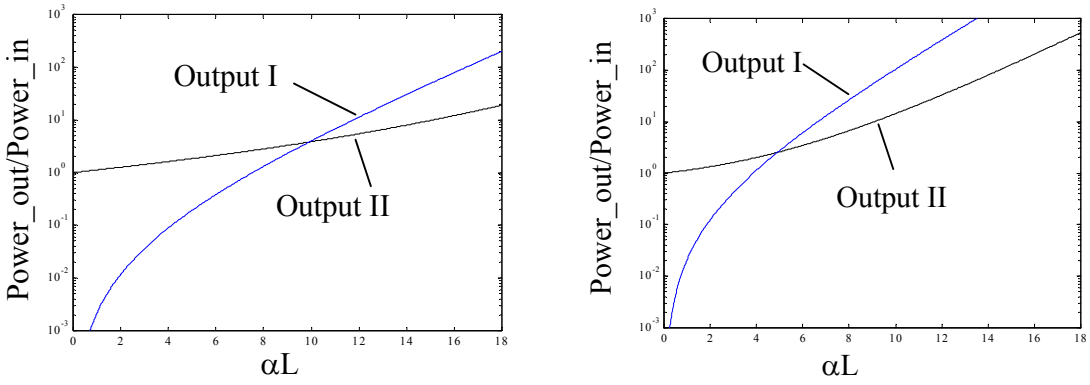

Fig. 4.11 Normalized beam output power as function of gain coefficient when gain region length changes.

If we vary the gain section length, we can see that the point where the two output values equal will happen at smaller αL as gain section length increase.

As a comparison to the second case, we also investigated the scenario where the gain part is in the front half of the top waveguide as shown in Fig. 4.12. The coupler structure is the same as case II, but the gain section is now in the front of the top waveguide. The output from top and bottom waveguide at the output end of the coupler is plotted out as a function of αL as shown in Fig. 4.13(a). We also used FDTD to simulate the same situation and the result is shown in Fig. 4.13(b).

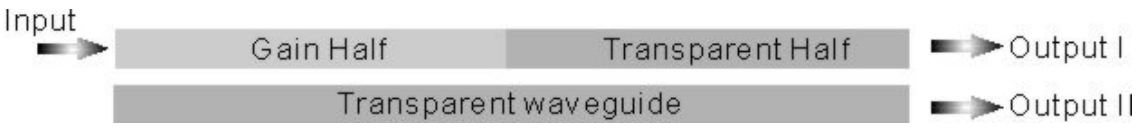

Fig. 4.12 Coupler structure with one waveguide absorptive.

A. Gain =1/2 LC

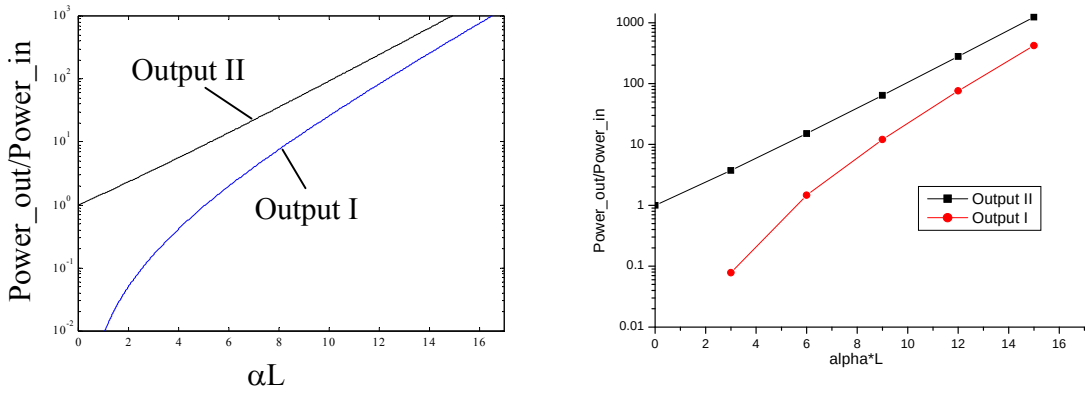

(a) (b)

Fig. 4.13 Normalized beam output power as function of gain coefficient using CME and FDTD simulation.

Comparing Fig 4.13(a) to Fig. 4.10(a), it can be seen that the result of those two cases are quite different. In case III the output from output II is always larger than output I no matter what the value of αL is. Fig. 4.14 shows the output change with different gain section length.

B. Gain =2/3 LC, Gain =3/4 LC and Gain=1 LC (from left to right)

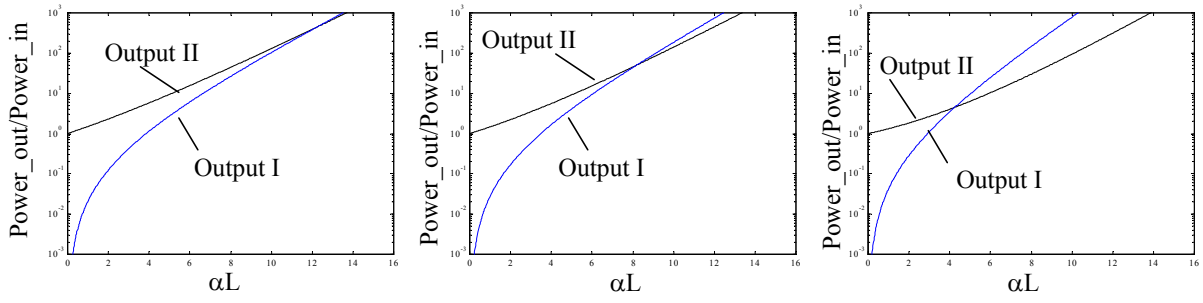

Fig. 4.14 Normalized beam output power as function of gain coefficient when gain region length changes.

4.2.2 Absorption manipulation of Optical Interference (AMOI) and Energy-Up Photonic Transistor

Specifically, the coupled waveguides based EUPT device is shown in Fig. 4.15(a). It has an unusual geometry in that only one arm of the two coupled waveguides is transparent (passive) while the other arm contains active medium M that is typically absorptive, but is amenable to optical excitation. The coupled waveguides have various input/output ports labeled as PS-IN (power-supply in), SIG-IN/PS-OUT (signal in/power-supply out), and SIG-OUT (signal out). The coupler's length is chosen to be a full coupling length LC for input wavelength λ_H from PS-IN.

Let us first discuss how AMOI works. To illustrate the principle of optical switching via Absorption Manipulation of Optical Interference (AMOI), we simulated the launching of a CW input beam with power $P_{PS\text{-}IN}$ into PS-IN. We then vary the absorption coefficient α of medium M and plot the output powers from PS-OUT and SIG-OUT ($P_{PS\text{-}OUT}$ and $P_{SIG\text{-}OUT}$) as a function of αL_C in Fig. 4.15(b), for the case where the input intensity $I_{PS\text{-}IN}$ is low compared to the saturation intensity I_{SAT} of the medium (intensity $I=P/A_{WG}$, where P is the beam power and A_{WG} is the waveguide mode area). The normalized outputs only depend on the product αL_C and are independent on the individual values of α and L_C. We see that when $\alpha=0$, we have $P_{PS\text{-}OUT}=P_{PS\text{-}IN}$ and $P_{SIG\text{-}OUT}=0$ since input beam entering the lower transparent waveguide will be coupled to the top waveguide completely (Fig. 4.15(c)). When αL_C increases from 0 to 5, $P_{SIG\text{-}OUT}$ increases while $P_{PS\text{-}OUT}$ decreases, and the total output decreases as a result of the absorption. When αL_C increases to 50, $P_{SIG\text{-}OUT}$ reaches 80% of the input power (Fig. 4.15(d)). At this point, the system

actually sees little loss. This is because at high absorption, the small energy leakage to the top waveguide has no chance to build up constructively, resulting in little energy transfer to the top waveguide and hence little absorption. Our applications will operate around αL_C ~5. Typical direct-gap semiconductor can have α~0.5μm^{-1}, resulting in compact device size of L_C ~10 μm.

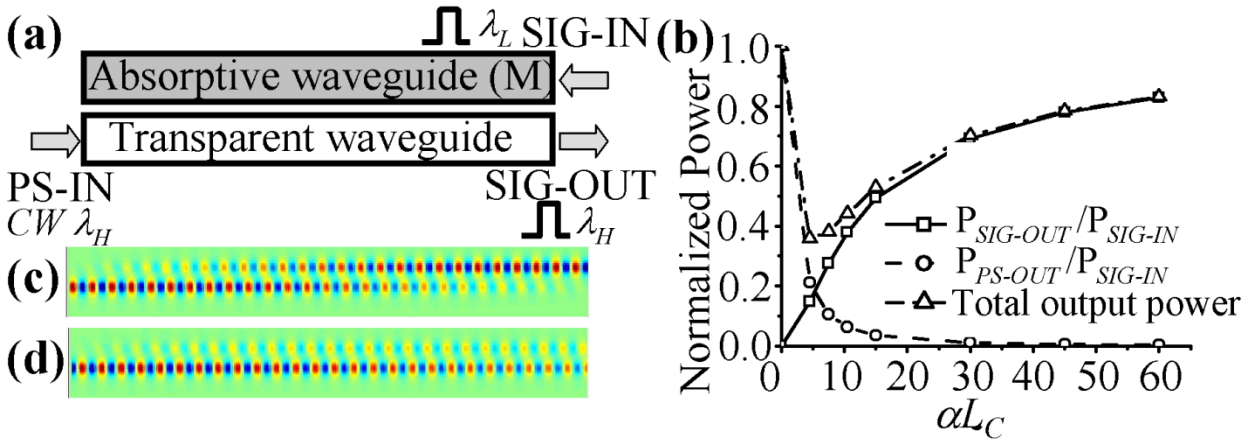

FIG. 4.15 (a) EUPT structure; (b) output from EUPT two ports as a function of αLC; (c) electric field showing output to PS-OUT when top waveguide is transparent; (d) output to SIG-OUT when top waveguide is absorptive.

In all-optical operation, the absorption coefficient of the medium in Fig. 4.15(a) is controlled via a fast control-signal pulse with $P_{SIG\text{-}IN}$ entering the right side of the top waveguide. The medium may be modeled as a multi-level type medium with a bandgap energy E_G for the two lowest levels, and can be provided by a semiconductor [2, 7]. A separate CW beam $P_{PS\text{-}IN}$ at λ_H, with energy $E_H > E_G$, enters PS-IN. This CW beam functions as a "power supply" beam and

is labeled as PS. For the desired operation, we make $P_{PS\text{-}IN}$ to be substantially higher than the medium saturation power P_{SAT} so that it will initially saturate M (i.e. pump M to transparency at λ_H) and be fully coupled to PS-OUT resulting in $P_{PS\text{-}OUT} = P_{PS\text{-}IN}$. Transparency at λ_H means that M is having gain for a lower energy beam. When a short signal pulse $P_{SIG\text{-}IN}$ at λ_L with a lower energy $E_L<E_H$ (still above E_G) enters SIG-IN/PS-OUT, it will see gain and de-excite M via stimulated emission. This causes M to become lossy at λ_H and the $P_{PS\text{-}IN}$ beam will see loss in the upper waveguide. Due to AMOI, the $P_{PS\text{-}IN}$ beam will be partially channeled to exit the lower waveguide at SIG-OUT with a short pulse $P_{SIG\text{-}OUT}$ at λ_H. Thus, a signal pulse at λ_L entering SIG-IN/PS-OUT will produce an output pulse from SIG-OUT with $\lambda_H<\lambda_L$, resulting in energy-up conversion. As shown below, the switched out pulse at SIG-OUT can actually have higher power than the input pulse to SIG-IN, resulting in signal amplification. Note in particular that the power supply beam PS-IN to be switched would not self switched through irrespective of how high its power ($P_{PS\text{-}IN}$) is. As mentioned above, this is important for the achieving switching gain needed for obtaining signal amplification. As discussed below, the medium of this device has no optical gain at the switched-out wavelength (in fact the medium is absorptive). Hence, the signal amplification is simply due to the switching gain (a weak pulse is used to switch a stronger "power-supply" optical beam).

The full device operation requires the transient dynamics of the pulse-medium interactions to be simulated with the pulse's spatial propagation. The simulation is performed using Finite-Difference Time Domain (FDTD) method that numerically solves Maxwell equations in time and space without any additional approximations. The semiconductor medium

is modeled realistically using a semiconductor model that we developed recently for used in the FDTD method [2, 7]. Our model takes into account the main carrier dynamics in semiconductor including intraband carrier relaxation, interband transition, carrier band-filling, Fermi-Dirac thermalization, as well as carrier-induced optical nonlinearities. The simulation assumes the following typical semiconductor parameters: spontaneous decay time τ_{SP} = 1nsec, intraband relaxation time τ' = 100 fsec, dipole transverse relaxation rate $\delta\omega = 3.9\times10^{13}$ Hz, and a ground-state electron population density that gives an on-resonance absorption coefficient of α=0.6 μm^{-1} and I_{SAT}=1kW/cm^2, which are within typical experimental values [38].

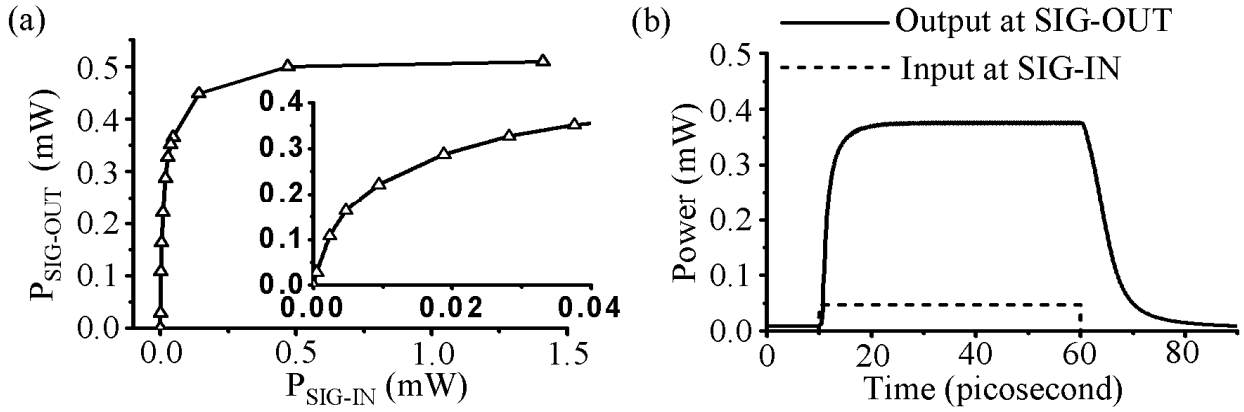

FIG. 4.16 (a) $P_{SIG-OUT}$ at different P_{SIG-IN} with constant P_{PS-IN}; (b) dynamical simulation with a 50psec input pulse.

As an example of the all-optical operation, we assume L_C=15μm. The structure is a single-mode semiconductor waveguide with a high refractive index core of n=3.4 surrounded by n=1.45 cladding materials (e.g. SiO_2) similar to the ones shown in [42]. For the simulation, we

assume TM modes, a waveguide width of 0.25 μm, and a waveguide height of 0.35 μm, which give a calculated mode area A_{WG} of 0.043 μm^2 (for λ_H = 1450 nm) or P_{SAT} = 0.43 μW. We take λ_L = 1550 nm, λ_H = 1450 nm, $P_{PS\text{-}IN}$ = 3,000P_{SAT} = 1.29 mW. At SIG-IN, we send in a 50 psec pulse (20Gb/s) with a varying pulse power $P_{SIG\text{-}IN}$ and plot $P_{SIG\text{-}OUT}$ versus $P_{SIG\text{-}IN}$ (Fig. 4.16(a)) in which we see that the device signal output has a quasi-linear regime with a maximal amplification G_S>10 at $P_{SIG\text{-}IN}$ = 0.014 mW, followed by a transition region, and then a saturation region ($P_{SIG\text{-}IN}$ = 0.15-1.5 mW) in which the output changes by only 10% with the input changes by >10x. The temporal shapes for the SIG-IN and SIG-OUT pulses at the quasi-linear regime are shown in Fig. 4.16(b). Note that these devices work with a much shorter interacting length. As a result, the carrier induced refractive index variations do not cause any appreciable cross-phase or self-phase modulation. Hence, the pulses switched out remained basically undistorted spectrally.

4.2.3 Gain manipulation of Optical Interference (GMOI)

While EUPT outputs pulse at λ_H with input at λ_L, EDPT will be able to convert the pulse back to a wavelength $\lambda_{L'}$ near or at λ_L. The EDPT device is also in the form of two coupled waveguide arms as shown in Fig. 4.17(a). One of the waveguide arms is transparent and the other half transparent and half with gain medium *M'*. For the EDPT, a CW beam $P_{PS\text{-}IN}$ at λ_L and energy E_L above the bandgap energy E_G of the active medium enters PS-IN. When the medium gain is below zero, this beam will initially be fully coupled to PS-OUT, resulting in an output power $P_{PS\text{-}OUT}$ =$P_{PS\text{-}IN}$. When a signal pulse $P_{SIG\text{-}IN}$ at shorter wavelength λ_H enters SIG-IN, it will excite *M'*. This causes the medium *M'* to achieve gain at λ_L and the $P_{PS\text{-}IN}$ beam will see gain in the upper waveguide. Due to the GMOI action discussed below, the $P_{PS\text{-}IN}$ beam will then be

channeled to exit the upper waveguide at SIG-OUT with a short output pulse $P_{SIG\text{-}OUT}$ at λ_L. The result is that a signal pulse at λ_H entering SIG-IN will produce an output pulse at SIG-OUT with a higher energy at λ_L.

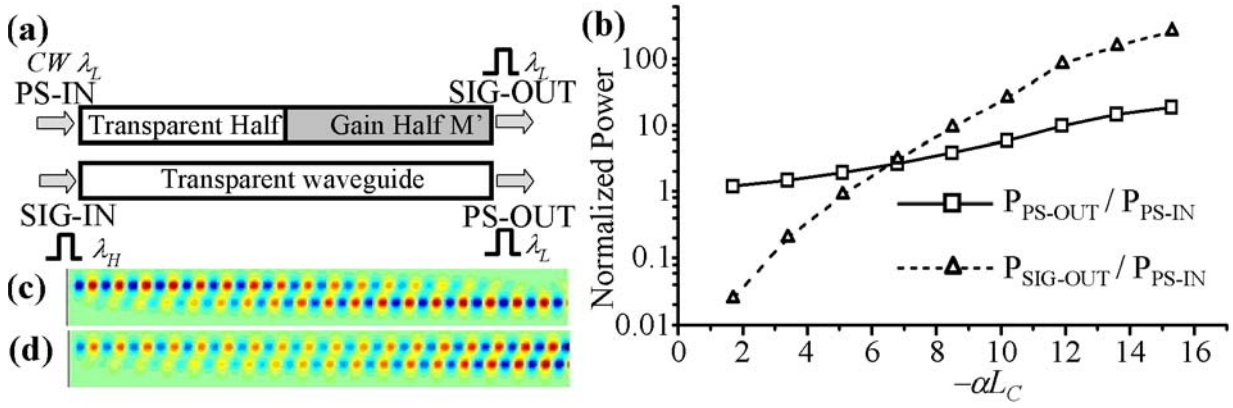

FIG. 4.17 (a) EDPT structure; (b) output from two ports as a function of αL_C; (c) electrical field showing when the gain half is transparent; (d) when the gain half has gain=0.5/μm for the 13μm long coupler.

To illustrate the principle of optical switching via Gain Manipulation of Optical Interference (GMOI), we let the gain coefficient of *M'* to be $-\alpha$ and plot in Fig. 4.17(b) $P_{PS\text{-}OUT}$ and $P_{SIG\text{-}OUT}$ versus $-\alpha L_C$ when $I_{PS\text{-}IN}$ is low compared to I_{SAT}. We see that when $\alpha=0$ so that $-\alpha L_C = 0$, we have $P_{PS\text{-}OUT} = P_{PS\text{-}IN}$ and $P_{SIG\text{-}OUT} = 0$. When $-\alpha L_C$ ($\alpha<0$ indicates gain) increases as the gain goes higher, $P_{SIG\text{-}OUT}$ will increase faster than $P_{PS\text{-}OUT}$. After $-\alpha L_C$ reaches 7, $P_{SIG\text{-}OUT}$ is actually higher than $P_{PS\text{-}OUT}$, which is a good point to operate. Our dynamical simulation with a 50psec input pulse at 1450nm and $P_{SIG\text{-}IN}$=0.43mW is shown in Fig. 4.18(a). The waveguide

and medium parameters are the same as those for EUPT. From Figs. 4.16(b) and 4.18(a), one sees that both the EUPT and EDPT can operate at a speed of ~100GHz (10psec). Fig. 4.18(b) plots the output power versus input pulse power at power-supply $P_{PS\text{-}IN}$=14μW. We also see that while EDPT has no signal amplification, high-efficiency conversion (>75%) can be achieved. Note again that the power supply beam would not self switched irrespective of how high its power is.

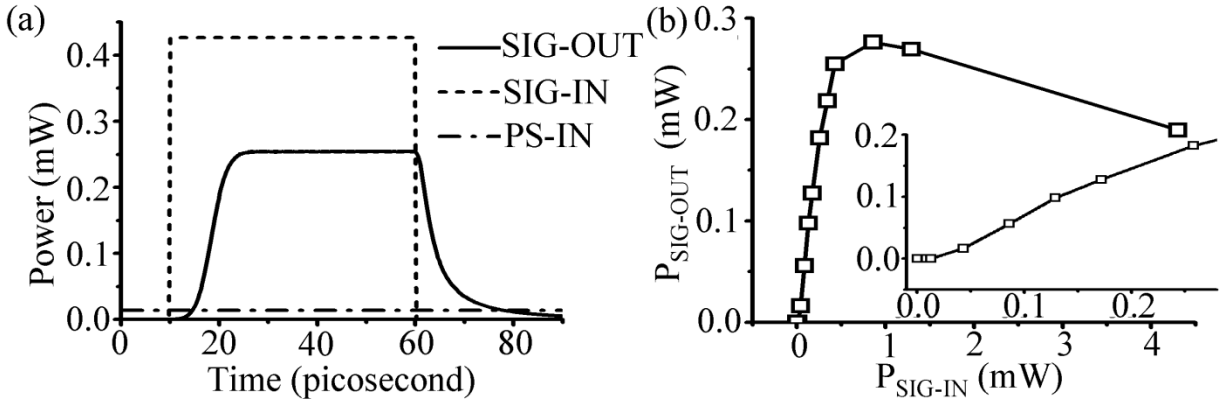

Fig. 4.18 Dynamical FDTD simulation for the EDPT: (a) Input/output relations for down converters; (b) Output power at different input pulse power.

The EUPT and EDPT can be joined in tandem as shown in Fig. 4.19(a) to achieve a full photonic transistor (FPT) capable of wide wavelength conversion range, signal amplification, and pulse regeneration with the cascaded input/output relation shown in Fig. 4.19(b). The device can operate within the wavelength range from λ_L and λ_H. The EUPT as well as the FPT device behaves similar to an electronic transistor in that it has both a linear and a saturation amplification regime in the response curve. The “power supplies” of EUPT, EDPT, and FPT are CW optical beams, switched to the output via input signals by means of optical absorption or

gain. In input-output block diagram form, the Photonic Transistors are like the Electronic Transistors but with "power-supply currents" replaced by "CW optical beams". The use of two CW optical beams at different wavelengths provides wavelength conversion and is unique to the optical case. There is no electrical power needed for the Photon Transistors to function. The power-supplies to a photonic transistor circuit are just CW optical beams. Like transistors, logic gates can be formed via cascading EDPTs and EUPTs to realize various all-optical signal-processing functions. In such applications, some of the CW beams will be replaced by other input pulse streams.

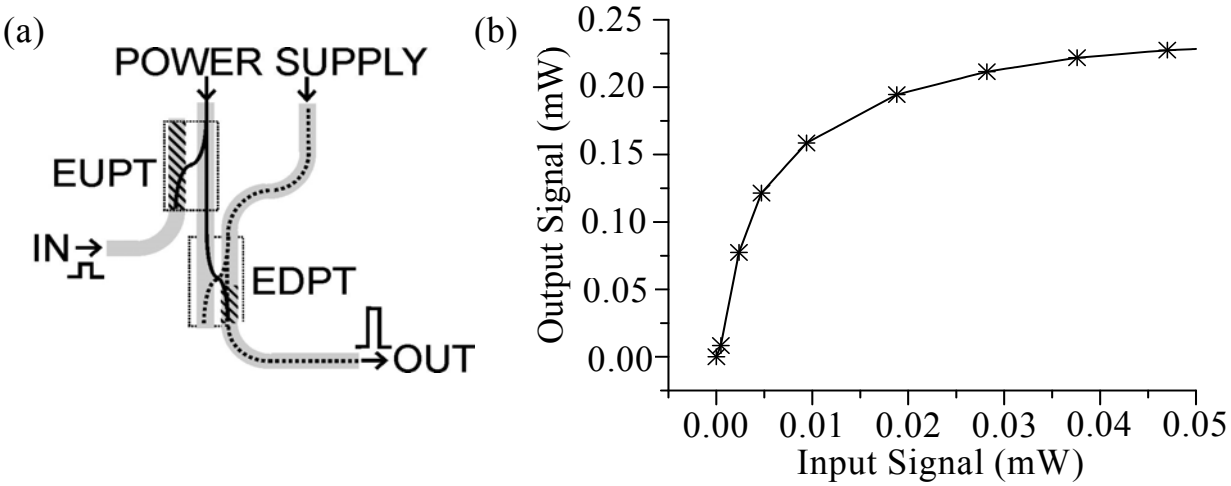

Fig. 4.19 (a) Layout of a full-function photon transistor; (b) input –output relation.

4.2.4 A Discussion on All-Optical Photonic Transistor Figure of Merit

Desirable Properties of All-Optical Device: As the goal of this work is to realize a new enabling technology for all-optical device, it would be important to understand the desirable properties for an ideal all-optical device. To do so, we listed the essential properties of current

electronic transistors. The properties of a typical transistor in a current 3GHz microprocessor chip are listed in Table 4.1. In order for all-optical switching device (or photonic transistor (PT)) to bring advantages beyond electronics, they shall have the competitive properties listed below:

	Operating frequency	Switching energy	Physical area	Power gain	Pulse regenerating	Wide optical bandwidth
Current Electronic transistor	~5GHz	A few fJ (10^7 units at 3Gb/s consume ~100W)	~10 μm^2 (10^7 ET ~1cm^2)	Yes	Yes	No
AOD desirable properties	>10Gb/s (can scale up to 1Tb/s)	<10 fJ (10^6 AOD at 10Gb/s ~100W)	<100 μm^2 (10^6 AOD ~1cm^2)	Yes	Yes	Yes wavelength conversion possible

Table 4.1 Desirable Properties of All-Optical Devices (AOD)

These properties may be summarized more succinctly by defining a Merit Factor (MF) for all-optical device (or photonic transistor (PT)) as follows:

$$MF_{PT} = \frac{\mathrm{N_{ch}} \cdot G}{(P_{PS} + P_{CTR-SIG})T \cdot A}, \tag{4.13}$$

where we have assumed that the photonic transistor requires a power-supply power P_{PS}, has a device area A, and is operating with digital signal pulses having input (control) signal power $P_{CTR\text{-}SIG}$, pulse repetition time T (or data rate $R=1/T$), and gain G *(G<1 is loss)*. The photonic transistors also has optical bandwidth dν corresponding to N_{ch} optical channels (N_{ch} =dν/(3R), 3R provides a safe 3 times inter-channel frequency spacing). N_{ch} >1 means the device can process different frequency channels in sequence. For the typical electronic transistor

mentioned above, we have $(P_{PS}+P_{CTR\text{-}SIG})T$~10fJ, G~2, A~10μm^2, and N_{ch}=1. The relative figure of merits normalized to the electronic transistor (ET) will be defined as $F=MF_{PT} / MF_{ET.}$ An ideal photonic transistor device shall have F value approaching or exceeding 1.

Table 4.2 lists the relative figure of merit for typical SOA bases optical switching devices and $\chi^{(3)}$ (semiconductor at below half the bandgap) based optical switching devices. The figure of merits or both device categories are several orders of magnitude worse than current electronic transistors.

All-optical switching devices involving semiconductor amplifiers (SOAs) in cross phase or cross gain modulation mode have attracted great interest for their integration potential and low optical power requirement. These devices rely on carrier-density-induced refractive index change via cross phase modulation (XPM) or gain change via cross gain modulation (XGM) [55-61]. The XPM scheme involves SOAs on two arms of a Mach-Zehnder Interferometer (MZI). By adjusting the SOA bias current injection and optical input beams, different response functions from input signals are achieved. The main disadvantage of this approach is their large electrical power consumption (~500mW wall-plugged power per switch) and the resulted heating when integration density is high. Meanwhile, when more than one SOA is used in interferometer structure, careful biasing is needed, which further increases the device complexity. In addition, they typically have high spontaneous emission noise and MZI also leads to large device size (millimeters).

Besides the problems mentioned above, the speed of SOA based all-optical switching deices could barely reach 100Gbit/s because of the slow recovering time of the large resonant

nonlinearity typically in ns range [60]. In the literature, there are three main ways proposed to overcome the slow nonlinearity. The first approach is to use a CW holding beam [61] to bring the carrier back to initial state. The second way is to design switch configuration so that slow nonlinearity in two arms of the interferometer will cancel each other [62-64]; this approach cannot solve the problem completely because that at the end of the switching window, the SOA will not be at the initial state, so repetition rate is still limited by the carrier lifetime although the switching window can be extremely short. The third way is to use a fast recovery (ps) nonlinear refractive index in SOA biased at transparency current to construct all-optical switches [65], but the required optical power is typically substantially higher.

$\chi^{(3)}$ based All-Optical Devices

Another category of photonic switching devices are based on $\chi^{(3)}$ material nonlinearity that gives very fast nonlinear refractive index change with response time less than 100 femtoseconds. The problem is that currently there is no material feasible for integration that has high enough $\chi^{(3)}$ values without high nonlinear loss [66]. As a result, high optical intensity of $\sim 10^8 W/cm^2$ or long device length (~km) is needed to perform the switching.

Other all-optical switching operation has been demonstrated using passive semiconductor waveguides with Symmetric MZ design [67-70]. The drawback of this approach is that they normally include un-integratable optical element such as polarization sensitive isolators, polarization controllers and complex feedback control electronics. In addition to that, the repetition rate is still limited by the carrier lifetime although the switching window can be extremely short.

Applying the FOM so defined to a typical electronic transistor in a microprocessor [71], we have $P_{TOT}\,T \sim 5$ fJ, $G_S \sim 2$, $N_{ch} = 1$, $A = 0.5\ \mu m^2$, giving for the electronic transistor an equivalent $MF_{ET} = (1*2)/(5*10^{-15}*0.5*10^{-12})$ ($J^{-1}\ m^{-2}$). A Relative Figure of Merits normalized to the typical Electronic Transistor (ET) can then be given by dividing MF_{PT} by MF_{ET}. It will be referred to as the Photonic Transistor Relative Figure of Merits: $F_{PT} = MF_{PT} / MF_{ET.}$ The desired PT device shall have F_{PT} value approaching or exceeding 1. As tabulated in Table 4.2, the typical $\chi^{(3)}$ and SOA $n^{(2)}$ based devices have low F_{PT}'s with $F_{PT} \sim 10^{-5}$ and $F_{PT} \sim 10^{-6}$, respectively, based on parameters in [44-48]. Whereas the PTs described here can achieve a F_{PT} near unity or over 100,000x higher than the typical $\chi^{(3)}$ or $n^{(2)}$ based devices.

In summary, the main problem currently impeding the realization of practical Photonic Transistor (PT) is that the physical scheme involved typically required either high optical power or long interaction length, resulting in Transistor Figure of Merits (F_{PT}) that is >100,000x worse than that of Electronic Transistors. In this dissertation, we illustrated a new physical mechanism to realize Photonic Transistor (PT) action involving the use of optically-controlled gain and absorption to manipulate optical interference (GAMOI), resulting in highly-efficient all-optical operations that can be used to form PTs with a wide variety of functionalities (switching, amplification, logical operation, λ conversion, pulse regeneration). The illustrated use of coupled waveguides is not the only choice as other multimode optical interference devices can also be used. Simulation of exemplary devices based on typical semiconductor medium show that the PTs are capable of high speed (>100Gb/s), low signal operating power (hundreds of μW), low power consumption (a few mW), compact size of ten of micrometers, good signal amplification,

and broad optical bandwidth, resulting in a Figure of Merits F_{PT} close to that of Electronic Transistors and $>10^5$ times higher than $\chi^{(3)}$ or $n^{(2)}$ approaches. The operating speed and gain can be pushed higher than what we illustrated here by using higher power for the power-supply beams. The operating power and speed performances are also dependant on the medium properties such as saturation power, which may be further engineered using quantum-confined structures. Thus, the new device concept described and simulated here will enable various new possibilities for realizing multi-functional Photonic Transistors that are orders of magnitudes more efficient than current approaches, and are highly attractive.

	$\chi^{(3)}$ half gap	SOA	GAMOI
P_{PS} (at 100Gb/s)	0	~ 400mW	~2mW
$P_{CTR\text{-}SIG}$ (at 100Gb/s)	~ 1 W	~ 0.01W	10μW
Amplification (G_S)	~ 0.1	~ 0.1	10
Device Area A (μm^2)	~ 1,000	~ 10,000	60
Max. Data Rate ($1/T$)	~ 5 Tb/s	~ 100 Gb/s	~ 100 Gb/s
N_{ch}	~ 1	~20	~20
F	~ $4x10^{-6}$	~ $4x10^{-7}$	~1

TABLE 4.2 Relative figure of merit for various photonic switching devices: (1) $\chi^{(3)}$ of semiconductor [44, 45]; (2) SOA based [46-48]; (3) GAMOI.

4.3 Simulation of GAMOI based Photonic transistor Using 4-level FDTD Model

In section 4.2, we give a simplified description on the basic operation principle of energy up photonic transistor (EUPT) and energy down photonic transistor (EDPT). The characteristics of the photonic transistor devices can be investigated using three different level of simplification.

The most simplified simulation results can be obtained by the analytical solution as shown in section 4.2. The analytical solution explains the basic mechanism governing the operation of the photonic transistors. However, the results are obtained with the following assumptions: first, it is assumed that the gain or absorption coefficient in the non-transparent part of the coupler remain constant; second, it is assumed that the real part of the refractive index is not related to the gain or absorption coefficients, so the optical mode profile in the two waveguides of the coupler remain unchanged throughout the full coupling length.

In order to describe the operation of the device under all-optical pulse situation, where the optical pulse entering the device will be change the gain and absorption coefficient to different values in different region, we use the 4-level FDTD model to study the device transient behavior. The 4-level FDTD model includes two active dipole pairs with resonant wavelength at the two optical wavelengths during operation. As a result both the signal and pump wavelength are considered on resonant with the medium and the change in the gain or absorption coefficient will not change the real part of the refractive index. This is a great simplification from the real semiconductor case. However, this model allows us to look at the effect of the imaginary part of

the refractive index alone and obtai n valuable information as regard to the dynamical operation of the device.

To take fully account of the effect from changes in both the real and the imaginary part of the refractive index, the multi-level FDTD model is required so the optically-induces real part of the refractive index change can also be included. The change in the real part of the refractive index, although plays a minor role in changing the coupling characteristics, can be shown to be not totally insignificant and is necessary to be included in the model in order to describe the device operation more accurately. Another important concern rising from the change in the real part of the refractive index is that in order to maintain the desired extinction ratio, the geometrical dimensions of the two waveguides in the coupler structure might need to be different in order to compensate back the refractive index difference rising from the all-optical pulse.

In this section we will cover details on the simulation of GAMOI based photonic transistors using the 4-level FDTD model.

4.3.1 Parameters for the active medium in the 4-level FDTD model

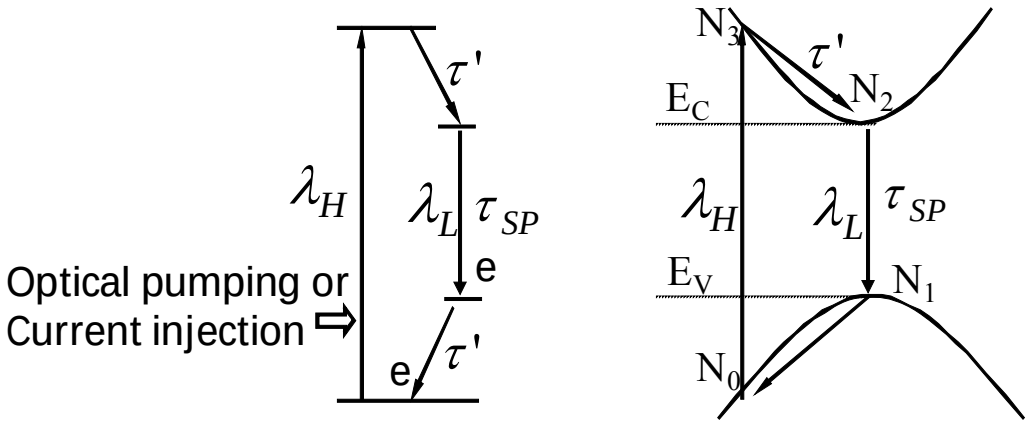

Fig. 4.20 4-level FDTD model

First, in order to determine the proper carrier density to be used in our four-level two-electron model, we simulated the absorption behavior of semiconductor. According to [38], for unstrained $In_{0.53}Ga_{0.47}As/(Q1.08)60\,\mathring{A}$ quantum well structure, the sheet carrier density is about $1.0\times10^{12}\,cm^{-2}$ at the transparent point, which corresponding to a carrier density of $1.67\times10^{24}\,m^{-3}$. The total carrier density at ground state will be twice the value at the transparent point, so the total carrier density can be calculated as $3.3\times10^{24}\,m^{-3}$. The absorption linewidth at ground state is about 300nm. Under normal pumping condition, the gain linewidth is about 100nm. Then the carrier density 'seen' within the gain linewidth will be about one third of the total carrier density in unexcited case. As a result, the proper carrier density under normal pumping conditions will be $1.1\times10^{24}\,m^{-3}$. We also need to take into account of the fact that in our absorption simulation, only one-dimensional CW wave is launched into the semiconductor medium, but in real situation, carrier density will spread over all three spatial dimensions. This fact requires us to use a carrier density of $0.35\times10^{24}\,m^{-3}$. We Assume $\tau_{21}=3ns,\quad \tau_{30}=4.16ns,\quad \tau_{32}=\tau_{10}=100\,fs$. The dipole dephasing time for level |3>-|0> and |2>-|1> are both 100fs. The absorption linewidth is chosen to be the normal gain linewidth of 100nm. At time zero, all electrons are at ground states, that is, $N_1=N_0=1, N_2=N_3=0$.

The structure we studied is a weakly guided semiconductor waveguide with core reflective index equal to 3 and cladding reflective index equal to 2.88. The waveguide is $1\mu m$ in length with a core region width of $1\mu m$. We assume that only the core region has active medium. We then launch a CW wave at the resonant wavelength between level |2> and level |1> of

$1.55\mu m$. The carrier density is chosen to be $0.35\times10^{24}\,m^{-3}$.

The absorption coefficient is measured by comparing the time average of the Poynting vector over $1\mu m$ distance. The resulted absorption coefficient is $1\mu m^{-1}$, which agrees with the typical absorption coefficient value for semiconductors.

4.3.2 EUPT Simulation

In section 4.2, we described briefly the basic working principle of the EUPT. Here we will examine in more detail the effect of various papameters on the device behavior. Here we will vary the pumping power and examine the response of the EUPT device. The structure used is: waveguide index 2.7 and 1.45 (vertical mode size 0.2μm), λ_H=1.45μm, λ_L=1.55μm, coupler length of 15μm with 0.5/μm ground state absorption. The result is shown in Fig. 4.21.

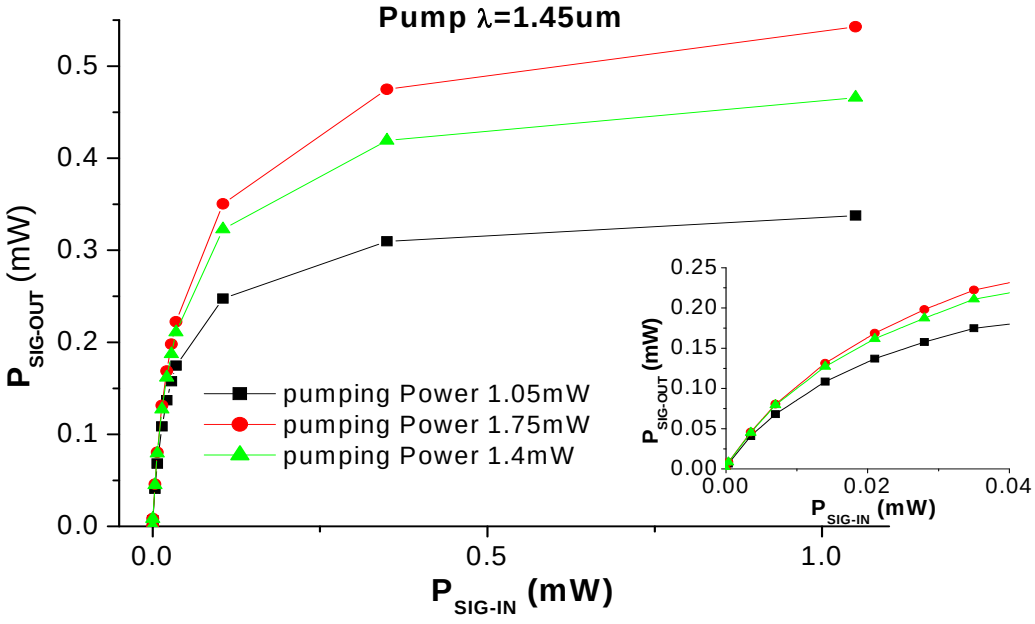

Fig. 4.21 EUPT input-output relations at different pumping power

It can be seen that the device signal output has a quasi-linear regime with a maximal amplification G_S>10 at P_{SIG-IN} = 0.014 mW, followed by a transition region, and then a saturation region (P_{SIG-IN} = 0.15-1.5 mW) in which the output changes by only 10% with the input changes by >10x.

Next we keep same pumping power and change the absorption coefficient α. At constant pumping power of 1.05mW, the gain varies a lot at different α*L as shown in Fig. 4.22. The maximal signal output power increase as the α*L increases. We can see that although the increase in the α*L can increase the signal gain, higher α*L makes it necessary to use higher pumping power to achieve the same switching speed. In the case where the pumping power is kept constant, the switching speed becomes slower as the α*L increases.

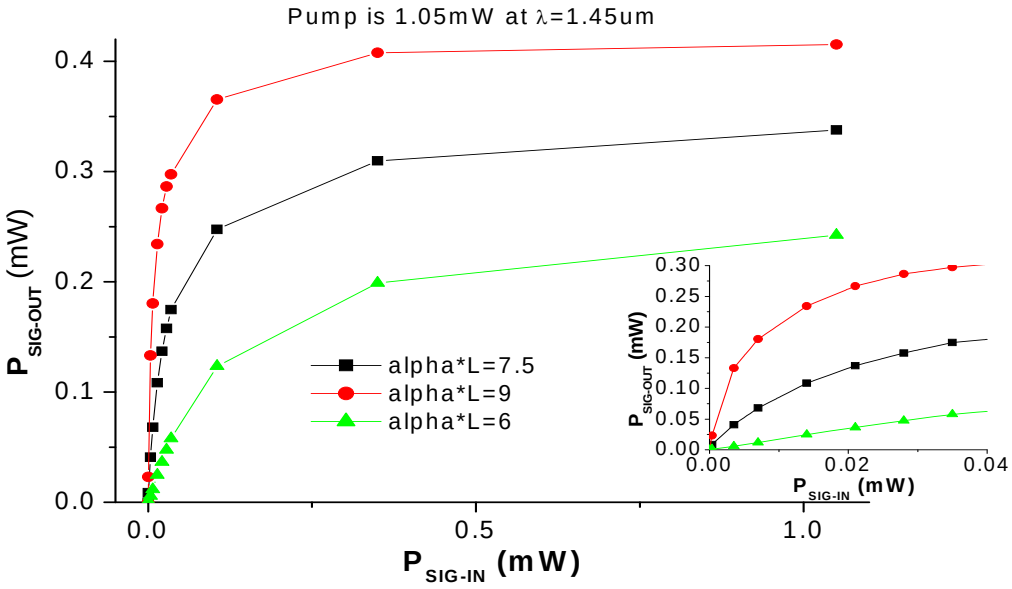

Fig. 4.22 EUPT input-output relations at different αL

We then study the EUPT behavior change at different signal wavelength. The result is shown in Fig. 4.23. This simulation is also for constant pumping power of 1.05mW. We change the wavelength of the input signal by +/- 10nm. The medium resonance frequency is kept unchanged. The gain at saturation region has little change but the gain at linear region changes by 40%. The change is about the same for both +10nm and –10nm wavelength difference.

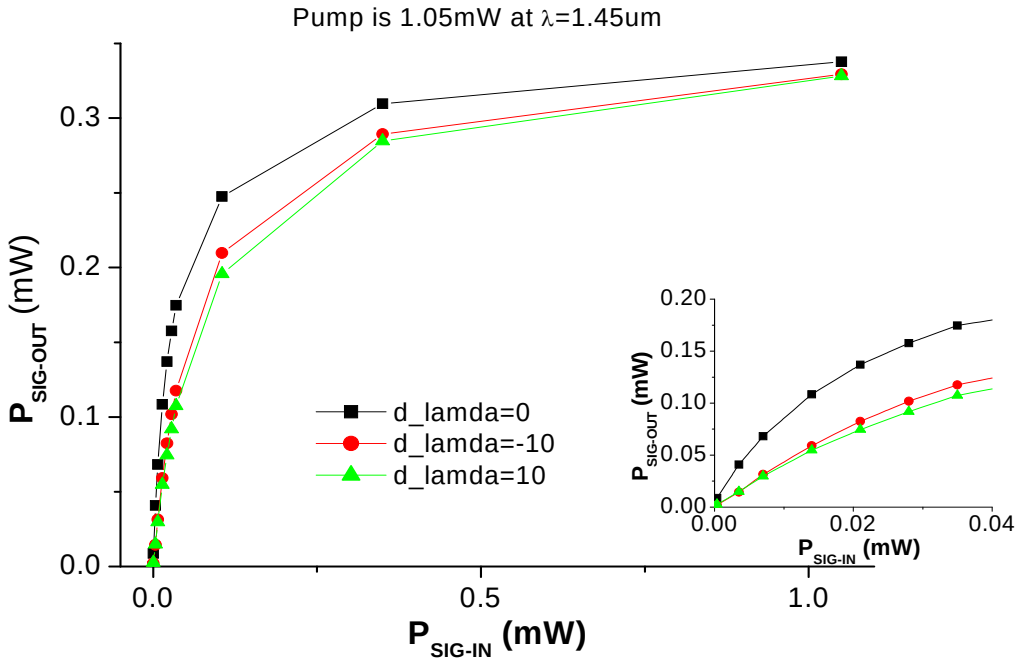

Fig. 4.23 How the EUPT behavior change at different signal wavelength

For the EUPT, the pumping light can either be at 0^{th} order optical mode or 1^{st} order optical mode. If 1^{st} order mode is used, the signal light (0^{th} order mode) will have much longer coupling length and more of the energy from signal light will stay in absorptive waveguide, leading to better switching efficiency. We show below the gain for those two cases with the same

coupler structure. It is obvious that 1st order pumping has much higher gain but the device structure will also be more complicated.

Input_λ_H (mW)	Input_λ_L (mW)	Output (mW)	Gain
0.978	0.326	0.226	0.69
0.978	0.0326	0.09	2.76
0.978	0.00978	0.04	4.08
9.78	0.326	0.28	0.85

Table 4.3 Signal gain when λ_H and λ_L are both 0th order mode, waveguide width is 0.25μm

Input_λ_H (mW)	Input_λ_L (mW)	Output (mW)	Gain
1.3(case1)	0.043	0.205	4.767
1.3	0.013	0.142	10.92
4.3(case2)	0.13	0.49	3.76

Table 4.4 Signal gain when λ_H is 1st order mode, λ_L is 0th order mode, waveguide width is 0.5μm.

For case 1 and 2 in the above table, we simulated two consecutive pulses passing through the EUPT. The result is shown in Fig. 4.24. It can be seen that the device speed can reach >3ps in case 2 and ~10ps in case 1.

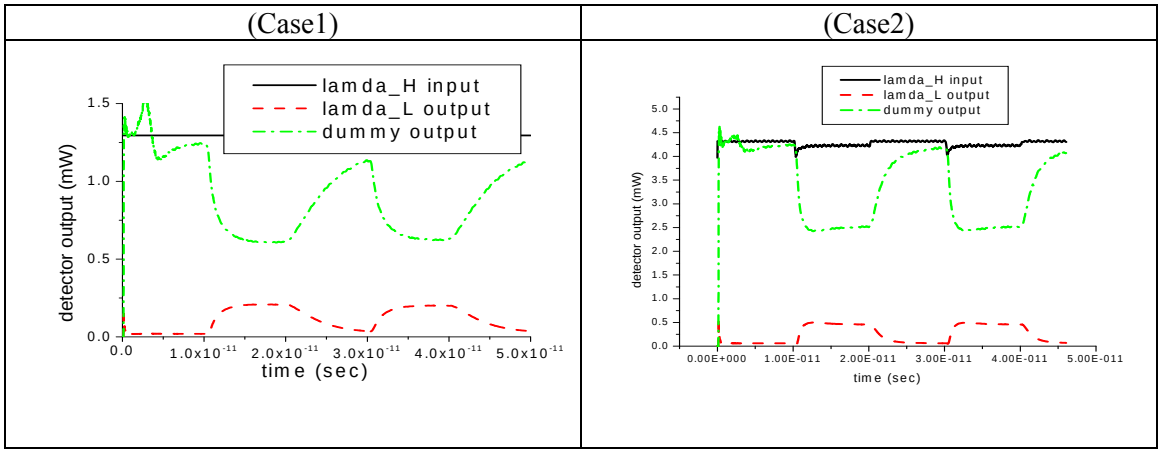

Fig. 4.24 Two consecutive pulses in EUPT operation

4.3.3 EDPT Simulation

For the energy down converter case, we simulated the following situations: the coupler is 13μm in length, with 0.5/μm absorption medium and waveguide width of 0.25μm. Transition quantum efficiency in down conversion case is compared to 1-1 photon transition since part of the energy loss in unavoidable because of the photon energy difference. The result is shown in Fig. 4.25, where the best quantum efficiency achieved is 77.5%. The gain as a function of input CW power at pumping pulse power of 5mW is plotted in Fig. 4.25.

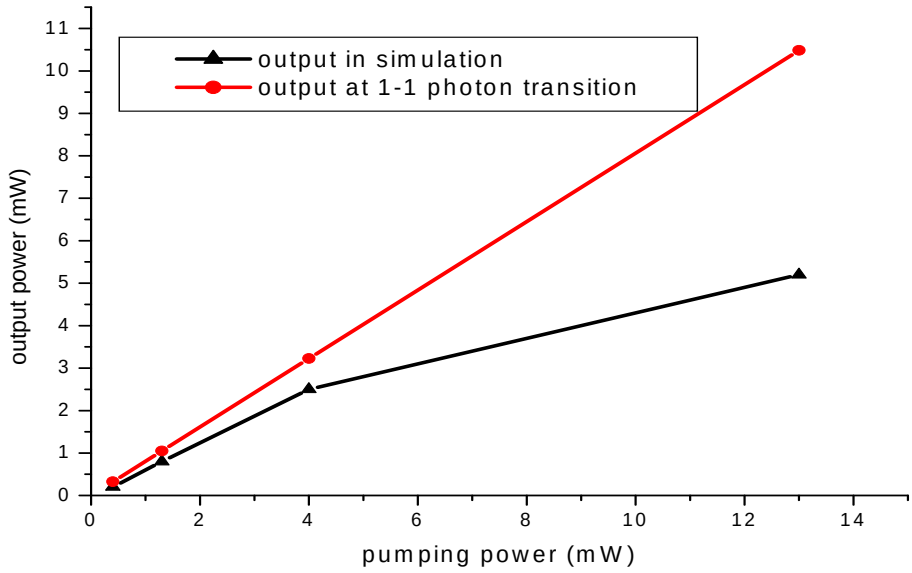

.

Fig. 4.25 EDPT energy transition efficiency for CW power of 0.4mW at different pumping power

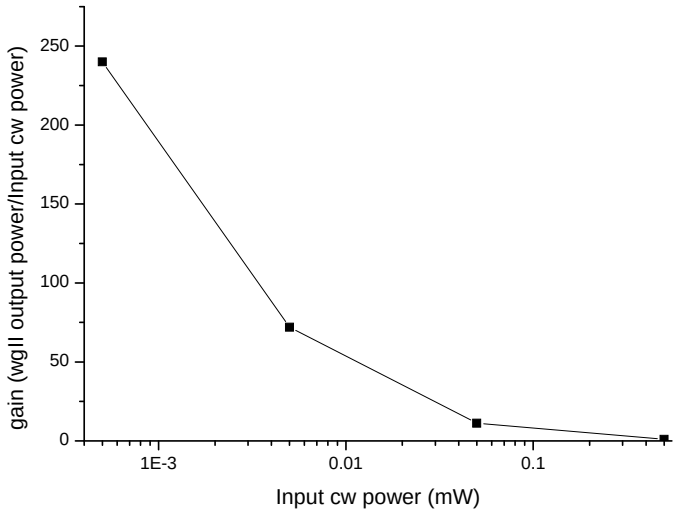

Fig. 4.26 EDPT energy transition efficiency for CW power of 0.4mW at different pumping power

4.3.4 EDPT and EUPT based All-Optical Logic Gate Simulation

The switching ability of the EUPT and EDPT offers basic building blocks for constructing complete set of logic functions. The EUPT and EDPT also double as wavelength converters, which can be useful for logic circuits involving multiple wavelengths. The EUPT also serves the function of pulse reshaping when operated at the saturation region. All those functionalities are of importance when it comes to realizing all-optical digital computing chip. In this section we will discuss the principle and initial simulation results for some typical logic functions.

AND: Using the proposed EUPT and EDPT, there are quite a few different ways to construct an AND gate. Here we gives an example of using one EUPT and one EDPT to

construct an AND gate, which operates at very low power of 60μW for 10Gb/sec speed, and has a signal gain of 3dB.

The layout of the AND gate is shown in Fig. 4.27. "**A**" and "**B**" are the two input port for the incoming data. Signal pulse train "**A**" and "**B**" are both at wavelength 1550nm and with low power of ~60μW (6fJ/pulse for 10Gb/sec). A CW light at wavelength 1490nm serves as the power supply for the logic gates. In our simulation we assume its power is 1mW. When the signal "**A**" is "1", the EUPT will generate an amplified pulse at λ_H in the lower arm of the coupler with power of ~260μW (6dB gain). The pulse will then be transported to the EDPT and pump up the absorber. If the signal "B" is also "1", it will get amplified and exiting from the upper arm of the EDPT coupler. If the signal "B" is "0", the remaining pulse at λ_H will be cleaned up by the absorbing filter following the EDPT.

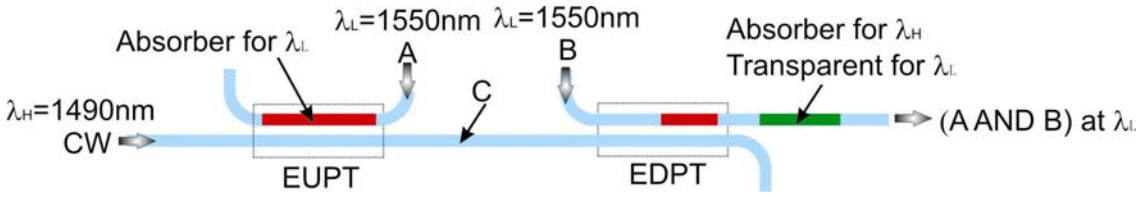

Fig. 4.27 GAMOI based all optical AND gate

From our dynamic FDTD simulation of the full structure (Fig. 4.28), it is shown that for "A" and "B" both with power of 60μW, the output of the AND gate is ~120uW, which means a gain of ~3dB. The gain capability of the proposed all-optical logic gate comes from the novel GAMOI device physics. Signal gain offers the cascadability of the device, which is crucial for the realization of large all-optical logic circuit.

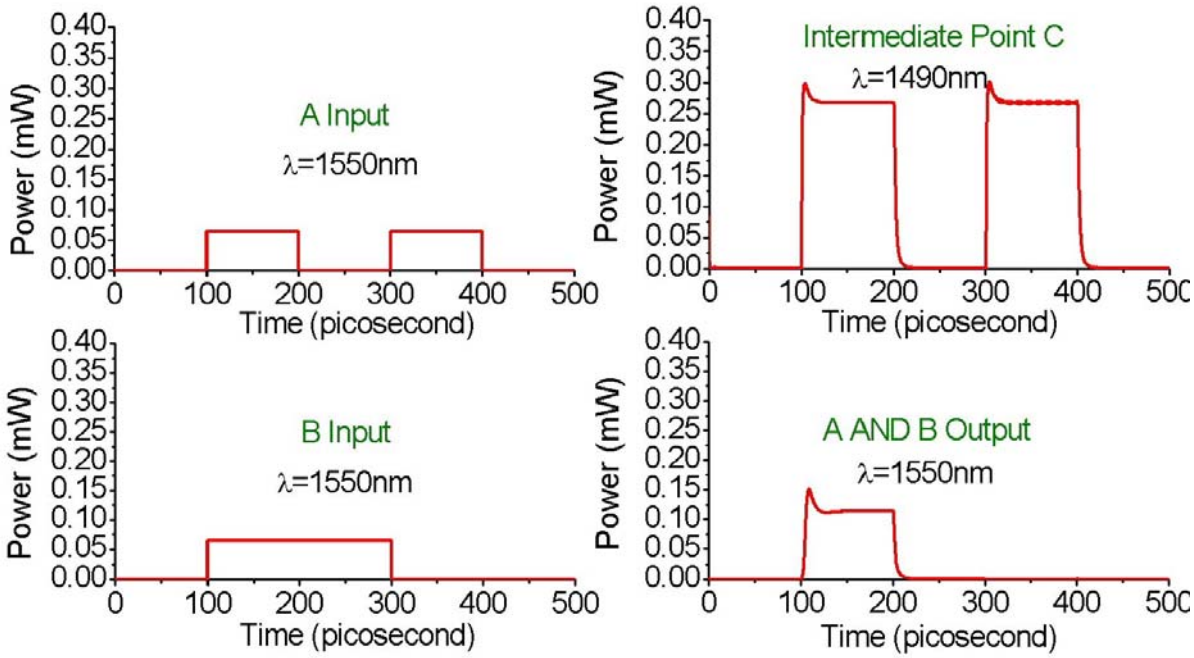

Fig. 4.28 FDTD simulation result of AND gate

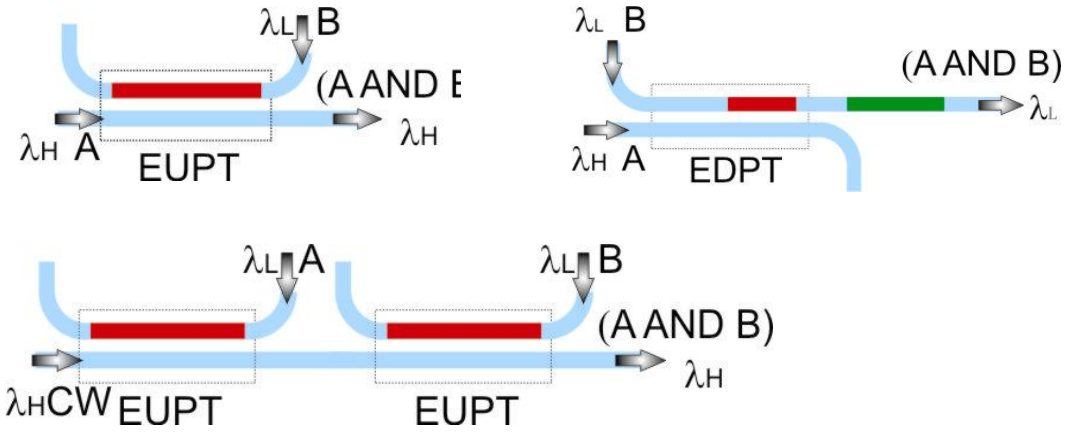

Fig. 4.29 Other configuration of AND gate

Simplified versions of AND gate also exist in cases where gain is not required. Fig. 4.29 shows the examples of other AND gate configuration.

OR: The OR gate can be constructed from either EDPT or EUPT with MZI configuration, as shown in Fig. 4.30. For both cases, when either "A" or "B" is "1", one arm of the MZI will be nonzero so the output will be "1". Only when both "A" and "B" are zero, the output will be zero. Note that in those configurations, the input signal and output signal are at different wavelengths. Depending on applications, if the same wavelength output is required, we can easily convert the output to original wavelength by adding an extra EDPT or EUPT, which can also function as wavelength converters.

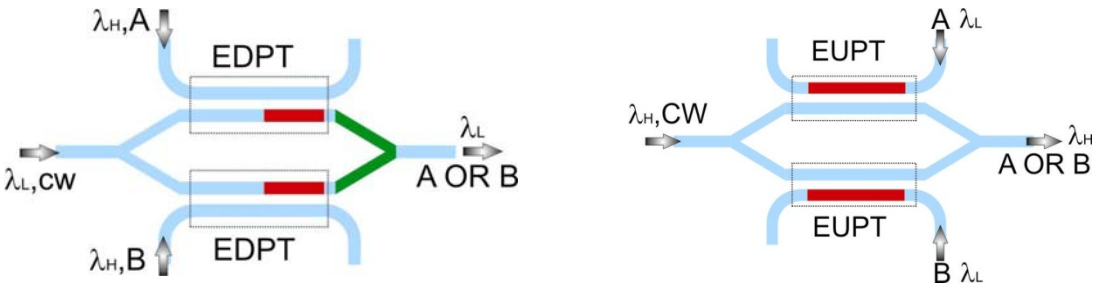

(a) OR gate with two EDPT (b) OR gate with two EUPT

Fig. 4.30 GAMOI based all optical OR gate

XOR: The above OR gate can be easily modified to perform XOR function when one arm of the MZI has an additional π phase shift. In that case, when both "A" and "B" are "1", the two arms of the MZI will have a π phase different and interfere destructively at the end, so the output will be "0".

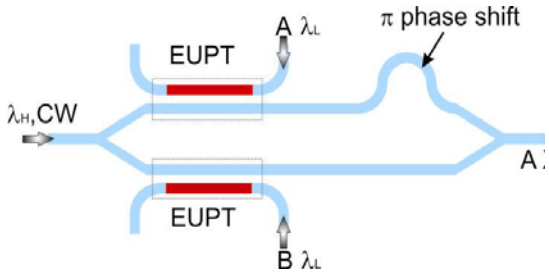

(a) Layout of the XOR gate

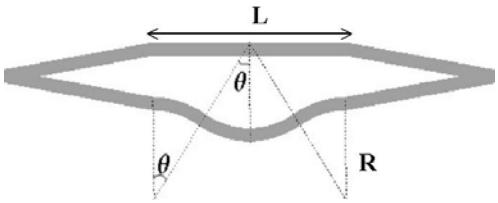

(b) π phase shifted MZI

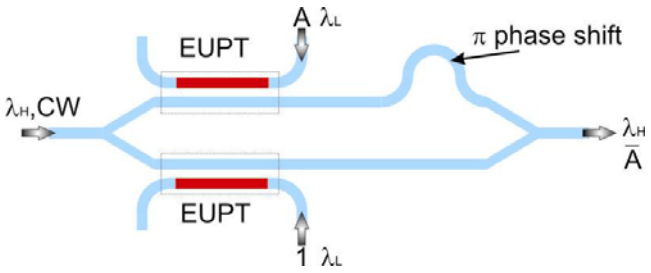

(c) Layout of the NOT gate

Fig. 4.31 GAMOI based all optical XOR/NOT gate

The design principle of π phase shifted MZI is shown in Fig. 4.31 (b). The bending part of one arm in the MZI is designed carefully to give π phase shift for the operating wavelength. In this structure, the phase shift can be expressed as: $\Delta\phi = (4\theta \cdot R - 4R\sin\theta)k_{prop}$. Here k_{prop} is the propagation constant of the optical beam inside the waveguide.

NOT: If one of the inputs in the above XOR gate is set to be "1" all the time, the above XOR gate can be transformed to a NOT gate. (Fig. 4.31(c))

REGENERATOR: The proposed energy-up photonic transistor can also be used as a pulse regenerator when operating at saturation region**.** When the input fluctuates 3dB, the output fluctuation is as small as 0.8dB. At the same time, since the output is at new wavelength and the

output power comes directly from the CW laser source, the noise of the input will not be transferred to the output.

From the discussions above, we can see that the proposed GAMOI based all-optical logic gates are Boolean complete and very flexible in device structure. They also have a lot of unique properties such as very low signal power requirement (10-100uW), fast operation speed (>100Gb/s) and signal gain.

4.4 Simulation of GAMOI based Photonic transistor Using 10-level FDTD Model

We showed above the simulation of the GAMOI based photonic transistors using the 4-level FDTD model. The simulation results give us lots of useful information on the general behaviors of the EUPT and EDPT. But the 4-level model did not take into account the band structure of typical semiconductors; as a result, the carrier-induced refractive index is not included in the model. In addition, the lacking of band filling in that model makes the saturation intensity calculated smaller than typical numbers in semiconductors. To more accurately understand the EUPT and EDPT, we carried out additional simulations on the photonic transistors based on the more sophisticated 10-level semiconductor model. In this part we will describe some of the main results.

4.4.1 Parameters for the active medium in the 10-level FDTD model

We assume a semiconductor bulk medium with bandgap wavelength of 1550nm and model it with the simple parabolic band case. The effective masses for the conduction and valence bands are assumed to be $0.046m_e$ and $0.36m_e$, respectively, with m_e being the free electron mass. The energy levels E_i's are spaced by constant wavelength spacing $\Delta\lambda$. If we use 5 energy levels for conduction and valence band and let $\Delta\lambda$=50nm, then the optical transition wavelengths for the discrete levels will be 1525nm, 1475nm, 1425nm, 1375nm, and 1325nm. The interband decay rate τ_i for typical direct-gap semiconductor bulk medium and quantum well of interest ranges from hundreds of picoseconds to nanoseconds [38]. In the simulation below we use τ_i=1nsec.

For illustration purpose, we set the downward intraband transition time $\tau_{(i,i\text{-}1)C}$ for conduction band electrons to be about one picosecond and set the downward intraband transition time $\tau_{(i\text{-}1,\,i)V}$ for valence band electrons to be about 100fs, which are within the range of values given in the literature [38]. The upward intraband transitions for conduction and valence bands are then set to follow the ratio given in Eq. (3.26). The initial random distribution of carriers will relax to the quasi-steady-state Fermi-Dirac distribution within the time scale given by the intraband transition rates. The dipole dephasing time is set to be ~50fsec. As those medium time-constants are several orders of magnitude larger than the optical period, it will not affect the choice of the FDTD time step (typically 1-2 orders of magnitude smaller than the optical period).

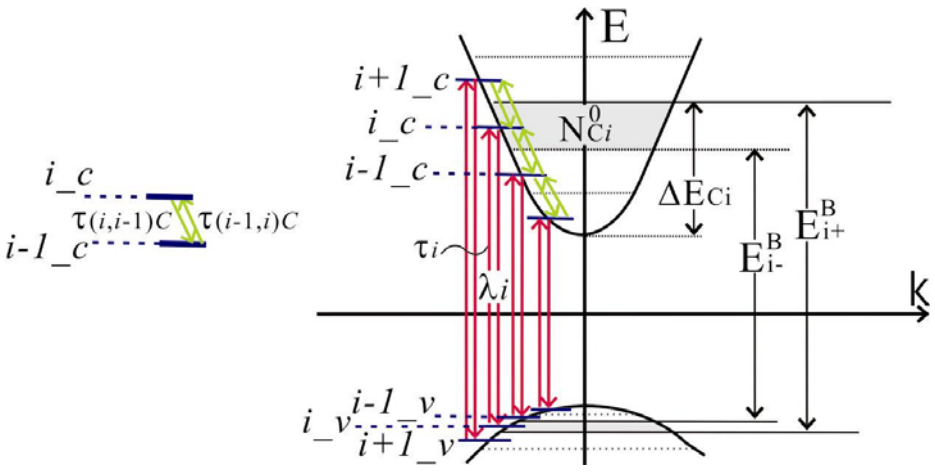

Fig. 4.32 The multi-energy-level model for the FDTD simulation of semiconductor material

4.4.2 EUPT and EDPT Simulation Using 10-level Model

Structure we used is coupler with waveguide vertical mode size of 0.2μm. First we compared the effect of pumping using different wavelength above the bandgap. The comparison was done by using pumping wavelength of 1350 and 1450nm. The pumping light beam was launched in by 1st order optical mode to enhance the gain. The directional coupler in this case is 150μm long with absorption coefficient of 0.05/μm for ground state material. The pumping power is kept at 10mW for both cases. The result is shown in Fig. 4.33. It can be seen that for the same pumping power and signal power, using shorter wavelength pumping beam could result in higher gain.

In practice, however, sometimes we are restricted by the wavelength we can use as the pumping wavelength without incur large loss. For example, if quantum well intermixing is used to fabricate the device, the maximal wavelength shift achievable without excessive loss is usually

~130nm for original wavelength of 1550nm. In this case the pumping wavelength can only be about 100nm away from the bandgap wavelength. Taking the pumping wavelength of 1450nm as example, we can see that because of the band-filling effect, a αL value of ~7 is no longer satisfactory as switching gain is different to achieve.

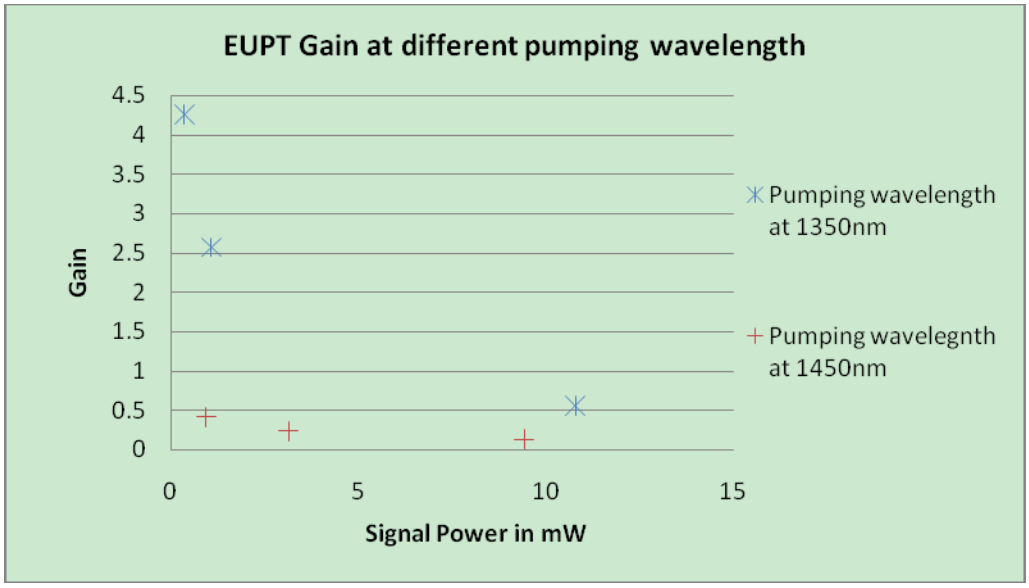

Fig. 4.33 EUPT simulation with different pumping wavelength

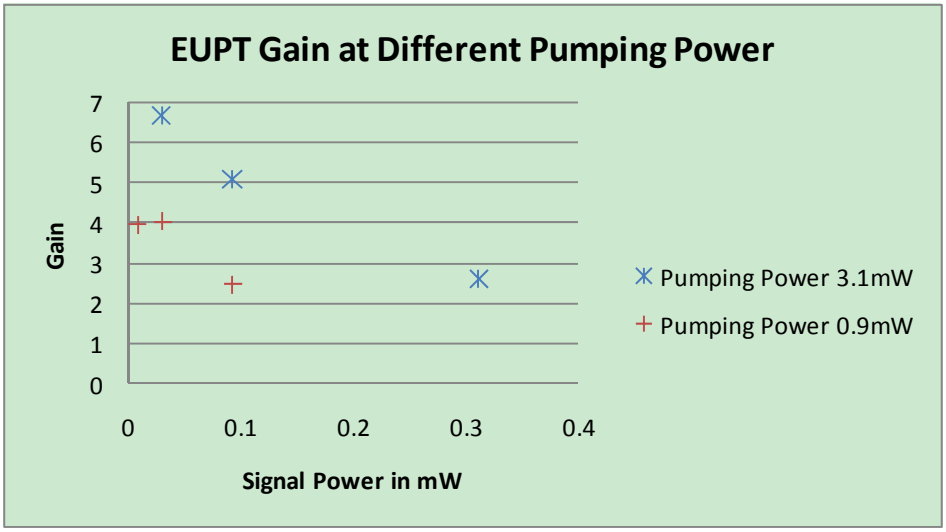

Fig. 4.34 EUPT simulation with 1.45μm wavelength pumping and different pumping power

In order to achieve higher gain at the practically feasible pumping wavelength of 1450nm, we increase the αL value to ~14 and simulated the EUPT gain at different pumping and signal power level. The result is shown in Fig. 4.34. The achievable gain increases compared to the case where αL is ~7. Meanwhile, high pumping power could lead to higher signal gain for certain signal power level when αL is kept the same.

If the pumping wavelength is changed to 1490nm, we expect the available signal gain to reduce again for the same αL. Similar to the case of 1450nm wavelength pumping, we first compare the effect of different αL. The result is shown in Fig. 4.35 where αL value of 7 and 14 is compared while the pumping power is kept constant at 3mW.

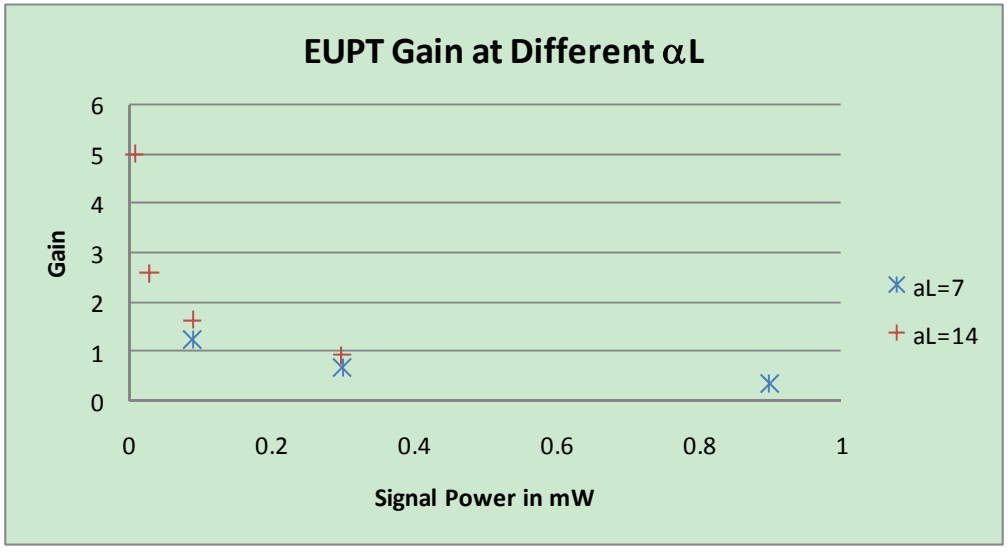

Fig. 4.35 EUPT pumping wavelength at 1490nm with different αL

From the simulation above, we can draw the following conclusions: (1) Comparing to 4-level simulation, the power consumption to reach the same performance is ~3-5 times higher because of the higher saturation intensity. (2) It is easier to achieve higher gain with larger wavelength separation between the pumping and signal light. 1.45μm wavelength pumping is ideal, but 1.49μm pumping can still be used. (3) Increasing the device length has almost the same effect as increasing the effective absorption of the waveguide, so we can use more QWs to get shorter device length.

Effect of index change

The relationship between carrier induced gain/absorption changes and the refractive index changes in semiconductor materials have been investigated by researchers over the years. It turn out that for common III-V semiconductor materials, there are conditions whereby the large gain/absorption coefficient changes are accompanied by minimal refractive indexes changes. For the case of InP material [72] with bandgap wavelength of 926nm, at wavelength slight above the bandgap of 887nm, the carrier density change from $3x10^{17}/cm^3$ to $10^{18}/cm^3$ are accompanied by near zero index changes, while at the same time, the gain coefficient will change by more than 0.6/um at the same wavelength. In other words, it is possible for the device to operate with significant absorption or gain change without the additional distortion from refractive index changes.

4.4.3 Comparison with $\chi^{(3)}$ medium

As discussed earlier, there are two basic problems with $\chi^{(3)}$ or $n^{(2)}$ materials. First, non-square pulses will experience frequency chirping because the nonlinear phase shift induced will

vary with the pulse intensity profile, resulting in spectral broadening under self- or cross- phase modulation [54]. Second, while it is desirable to achieve switching gain so that a weak control beam can switch a strong signal beam, in practice when the control beam induces π phase shift, the much stronger signal beam will experience self-phase modulation of multiple π, resulting in serious spectral broadening as well as encountering multi-photon absorption [54]. These problems make the devices not very cascadable, which is essential for complex circuits.

In this section we will show by simulation the frequency chirping experience by a Gaussian pulse passing though a $\chi^{(3)}$ medium with π phase shift as well as a pulse passing though the GAMOI based photonic transistor.

First we simulated the pulse operation of the EUPT device. The power supply beam is at wavelength of 1450um with power of 4.3mW. The input signal pulse has $1/e^2$ pulse width of 100ps and peak pulse power of 0.043mW at wavelength of 1550nm as shown in Fig. 4.36. The output pulse is also plotted out in Fig. 4.36. And the input/output pulse spectrum is compared in Fig. 4.37. The output pulse suffers slight broadening from the medium response time, however, the pulse shape in both temporal and spectral domain is retained quite well. And the switching has a gain of ~14.

Next we simulated the pulse operation of the EDPT device. The power supply beam is at wavelength of 1550um with power of 0.43mW. The input signal pulse has $1/e^2$ pulse width of 100ps and peak pulse power of 4.3mW at wavelength of 1450nm as shown in Fig. 4.38. The output pulse is also plotted out in Fig. 4.38. And the input/output pulse spectrum is compared in

Fig. 4.39. Again, the EDPT device is able to retain the pulse shape in both temporal and spectral domain quite well. And the switching has power efficiency of ~58%.

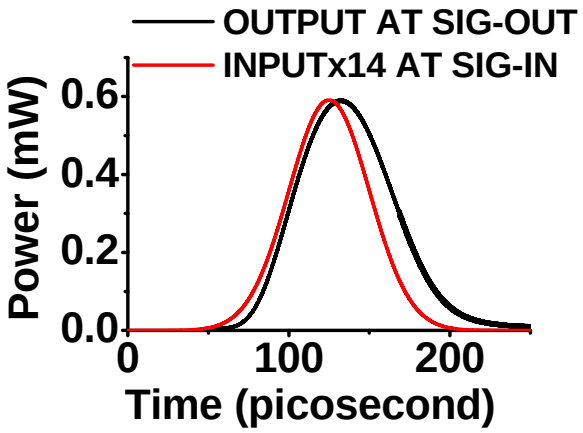

Fig. 4.36 EUPT input and output in time domain

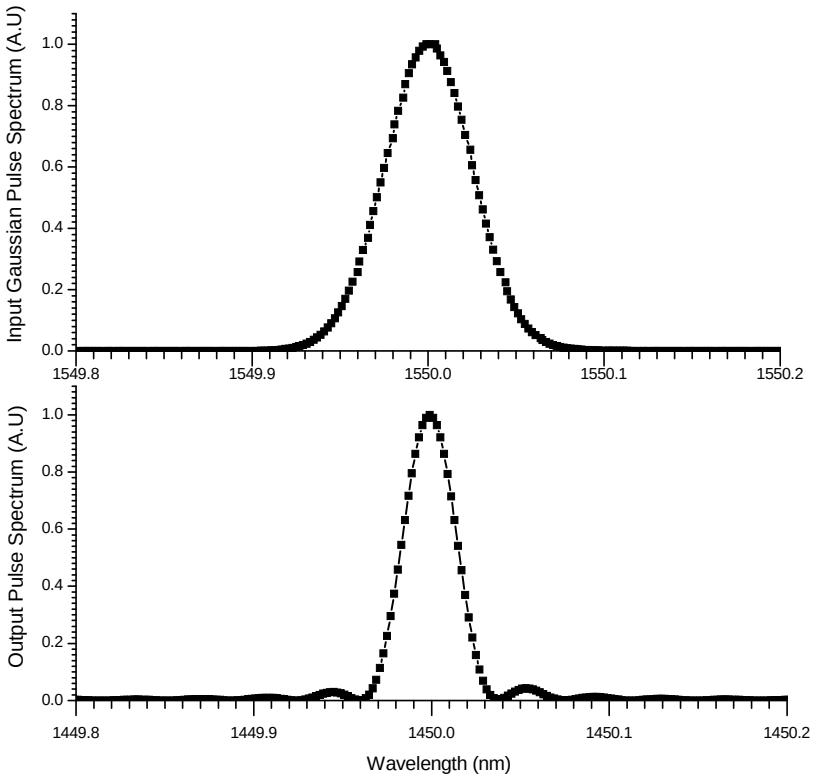

Fig. 4.37 EUPT input and output in spectrum domain

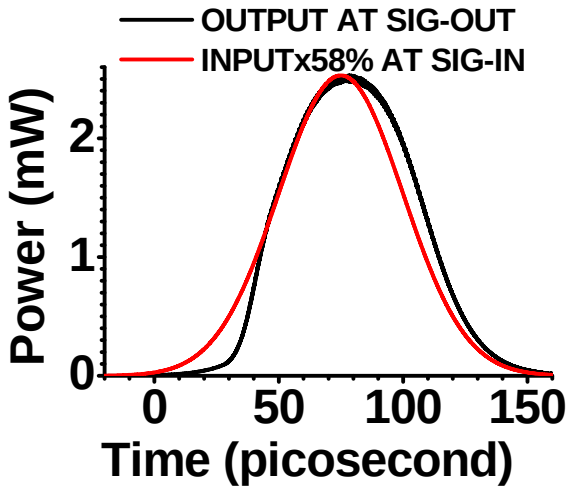

Fig. 4.38 EDPT input and output in time domain

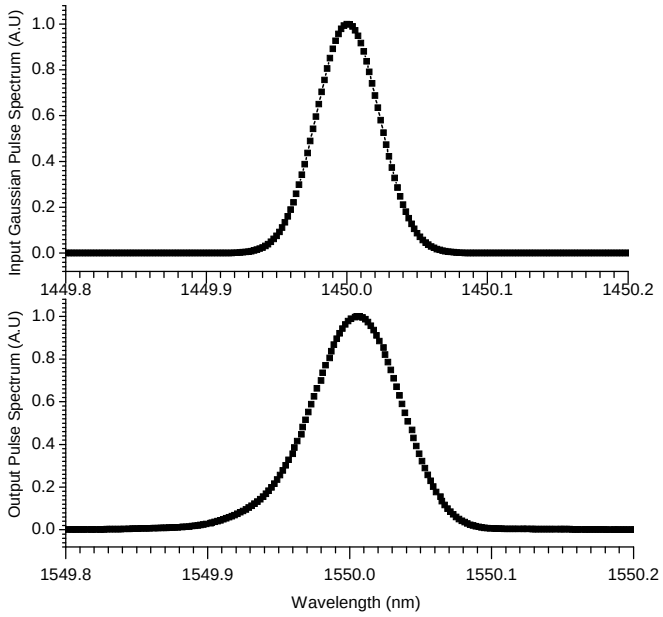

Fig. 4.39 EDPT input and output in spectrum domain

The $\chi^{(3)}$ simulation: the medium has a $\chi^{(3)}$ coefficient of $2.8\text{x}10^{-16}\text{m}^2/\text{V}^2$ and the structure involved is a weakly guiding optical waveguide with core refractive index of 3.55 and cladding refractive index of 3.5. The total length of the $\chi^{(3)}$ medium is 100um, so a Gaussian pulse with peak power of $1.2\text{x}10^8\text{W/cm}^2$ will experience π phase shift. The before and after pulse spectrum is shown in Fig. 4.40, where obvious distortion can be found from the pulse spectrum after passing through the medium.

The GAMOI based photonic transistor device shows obvious advantages in retaining the original spectrum profile of the input pulse. The minimal changes in the signal pulse spectrum from the EUPT device also suggest that the main switching mechanics of the device is the

gain/absorption modulation, instead of the refractive index changes, even in the case of operating around the bandgap of the semiconductor material, where carrier induced refractive index change can be large.

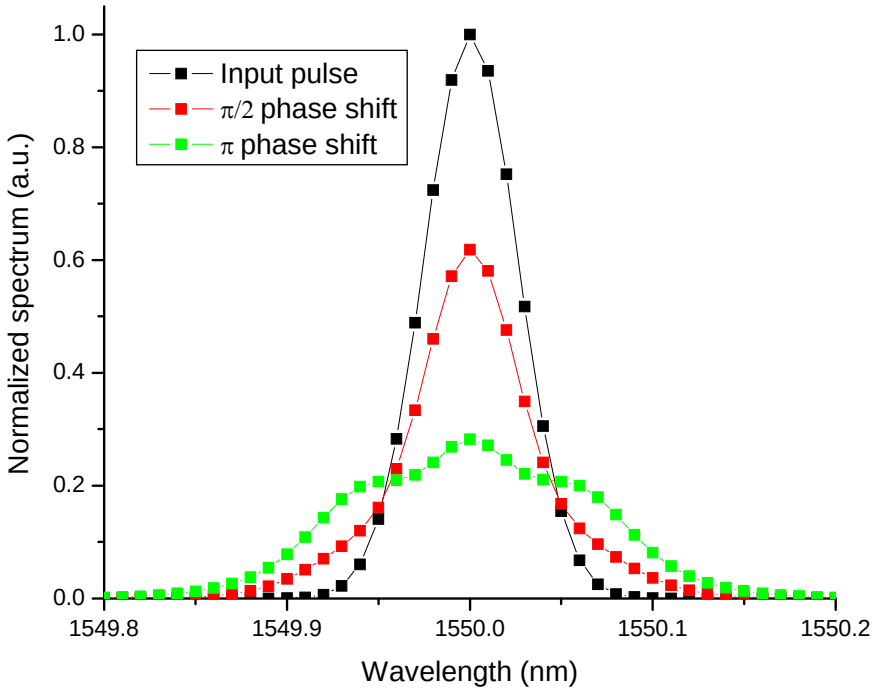

Fig. 4.40 Spectrum broadening in $\chi^{(3)}$ medium

4.5 Initial Measurement Results - Saturation and Pump-probe in Quantum Well Intermixed Waveguides

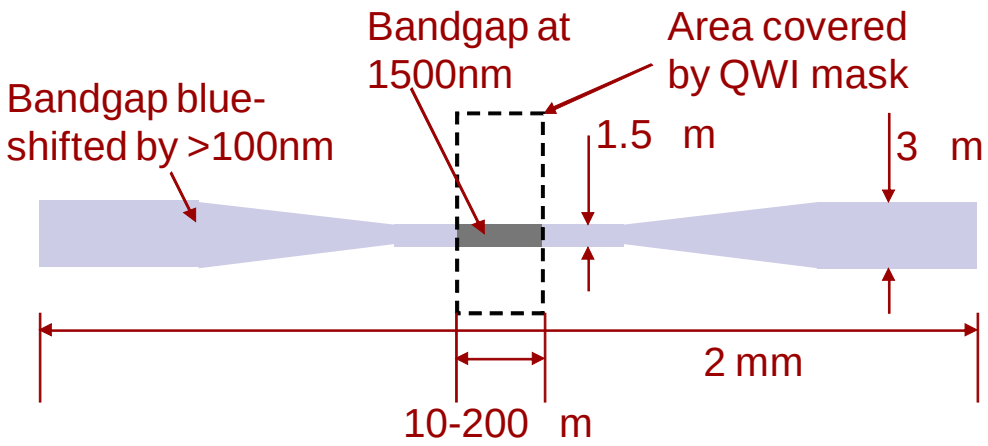

Fig. 4.41 Quantum well intermixing measurement waveguide structure

Initial fabrication and measurement work is carried out to study the basic saturation behavior of the semiconductor material. The waveguide structures we fabricated is shown in Fig. 4.41. By using quantum well intermixing, most areas of the wafer are bandgap blue-shifted to transparency, except areas at the center of the waveguides protected by SiO_2 mask. After the quantum well intermixing, 400nm SiO_2 is deposited as the mask for InP deep etching. The SiO_2 mask is patterned by optical lithographically and etched in RIE. The photoresist is then removed and the wafer is etched in ICP chamber to form 3μm-high ridge waveguide structures. The dimensions of the waveguide are shown in Fig. 4.41 with the total length of the waveguides being ~2mm. At the input and output side of the waveguide width is 3um for optical coupling, the width is then reduced to 1~1.5um by a waveguide taper. The center region of the waveguide

has various lengths ranging from 10um to 100um. The bandgap of the waveguide is at ~1380nm, except the center region, which keeps the original bandgap of ~ 1550nm.

The optical source used in the experiment is a Ti-Sapphire laser pumped Optical parameter oscillator with 130fs optical pulse output. The pulse is then passed through a grating-pulse-stretcher (Fig. 4.42) to form 30ps pulse with frequency width (FWHM) of ~3.0nm. The pulse is then used for both self-saturation and pump-probe experiments. The pulse is split to pump and probe beams that could be temporally delayed with respect to each other. The signal is detected by Hamamatsu streak camera with 2ps time-resolution. The spectral information is recorded by Spex-500M with 0.02nm spectral-resolution. Energy of the pump and probe pulse is monitored by the calibrated New Focus IR photo-receiver.

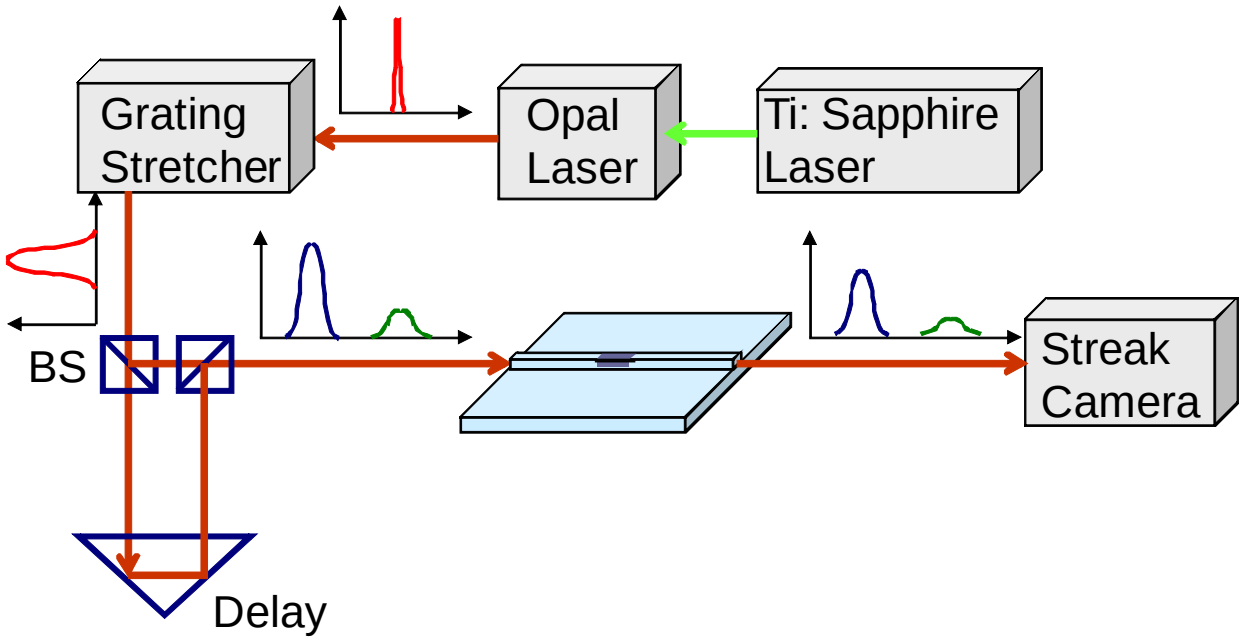

Fig. 4.42 Optical setup for pump-probe experiment

First we studied the absorption saturation of the picosecond pulse at wavelength close to band edge. The input pulse width is ~30ps with FWHM width of 2.5nm centered at wavelength 1510nm as shown in Fig. 4.43. The active region length in this case is 50um. Fig. 4.43c shows the waveguide transmissivity as a function of the peak pulse power. The power value shown on the plot refers to the optical power inside the waveguide, coupling loss has already been subtracted. From the data it can be estimated that the saturation intensity is about 10kW/cm^2 for our sample if the spontaneous decay time is ~3ns.

Now we know that in the waveguide structure we have, self-saturation of 30ps pulse required optical power ~ 20mW. There are ways to reduce the power even further. Since ultimately the saturation effect is dependent on the intensity, so as long as the intensity is the same, the power can be reduced if we reduce the optical mode size. If instead of 1.5um waveguide, we use 0.3um deep etched waveguide, the mode size will be reduced by factor of 5. If we try to further reduce the vertical optical mode size by using thin film wafer boding, so the index confinement is much stronger, we can further reduce the mode size by factor of about 4. So it is possible to observe similar effect with only ~1mW optical power if the thin film nanowaveguide is used.

Pump-probe experiments is also carried out using the techniques discussed above. The pump and probe pulse both centered at wavelength ~1520nm with a delay of 605 ps as shown in Fig. 4.44a. The pump-probe experiment result is shown in Fig. 4.44b. The red curve is the output of the probe beam without pumping, the black curve is the output of the probe beam with

pumping. The effect of the pumping beam can be seen from the 3dB increasing in probe beam output.

In summary, we describe the fabrication of area-specific 10-100μm long absorption region in mm-length waveguides. Self-saturation and pump-probe experiment of picosecond pulse in the ultra-short absorptive region is performed. The results show the feasibility of the low-energy quantum well intermixing process in realizing integrated nanophotonic devices with small active and passive regions.

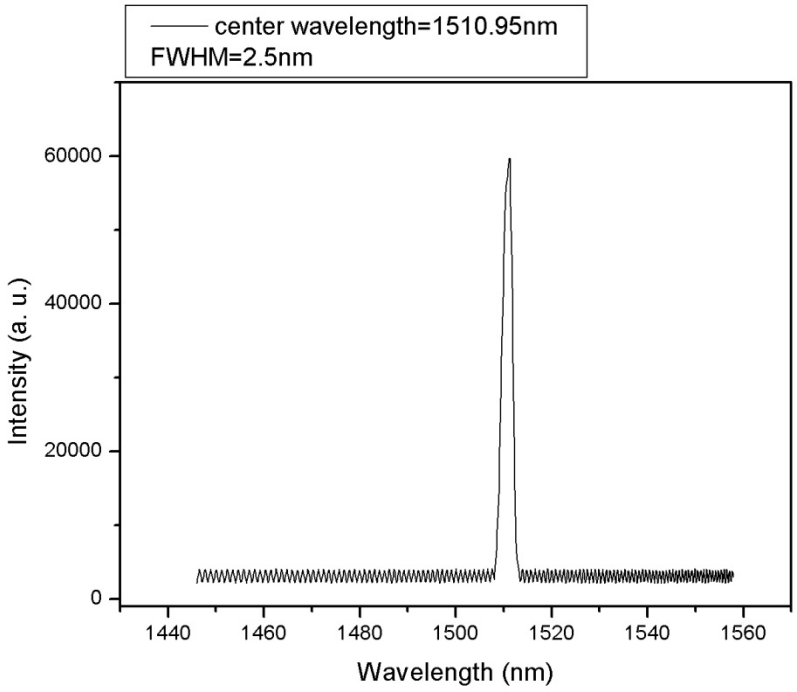

(a)

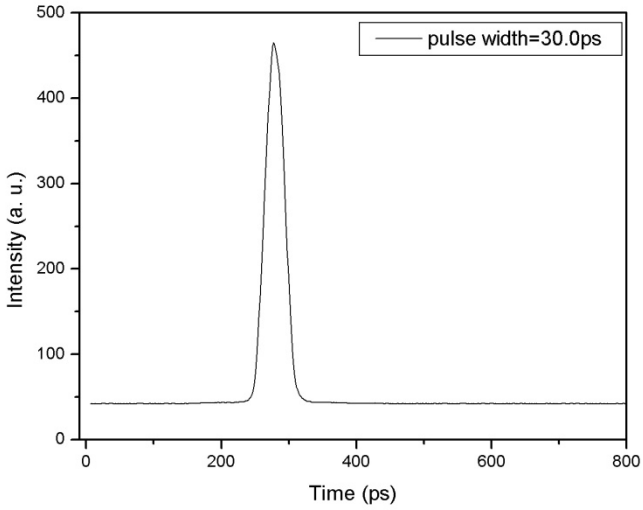
pulse width=30.0ps
Intensity (a. u.)
Time (ps)
0
100
200
300
400
500
0
200
400
600
800

(b)

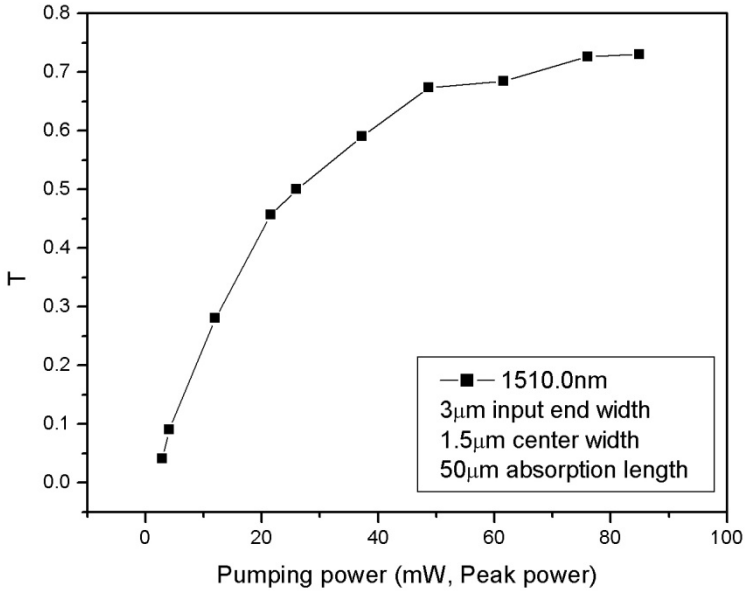
T
Pumping power (mW, Peak power)
1510.0nm
3μm input end width
1.5μm center width
50μm absorption length
0.0
0.1
0.2
0.3
0.4
0.5
0.6
0.7
0.8
0
20
40
60
80
100

(c)

Fig. 4.43 Self saturation of a 30ps optical pulse at wavelength 1510 μm, (a) pulse shape in frequency domain, (b) pulse shape in time domain, (c) transmissivity as function of input pulse power.

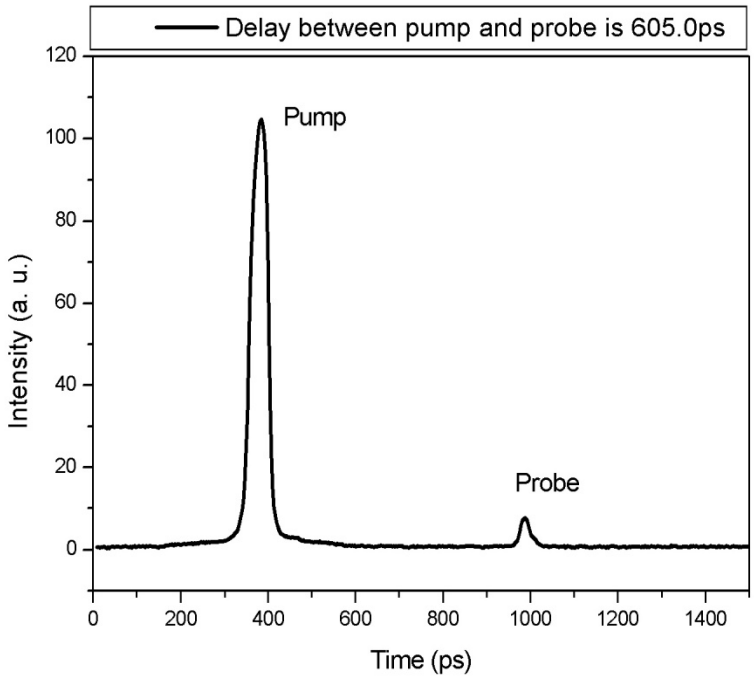

(a)

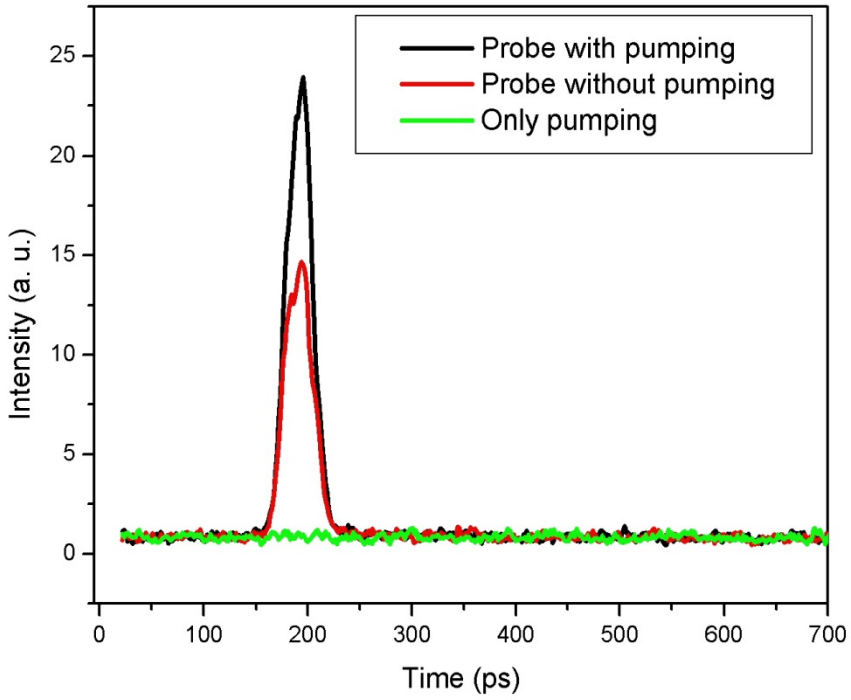

(b)

Fig. 4.44 Pump-probe experiment in bandgap shifted optical waveguide: (a) delay between pump and probe pulse (b) probe output with and without pump.

4.6 Ultra Compact Mode Order Converter

From section 4.3 we can see that to achieve the optimal performance of the GAMOI based energy up photonic transistors it is necessary to launch in both 0th order and 1st order optical mode into the device. Thus it is desirable to have a compact mode order converter that can achieve easy converting between 1st order mode and 0th order mode. Such optical mode

order converter can offer an additional dimension of freedom in photonic integrated circuit design, as different orders of optical mode have different effective refractive indexes. For example, in the case of a directional coupler with waveguides supporting both 0th order and 1st order modes, different coupling length can be obtained from the same coupler for the two different mode orders.

In this section, we propose a new type of optical mode converter based on an ultra-compact interferometric structure formed by nano-waveguides. The mode order converter is a waveguide-based interferometer as shown in Fig. 4.45. The two arms of the interferometer consist of single mode nano-waveguide structures with an optical path difference of π. In a 0 to 1st order mode conversion, the input end is a single mode waveguide supporting only 0th order mode, while the output end is a multimode optical waveguide, which can support both 0 and 1st order mode. As the beam coming in form the input waveguide, it is split 50/50 by a Y-splitter to the two arms of the interferometer and phase difference of π is introduced between the two beams. The two beams then recombine at the output waveguide end and forms a 1st order mode. The structure can also be used as 1st to 0th order mode converter if the propagation direction is reversed.

The nano-scale waveguides have strong refractive index contrast between the core and cladding. As a result, large angle Y-splitters and sharp bending are possible, making the resulted device ultra compact.

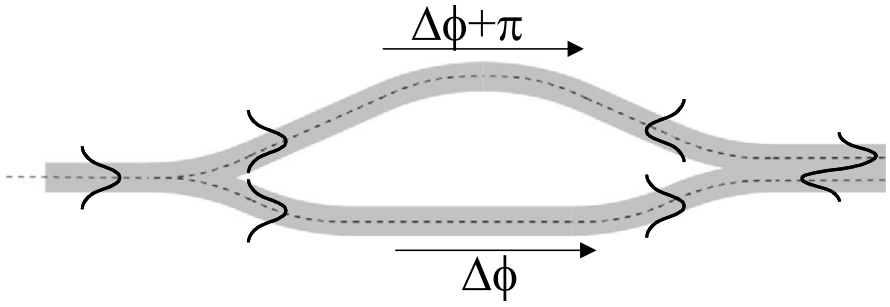

Fig. 4.45 Schematic of the optical mode order converter

4.6.1 Design and Simulation

The detailed structure of the optical mode order converter is illustrated in Fig. 4.46. The input nano-waveguide width is W_1, which is chosen so only 0th order mode is well supported in the waveguide. The input waveguide is then split to two arms via Y-junction. The two arms have the same waveguide width W_1 as the input waveguide. The light beam in the two arms will recombine at the output waveguide with width W_2. The output waveguide width is chosen so 1st order mode is also well supported. In the output waveguide, the distance between the two intensity peaks in the 1st order mode is defined as W_{off}.

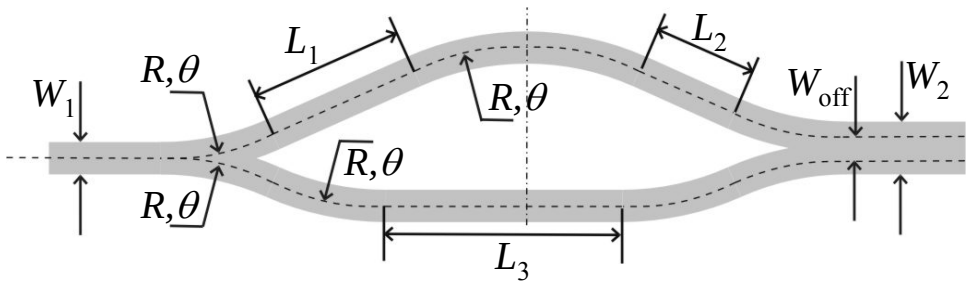

Fig. 4.46 Schematic of the optical mode order converter

The lower arm of the interferometer consists of two s-bend sections connected by a straight section with length L_3. Each s-bend is formed by two arc with radius R and enclosed angle θ. The left half of the upper arm starts with an arc section with the same radius R and angle θ, followed by a straight section with length L_1, which is then followed by the identical arc section. The same structures are repeated for the right half of the upper arm, except that the straight section is shorter with length L_2. Note that the following equations holds for L_1, L_2 and L_3:

$$L_1 \cos\theta + L_2 \cos\theta = L_3$$

$$L_1 \cos\theta + L_2 \cos\theta = L_3 \tag{4.14}$$

Since both upper and lower arms have exactly same arc section length, the phase difference $\Delta\phi$ is introduced by the length difference in the straight section only. $\Delta\phi$ can be expressed as:

$$\Delta\phi = 2\pi n_{eff} \cdot (L_1 + L_2 - L_3) / \lambda = \pi . \tag{4.15}$$

At wavelength of 1550nm, we design the mode converter based on III-V semiconductor waveguide with core refractive index of 3.2 (InP) and cladding refractive index of 1.54 (BCB). R is chosen to be 10um to minimize the bending loss. For the case where W_1=0.35um, N_{eff}=2.66 for order TE mode. In order to minimize reflection loss at the joint between waveguide W_1 and W_2, we choose W_2 so the effective refractive index of 1st order mode in waveguide W_2 will match the effective refractive index of 0th order mode in waveguide W_1. For N_{eff} of 2.66, W_2 is 0.75um. W_{off} can be calculated to be 0.4um in this case, with L1=6.56um, L2=4.78um. θ should

be minimized without increase the length of the device, we choose θ=13° in our design, as increasing beyond 13° has minimal effect in reducing device length while will inevitably increase the device loss.

Finite difference time domain method (FDTD) [17, 18] is used to simulate the optical mode order converter performance. The FDTD simulated electromagnetic field pattern is shown in Fig. 4.47. The mode order converter shows 94% converting efficiency for the designed wavelength of 1550nm.

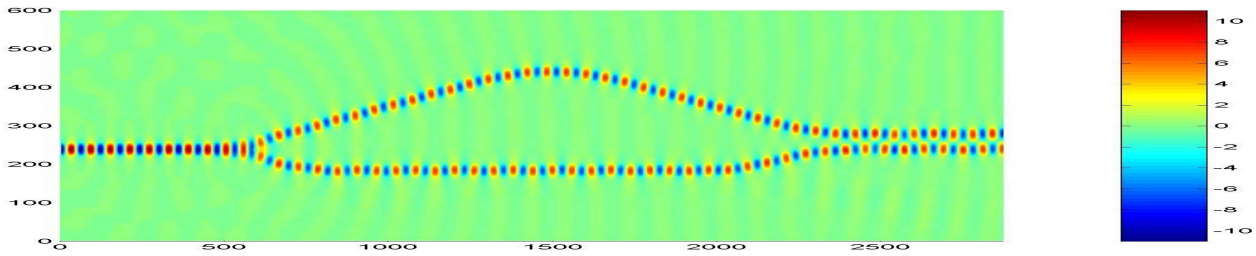

Fig. 4.47 FDTD simulation result of 0th order to 1st order mode conversion for TE mode at wavelength of 1.55 micron.

4.6.2 Fabrication

In initial fabrication, we realized the nano-waveguides via deep etched double-trench structure similar to that shown in [75]. 50 micron long tapers are used on both the input and output end of the device to taper the nano-waveguide to 3um wide so easy coupling through lens system can be realized.

We used commercially epitaxial grown InGaAs-InP quantum well wafer with ten 5.5nm unstrained InGaAsP quantum wells separated by 12nm thick barriers. The wafer are bandgap blue shifted by >100nm to transparency via quantum well intermixing technique [12].

After the quantum well intermixing, 300nm PECVD SiO_2 is deposited as the mask for InP/InGaAsP deep etching. 300nm PMMA 950 is then spun on as ebeam lithography resist. The ebeam lithography is performed on a JEOL9300 ebeam system. The PMMA resist is then developed in MIBK: IPA=1:3 developer for 90 seconds. The PMMA mask is transferred down to SiO_2 mask by Oxford PlasmaLab 80+ RIE system using CHF3. The PMMA is then removed by actone and the wafer is cleaned by O2 plasma descum. The SEM picture of the mode converter is shown in Fig. 4.48. After removal of ebeam resist, the wafer is etched in PlasmaTherm ICP system to form ridge waveguide structure (Fig. 4.49). The ICP etching condition is similar to that discussed in [76]. The etching depth of ~3um is achieved in the trench. After ICP etching, the SiO_2 mask is removed. The whole wafer is planarized using BCB. After curing the BCB at 250°C for 1h, the wafer is thinned down to ~120um thickness and the wafer is cleaved to form devices. The cross section of the devices after processing is illustrated in Fig. 4.50.

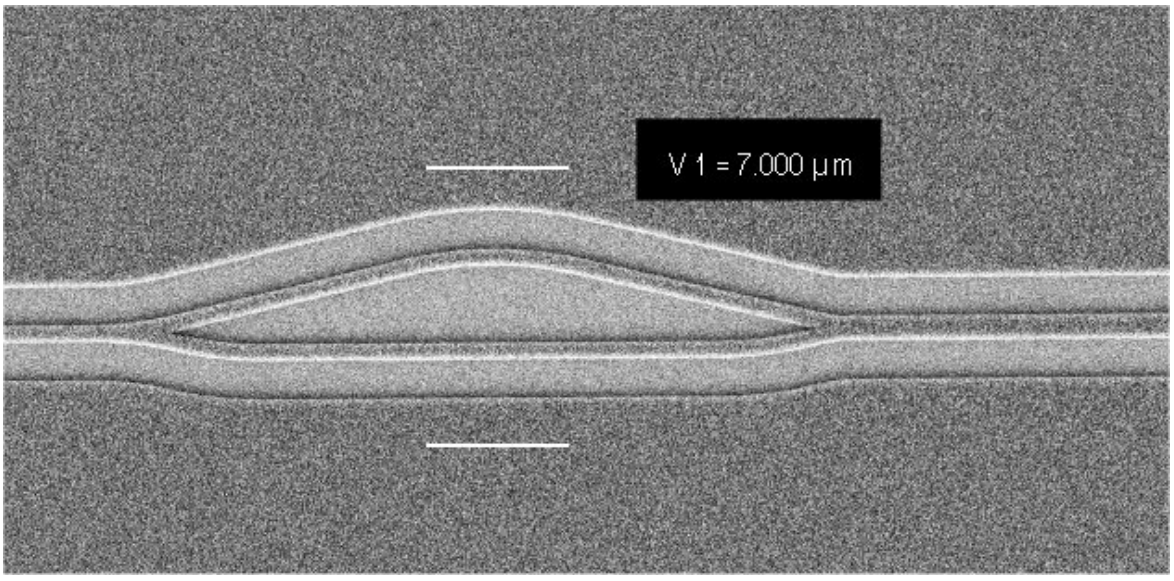

Fig. 4.48 SEM picture of the mode order converter after SiO_2 etching

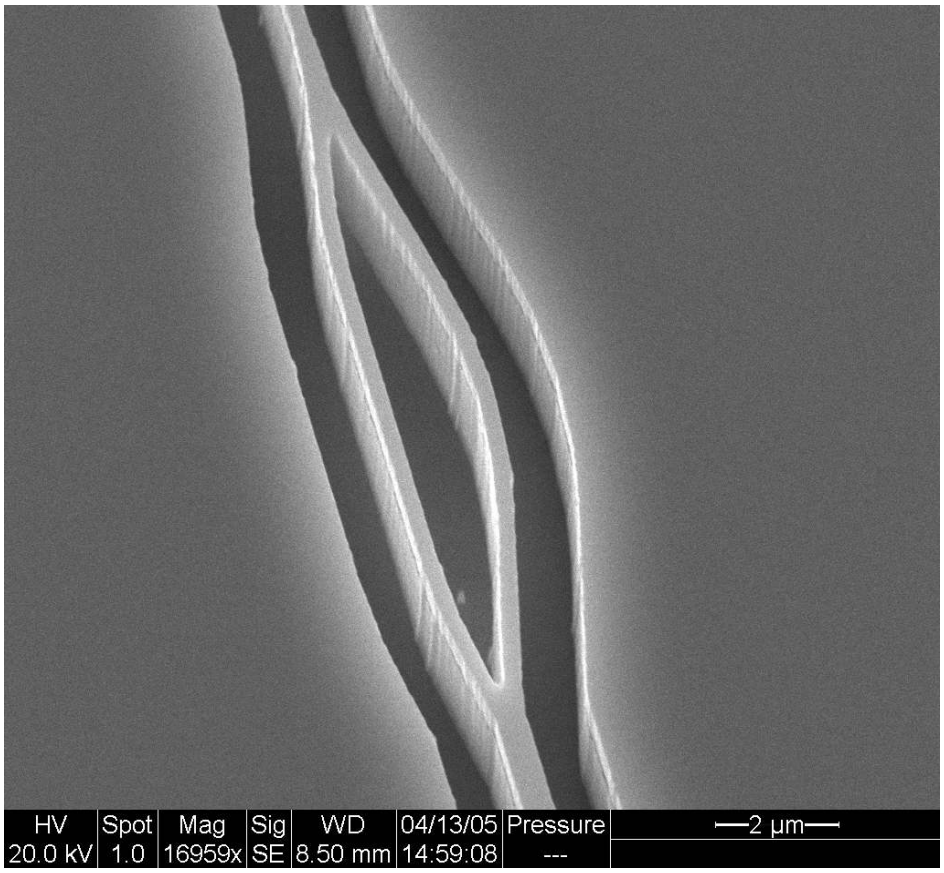

Fig.4.49 SEM picture of the mode order converter after ICP etching

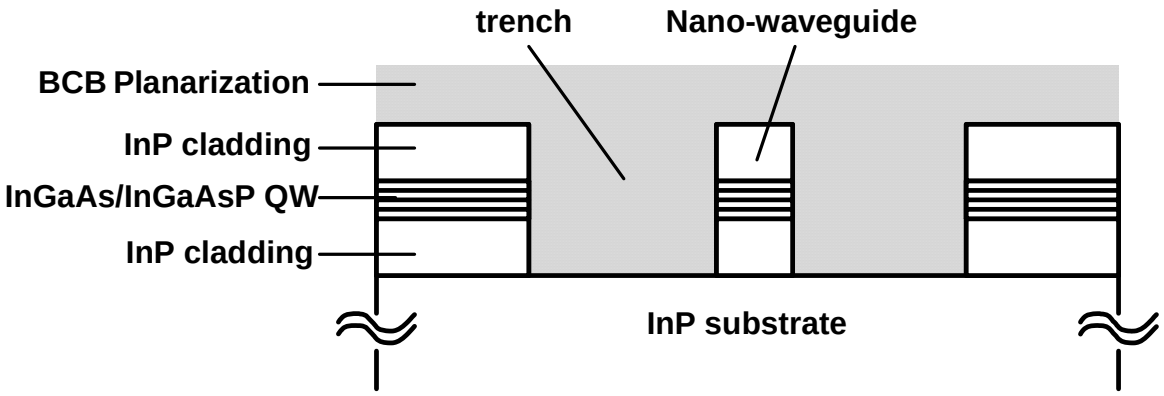

Fig. 4.50 Cross section structure of the fabricated mode order converter.

4.6.3 Experiment

The fabricated devices are then tested with a tunable laser source as the optical input. The laser light is focused to the input end of the device. The output optical mode is captured by an IR camera. The output of the mode converter is compared to the output from a straight single mode optical waveguide with the same width as the input waveguide of the mode converter. The result is illustrated in Fig. 4.51. Fig. 4.51(a) shows the output optical mode from the single mode waveguide, while Fig. 4.51(b) shows the output optical mode form the mode converter. The results are compared to the optical mode calculated numerically by C2V software, and the result is plotted out in Fig. 4.51(c) and (d), respective. The loss of the mode converter is also calibrated by comparing the output power of the mode converter to the straight waveguide device. The fabricated mode converter has a 0.4dB additional loss, close to that predicted by FDTD simulation.

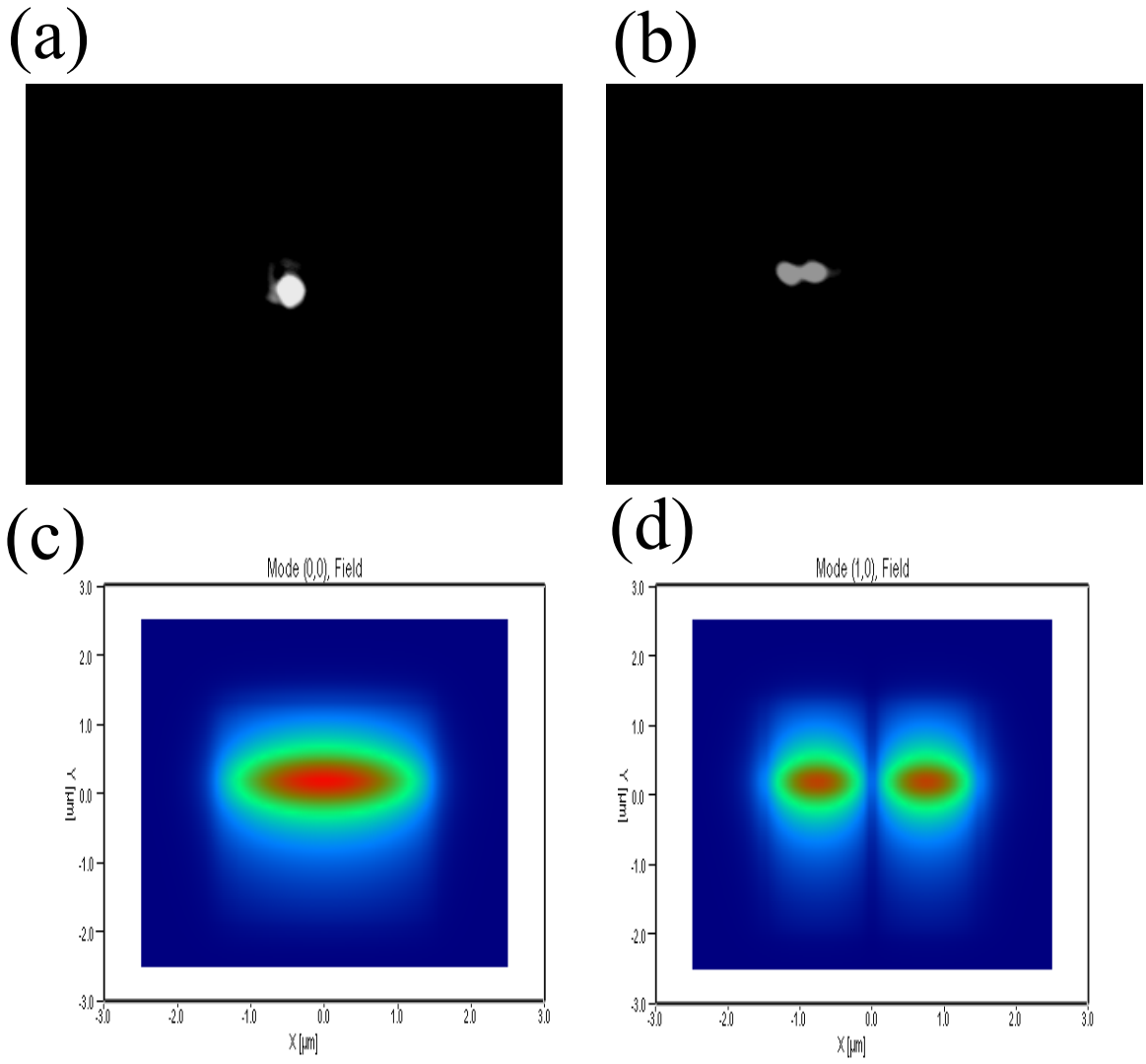

Fig. 4.51(a) IR camera image of the output from a straight single mode waveguide showing TEM 00 mode; (b) IR camera image of the output from the mode converter showing TEM 01 mode; (c) TEM 00 mode in the single mode waveguide calculated by C2V; (d) TEM 01 mode in the output waveguide of the mode order converter calculated by C2V.

In summary, we discussed the design principle of an optical mode order converter, which is capable of converting 0th order optical mode to 1st order mode, and vise verse. The initial

fabrication and measurement result of the mode order converter is also demonstrated. The Optical mode order converter could have a wide variety of interesting applications in photonic integrated circuit by offering the capability of launching either 0th order or 1st order optical mode, and realize easy converting between the two. The fabricated optical mode converter demonstrates very low loss (0.4dB per conversion) and ultra-compact foot print of less than 18um by 3um.

CHAPTER V MICRO LOOP MIRROR LASER

5.1 Introduction

Microlasers are lasers based on strongly-guiding sub-μm wide structures such as the photonic-wire laser and photonic bandgap laser [77, 78]. Microlasers are of great interest due to their low lasing thresholds and small sizes [79]. However, microlasers typically have low output powers, which limit their usefulness. Comparing to other planar microcavity such as ring or disk [80], linear cavity is advantageous as it is capable of single-end output with higher power. Deeply etched DBR gratings with semiconductor-air interface have been attempted for realizing mirrors with higher reflectivity, but only ~ 75% reflectivity was obtained because of mode diffraction loss in the air gap [81-84]. By using butt-coupled waveguide to enlarge the vertical mode size, 90% reflectivity was achieved [85]. However, it requires expensive regrowth and the cavity Q is still not high enough for microcavity applications that typically need reflectivity>95%. The realization of efficient microlaser is further complicated by the need to join a small active area to passive areas.

Recently, we proposed a novel linear geometry microlaser using micro-loop mirrors (MLM) as high reflectors [86]. By using a micro directional coupler in the MLM, a single optical output port can be realized with a small amount of output coupling so as to maintain a high cavity Q. The key to this approach is the use of high refractive index contrast nano-waveguide

structure so that the MLM consisting of single mode waveguide will have high reflectivity with compact size. Furthermore, the center part of the laser can be enlarged to provide widened gain medium for achieving even higher output power. The high index contrast structure enables short tapering length between the single mode waveguide and the widen gain region, thus maintaining the single transverse mode needed for single-frequency operation. This laser is capable of operating with only one Fabry-Perot mode under the gain curve. We demonstrate an initial fabrication using quantum well intermixing (QWI) to achieve efficient microlaser structure with active area joined to passive area without disjoint that often occurs with use of material regrowth.

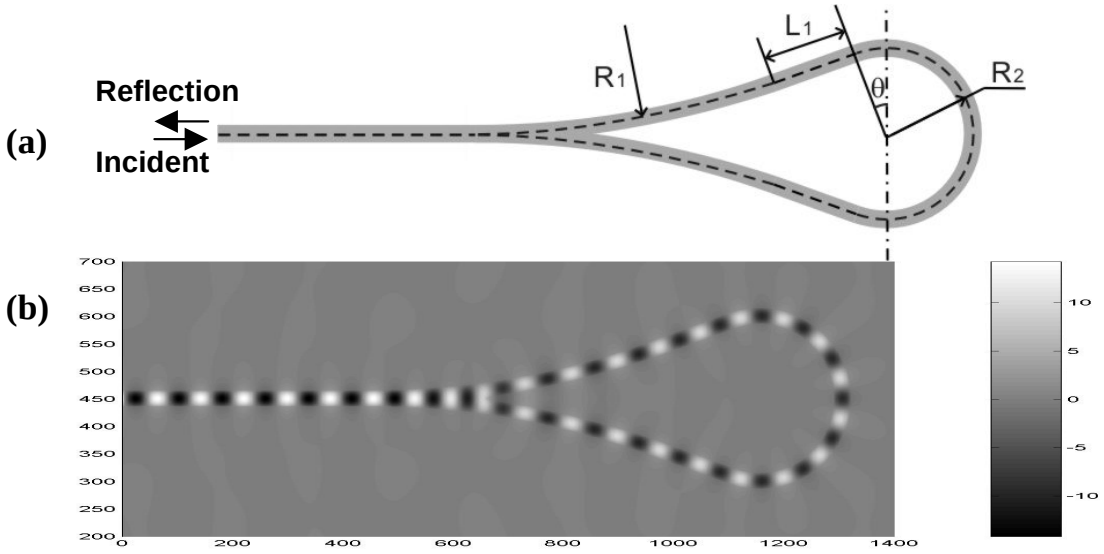

Fig. 5.1 (a) High reflectivity MLM with θ=20°, R_1=15μm, L_1~1.5μm, and R_2=1.5μm, (b) FDTD simulated magnetic field distribution when launching in CW wave at wavelength 1.55μm (total area shown 5μm by 14μm).

5.2 Theory and Design

The high reflectivity MLM is formed by connecting the two arms of a Y-splitter with a curved single mode waveguide as illustrated in Fig. 5.1(a). The main loss comes from two parts: the Y junction loss, which becomes large when the Y-junction angle θ increases, and the bending loss at the curved loop with radius R_2, which becomes large when R_2 decreases. Finite-difference time-domain (FDTD) method [87] is used to evaluate the loss of the MLM. The waveguide structure considered is 310nm wide with core/cladding refractive index contrast of 3 and 1. The simulation shows that with R_1=15μm, L_1~1.5μm, and R_2=1.5μm, the reflection is 98.6% at λ=1550nm for TE mode (with E-field propagating parallel to the plane). The FDTD simulated electromagnetic field pattern inside the MLM is shown in Fig. 5.1(b). In short, a MLM with a half-round-trip loop length of <7μm and >98.5% reflectivity can be achieved, enabling the realization of microlaser with <25μm cavity length (~10μm-long active medium), giving a large cavity-mode free-spectral-range of ~25nm (effective waveguide index is ~2).

For the laser output mirror, instead of having Y-junction as 50/50 power splitter, a 1μm-long micro directional coupler is used to form the MLM as shown in Fig. 5.2(a). Such micro directional coupler has been realized before [88]. Following the typical coupled-mode analysis, the outputs B_1 and B_2 for the directional coupler shown in Fig. 5.2(b) with input A_1 are given by:

$$B_1 = \sqrt{1-c^2}\,A_1, B_2 = -jcA_1, \tag{5.1}$$

where $c = \sin(\pi L / 2L_0)$, with L_0 being the full coupling length of the coupler.

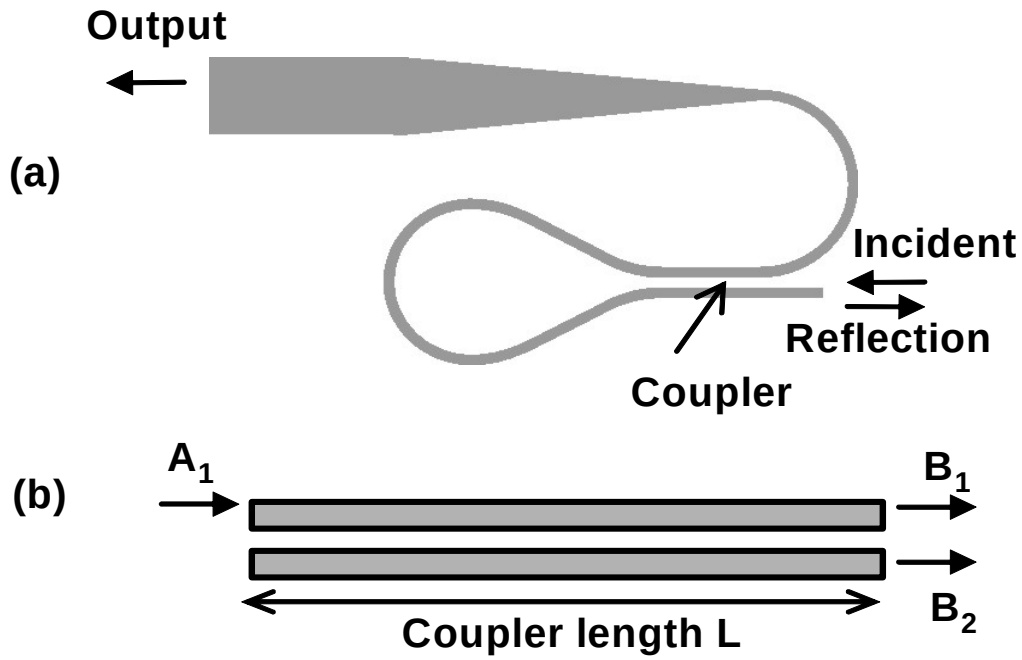

Fig. 5.2 (a) Schematics of the adjustable output MLM, (b) coupler structure used in the adjustable output MLM reflectivity calculation.

If we connect the two output ends with a curved single mode waveguide and let the coupler length *L'* deviates slightly from $L_0/2$ as $L' = L_0/2 + \Delta L$, the transmissivity *T* of the MLM can be calculated as $T = \sin^2(\pi \Delta L / L_0)$. Note that total reflection *R*=1 occurs at $L' = L_0/2$. Thus, by varying ΔL from 0 to $L_0/2$, an *R*-value of 1 to 0 can be achieved.

Next, we use a 4-level 2-electron rate-equation model [89-92] in FDTD to simulate the lasing behavior of the MLM-WGM laser. In this model, two pairs of discrete energy levels are used to model current injection dynamics in the semiconductor medium as illustrated in Fig. 5.3. The use of 2 electrons with the inclusion of the Pauli Exclusion Principle enables us to model

intraband carrier relaxation for holes and electrons. The model assumes the following parameters typical for semiconductor materials [93]: carrier spontaneous decay time τ_{sp}=1 nsec; carrier intraband relaxation time τ' =100 fsec; dipole transverse relaxation rate $\delta\omega=3.9\times10^{13}$Hz (it corresponds to 50 nm linewidth); and ground-state electron population density of 6×10^{16}cm^{-3} for each energy pair ($N_1\Leftrightarrow N_2$ and $N_0\Leftrightarrow N_3$) that gives an on-resonance absorption coefficient of $\alpha=0.6\mu m^{-1}$ and saturation intensity of I_{SAT}=1 kW/cm^2.

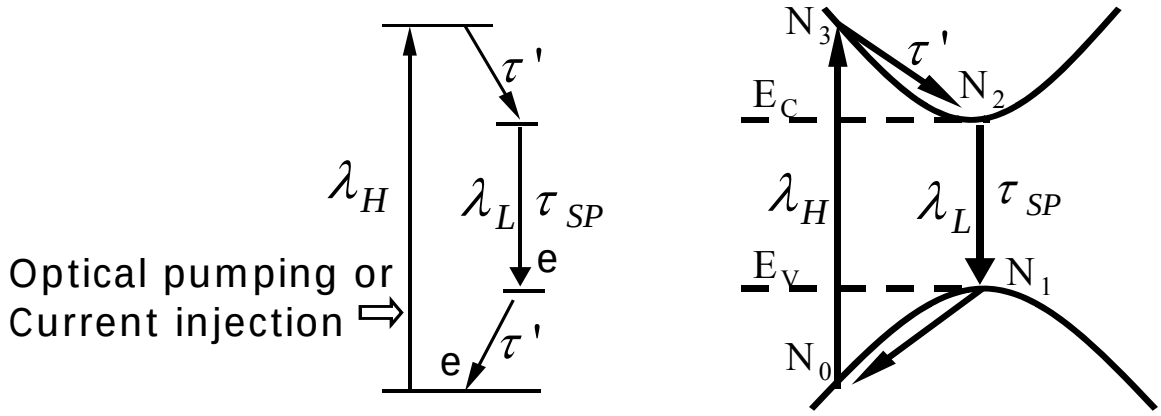

Fig. 5.3 4-level 2-electron rate-equation model for FDTD simulation of laser

For the laser of Fig. 5.4(a), the simulated electromagnetic field pattern is shown in Fig. 5.4(b) and the simulated current – output power relation of the laser is shown in Fig. 5.4(c) for which a carrier quantum efficiency of 90% is assumed in the simulation.

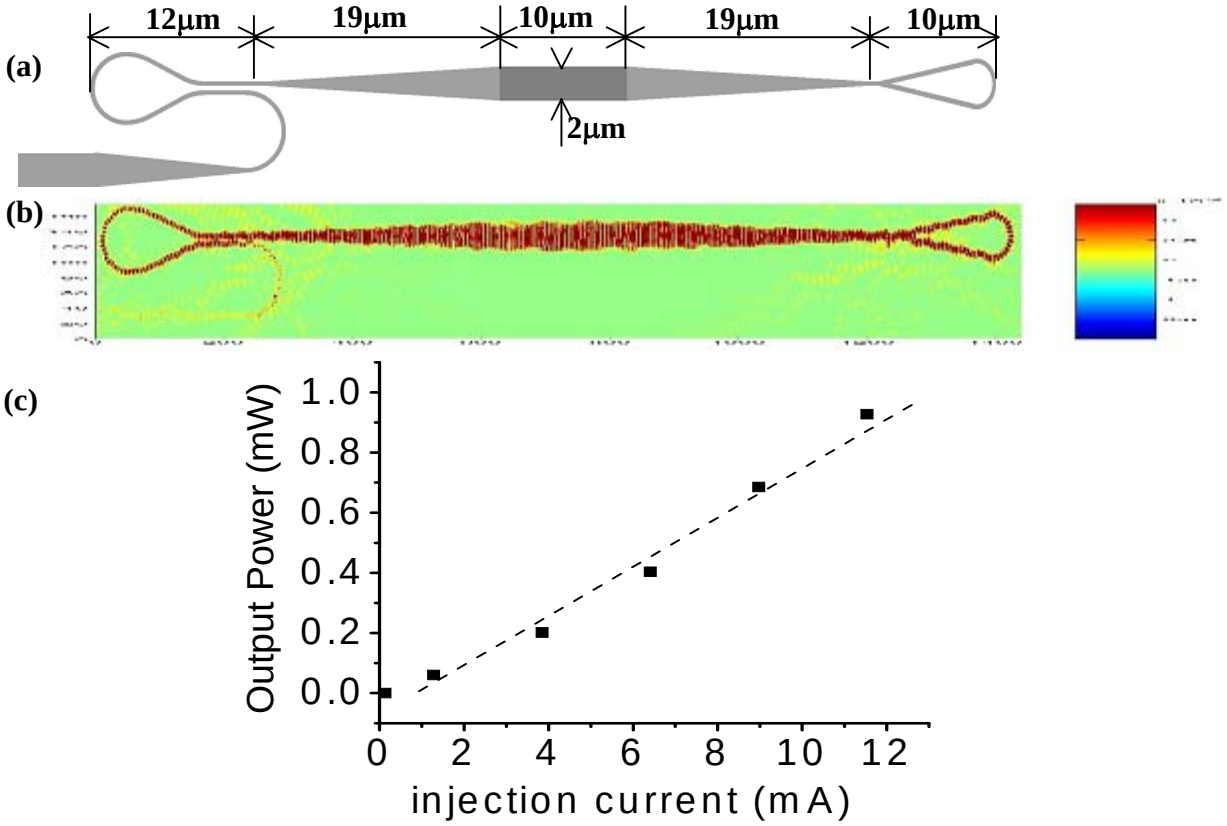

Fig. 5.4 FDTD simulation of MLM-WGM laser: (a) device structure, where the light gray part is bandgap shifted to transparency for lasing wavelength and dark gray part is not bandgap shifted; (b) electromagnetic field pattern of MLM-WGM laser when lasing; (c) plot for output power vs. current.

5.3 Fabrication and Results

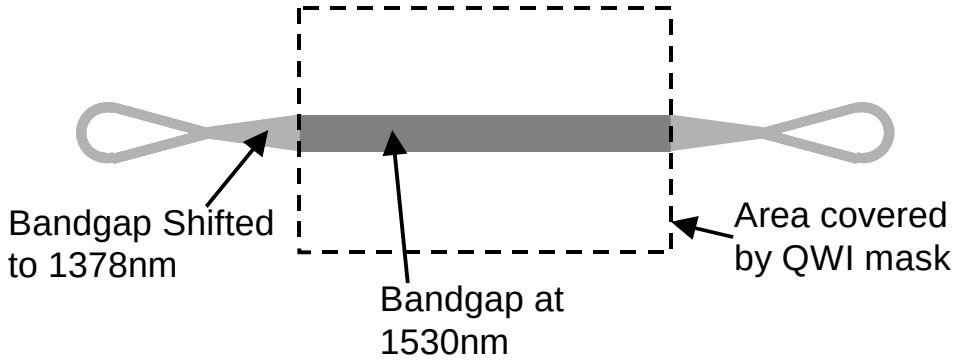

(a)

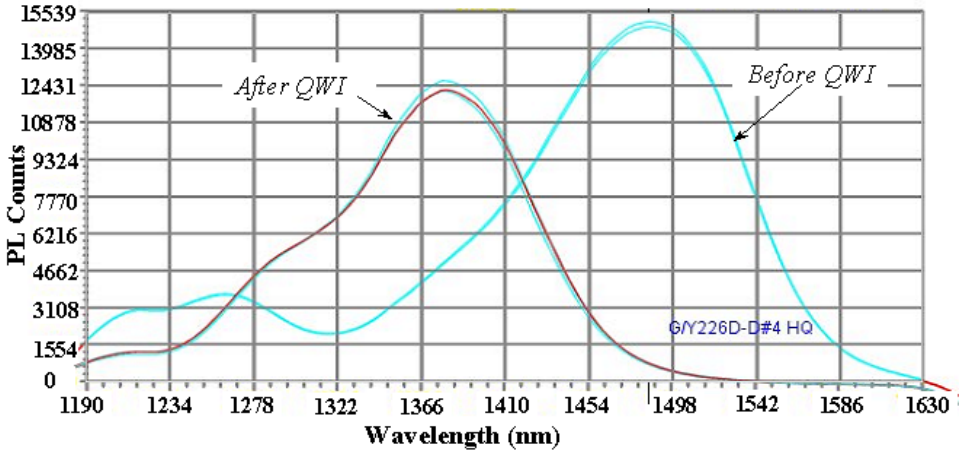

(b)

Fig. 5.5 (a) Schematic diagram of the bandgap at different sections of the fabricated micro loop mirror laser. (b) PL result for the quantum well wafer before and after quantum well intermixing measured at room temperature.

In initial fabrication, we used high-reflectivity MLMs on both ends of the cavity as illustrated in Fig. 5.5(a). The waveguide width is wider than simulation with similar loop dimensions. We used commercially grown epitaxial InGaAs-InP quantum well wafer with five 5.5nm unstrained InGaAsP quantum wells separated by 12nm thick barriers. In order to prevent

excessive heating in MLM region, the mirror sections at both ends of the laser are bandgap blue shifted by >100nm to transparency via quantum well intermixing technique [94], as shown by the lighter-color area in Fig. 5.5(a). 1.2μm thick SiO_2 is deposited as ion implantation mask and windows are then opened for areas where bandgap will be shifted. The sample is then ion-implanted with phosphorus ions at accelerate voltage of 360KeV, dosage of $10^{15}cm^{-2}$ and substrate temperature of 200°C. After ion implantation, the SiO_2 is removed and the wafer is annealed in a rapid thermal processor at 650^oC for 2 minutes. The bandgap-shifted photoluminance (PL) is shown in Fig. 5.5(b). The MLM part will be transparent for the lasing wavelength with bandgap λ of ~1378nm, while the center part of the laser remains the original bandgap energy and provides optical gain under current injection. 3um-wide index guided waveguides intermixed to similar degree give a propagation loss of ~2-3 cm-1 at 1550nm.

After the QWI, 400nm SiO_2 is deposited as the mask for InP deep etching. The SiO_2 mask is then lithographically patterned and etched in RIE. The resist is subsequently removed and the wafer is etched in ICP chamber to form ridge waveguide structure. The SEM picture of the etched loop mirror before passivation and planarization is shown in Fig. 5.6. The structure is then passivated by SiO_2 and planarized using BCB. After etching back the BCB with dry etching, electrical contact windows are opened, and metal contacts are deposited. The cross-section of the laser structure with top and bottom electrical contacts is illustrated in Fig. 5.7.

The output-injection current relation of the MLM-WGM laser with 20μm long and 2μm wide center gain region is shown in Fig. 5.8. The output is collected from the top of the device

with an optical fiber to a detector. The threshold of the laser is ~0.4mA. The threshold current density can be calculated to be ~1 kA/cm^2.

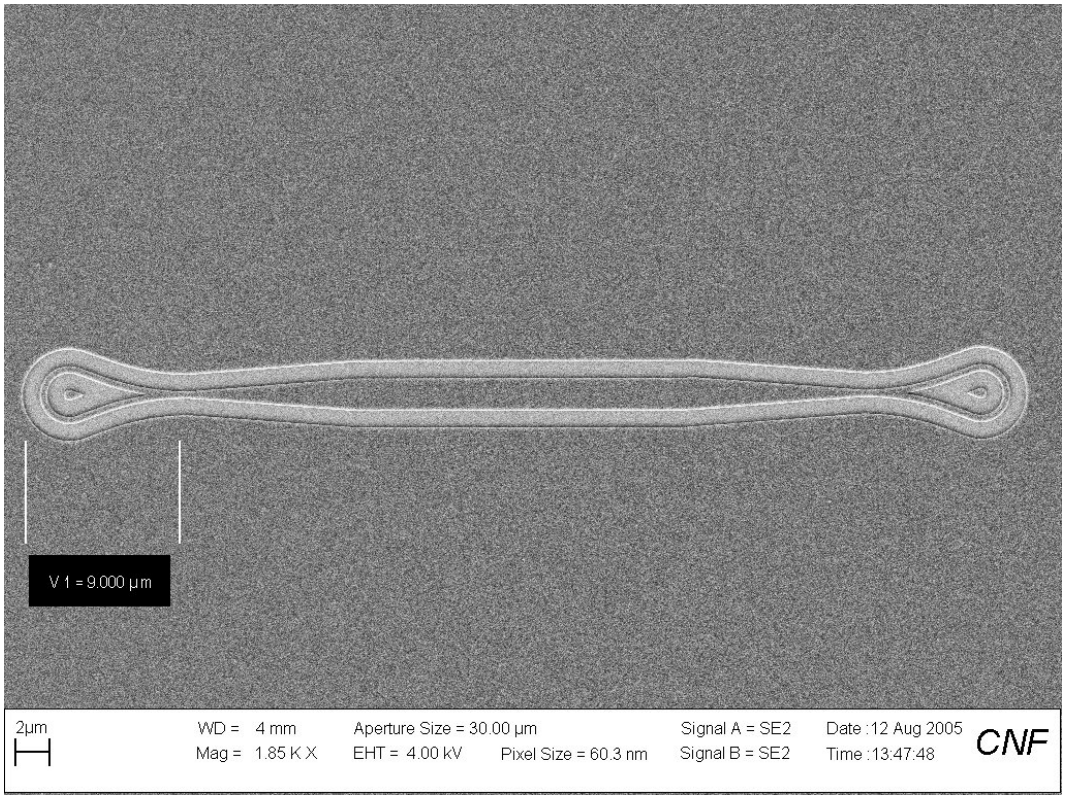

(a)

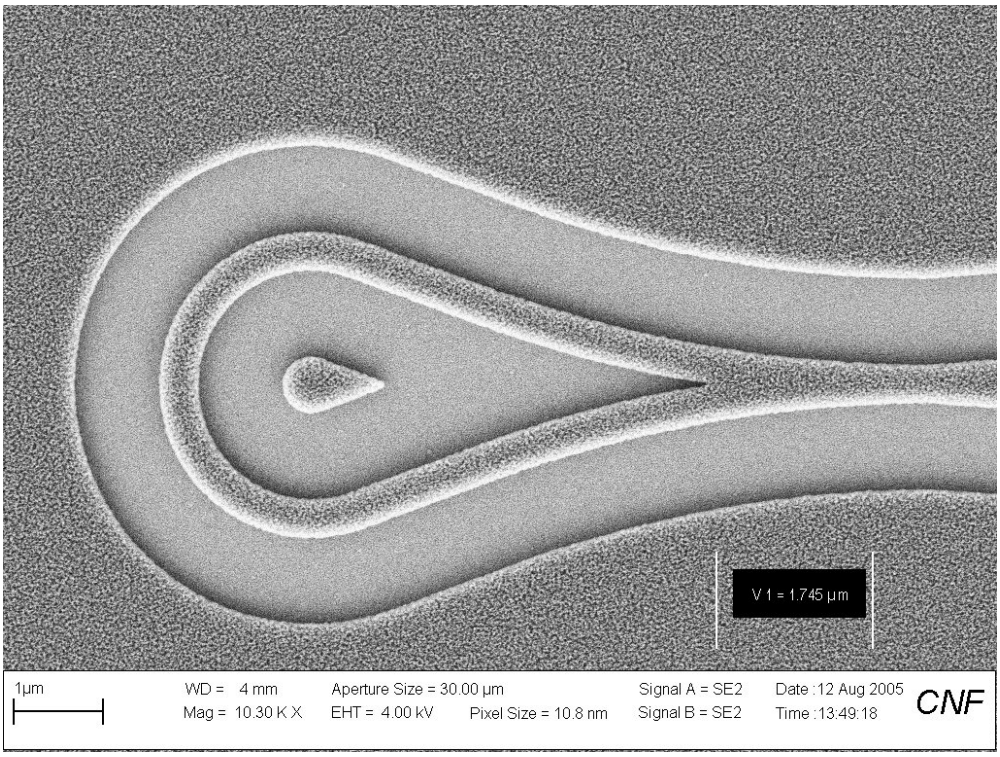

(b)

Fig. 5.6. SEM picture of the ICP etched looped mirror laser.

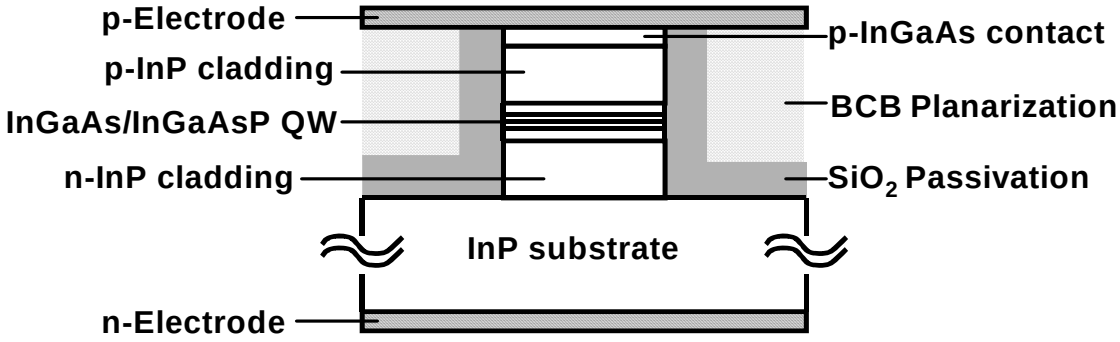

Fig. 5.7. Schematic diagram of the laser cross-section in areas with contacts

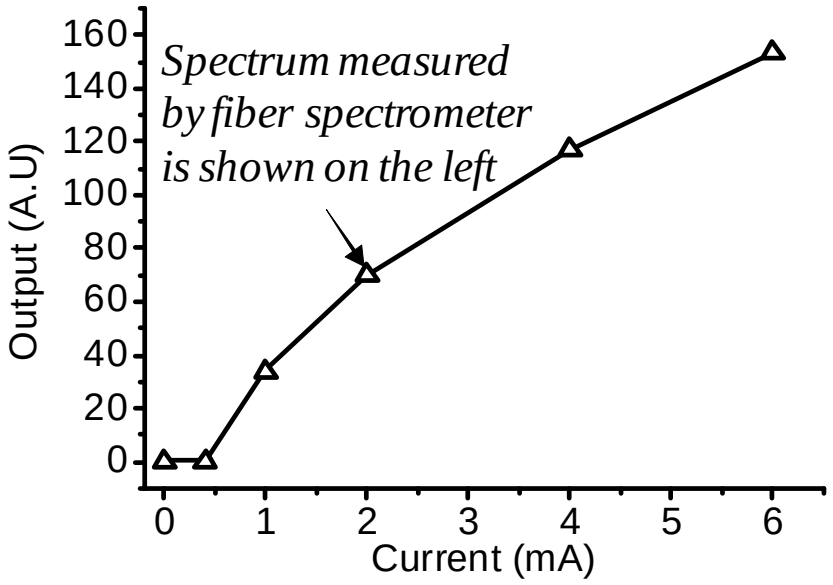
Spectrum measured
by fiber spectrometer
is shown on the left
Output (A.U)
Current (mA)
0
20
40
60
80
100
120
140
160
0
1
2
3
4
5
6

(a)

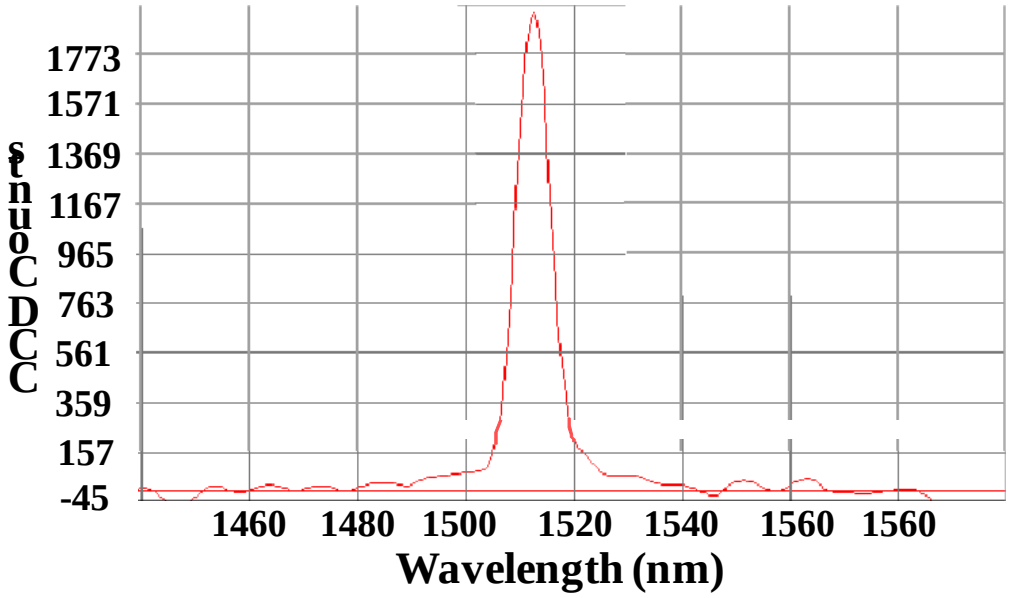
Counts
1773
1571
1369
1167
965
763
561
359
157
-45
1460
1480
1500
1520
1540
1560
1560
Wavelength (nm)

(b)

Fig. 5.8. Experiment curve for (a) output power vs. current for the micro loop laser and (b) lasing spectrum measured by fiber spectrometer with 5nm resolution.

5.4 Summary

We have described a novel microcavity laser structure with use of MLMs as high reflectors, enabling linear geometry. A widened gain medium (WGM) facilitates higher output power. FDTD simulation is used to examine the mirror loss and simulate the laser operation, showing that a cavity length of <25μm is achievable. Initial fabrication and testing result of the MLM-WGM laser is presented. Quantum Well Intermixing is used to optimize the microlasers by engineering small active area joint with the passive area without disjoint.

CHAPTER VI SUPER HIGH NUMERICAL APERTURE MULTI-LAYER GRIN (Super-GRIN) lens

6.1 Introduction

In chapter IV and V we discussed several types of nanophotonic devices with potential application in the nano-OEIC. They utilize waveguides with increasingly smaller dimensions to increase integration density; the vertical dimension of such waveguides can approach λ/(2n) (λ=free-space wavelength) or about 0.3μm at λ=1.55μm for n=3.5 III-V semiconductors [95]. Even the conventional semiconductor lasers have vertical mode sizes as small as 1μm [96]. The horizontal beam spot sizes are usually larger and can be more easily transformed with tapered waveguides. In order to achieve high coupling efficiency between optical fiber and the on-chip devices, the coupling optics must be able to focus a collimated beam to submicron mode size vertically. Small spot sizes require optics with large NA as the diffraction-limited full-width-half-maximum (FWHM) focusing spot size d of an optical beam is given by $d = \lambda/(2 \cdot NA)$ [97], where λ is the free-space wavelength.

One way to achieve strong vertical focusing is to use a gradient-index (GRIN) lens. However, the conventional GRIN lens's performances are limited by the small refractive index difference Δn achievable via typical fabrication techniques such as chemical vapor deposition,

ion exchange, and crystal growing (maximum Δn~0.15, NA~0.5) [98-100]. In this chapter, we show that a GRIN lens with very high Δn giving NA>1.5 can be realized by depositing thin films of two or more materials with high refractive index difference alternatively with variation in thickness ratio to achieve an effective variation in the refractive index, which we refer to as super high numerical aperture multi-layer GRIN (Super-GRIN) lens. In this Chapter, we discuss the design procedures for the Super-GRIN lens and the simulation results showing strong lens focusing. The numerical simulation is based on finite-difference time-domain (FDTD) method that solves Maxwell's Equations spatial-temporally without additional approximations [101].

6.2 Design Theory

To construct a Super-GRIN lens with an approximate parabolic refractive index profile as shown by the dashed line in Fig. 6.1(a), the design procedures are as follows: first, the parabolic profile is replaced by step refractive index profile as shown by the solid line in Fig. 6.1(a). Next, each step refractive index n_{step} region is broken down into a few periods of mixing one high refractive index (n_1) material with thickness L_1 and one low refractive index (n_2) material with thickness L_2, as shown by Fig. 6.1(b), according to the approximate formula:

$$n_{step} = (n_1 L_1 + n_2 L_2)/(L_1 + L_2). \tag{6.1}$$

By varying the ratio/thickness of these two materials, any n_{step} value in between can be achieved. For a ¼ pitch length GRIN lens with continuous parabolic index profile $n^2(x) = n_0^2(1 - \frac{n_0^2 - n_R^2}{n_0^2} \cdot \frac{x^2}{D^2})$, the NA is given by $NA_{con} = dn \equiv \sqrt{n_0^2 - n_R^2}$ [102], where n_0, n_R

are the respective refractive indices at the center and edge of the GRIN, *x* is the distance from the axis and *D* is the half width of the GRIN (note $dn \neq \Delta n \equiv n_0 - n_R$). To achieve sub-micron spot size, we need to have a lens with Δn at least 0.19 for λ=1.55μm, assuming n_R=1.5. For illustrative purpose, we take the refractive index of the two materials to be n_1=2.35 and n_2=1.45 (realizable by TiO_2 and SiO_2). Ideally this can give Δn as high as 0.9 (NA=1.85), resulting in potential focusing spot size of 0.42 μm at wavelength λ=1.55μm.

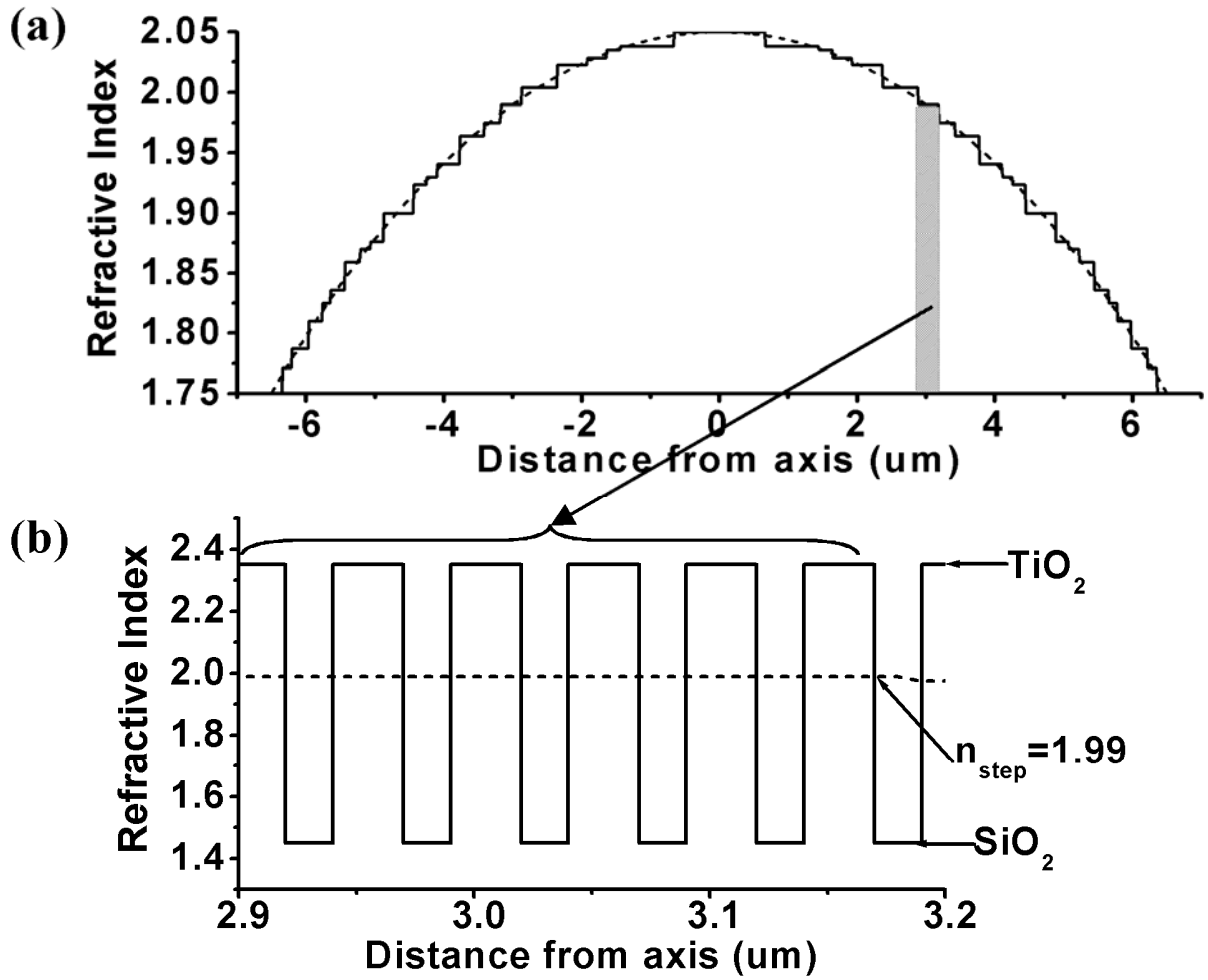

Fig. 6.1 (a) The parabolic refractive index profile (dashed line) of a 13μm thick GRIN lens and the approximate step refractive index profile of a Super-GRIN lens (solid line), (b) TiO_2 and SiO_2 layers (solid line) used to approximate a certain step refractive index (dashed line).

From Eq. (6.1) we can see that for the given two materials, the maximum Δn achievable is dependent on the maximum film-thickness ratio. The minimum layer thickness is limited by the current thin film deposition technology while the maximum film thickness is limited by the scattering loss at layer interfaces. Material absorption is neglected due to the small lens size. Current thin film deposition process has thickness control accuracy of 1nm or better. In order to achieve fabricated film thickness error within 5% of the targeted value for example, the minimum thickness L_{MIN} of each layer shall be 20nm, which will be the value used in our design below.

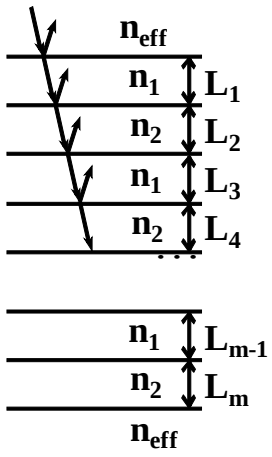

(a)

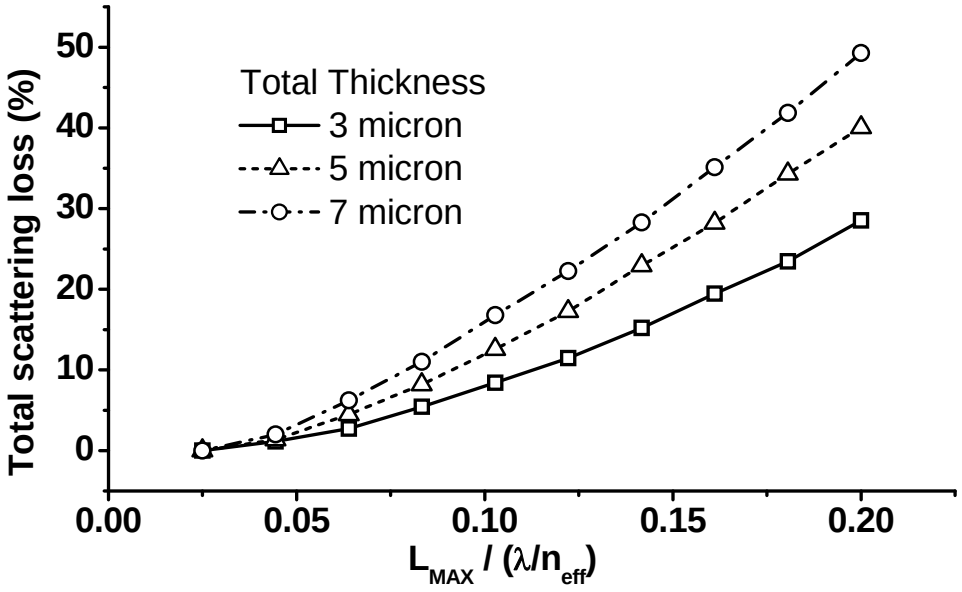

(b)

Fig. 6.2 (a) Layer structure used in estimation of the scattering loss using transfer matrix method. (b) Total scattering loss calculated by transfer matrix method for three total structure thickness: 3μm (straight line), 5μm (dotted line), and 7μm (dashed-dotted line).

The maximum film thickness L_{MAX} is restricted by the scattering loss at layer interfaces. Scattering loss in multilayer thin films arises mainly from refractive index fluctuation in the structure. The scattering loss in the Super-GRIN lens is dependent on the actual film structure, which will be shown below for specific cases. For design purpose, it is useful to obtain upper bound estimation on the scattering loss dependence of L_{MAX}. We consider the worst-case scenario where the thickness of each thin film layer L_i (Fig. 6.2(a)) is a random value uniformly distributed between L_{MIN} and L_{MAX}. The total scattering loss is calculated by transfer matrix

method [103]. The refractive indices at incident and exit plane are matched to the effective refractive index n_{eff} in the center so the Fabry-Perot resonance effect caused by the slab boundaries is eliminated. The total reflection will then all come from the scattering within the slab. Fig. 6.2(b) shows the calculated scattering loss from 3, 5, and 7μm structure with normal incident plane wave at λ=1.55μm. Each data point is obtained by averaging the results over 2000 random structures. To get loss less than 10% for the case of focusing fiber mode in a 10μm thick structure with 5μm vertical propagation, L_{MAX} should be less than 10% of λ/n_{eff}, which means L_{MAX}=80nm.

6.3 Simulation

Below, we will use FDTD method to study some specific Super-GRIN lens design. Based on the analysis above, we first construct a Super-GRIN lens structure using ~300 layers of TiO_2 and SiO_2 with carefully designed thickness from 20-80nm for the case of an approximate parabolic index profile with n_0=2.05 and n_R =1.75 (NA=1.1) as shown in Fig. 6.1. The total thickness of the lens is 13μm, large enough for 8μm fiber mode.

The TE light propagating inside a continuous parabolic refractive index profile GRIN lens (Fig. 6.3(a)) with the above n_0 and n_R value is compared to the Super-GRIN (Fig. 6.3(b)), where λ=1.55μm optical mode from a single mode fiber is launched into both structures. The snapshot is taken at a time when light propagates slightly longer than ¼ pitch length. We can see that the Super-GRIN from the two-material system has behavior almost identical to a continuous index GRIN lens. The ¼ pitch length is ~18μm, making the lens very compact. The

corresponding TM light propagating inside the Super-GRIN lens is shown in Fig. 6.3(c). The Super-GRIN lens shows very little difference in TE/TM focusing behavior. The focused spot size at ¼ pitch point is compared to an optical waveguide mode in Fig. 6.3(d). The Super-GRIN lens focusing spot size has FWHM ~0.7μm, close to the estimation of $d=\lambda/(2NA_{con})$, with $NA=NA_{con}$ given by the continuous GRIN lens formula.

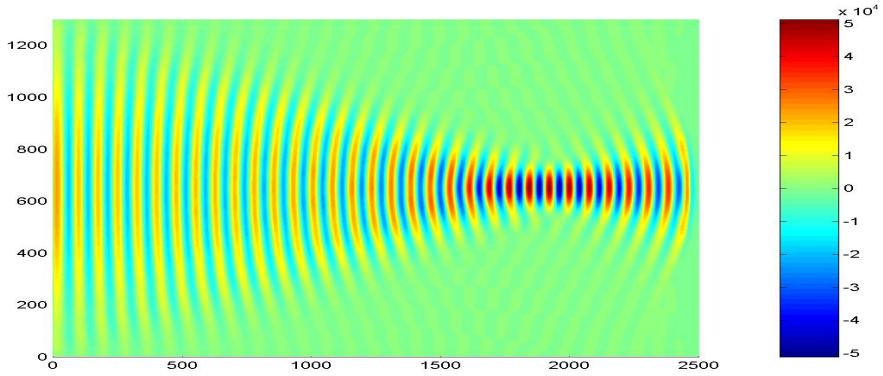

(a)

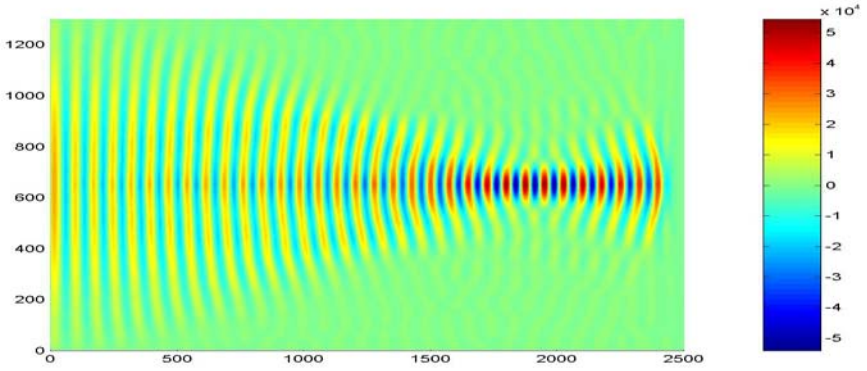

(b)

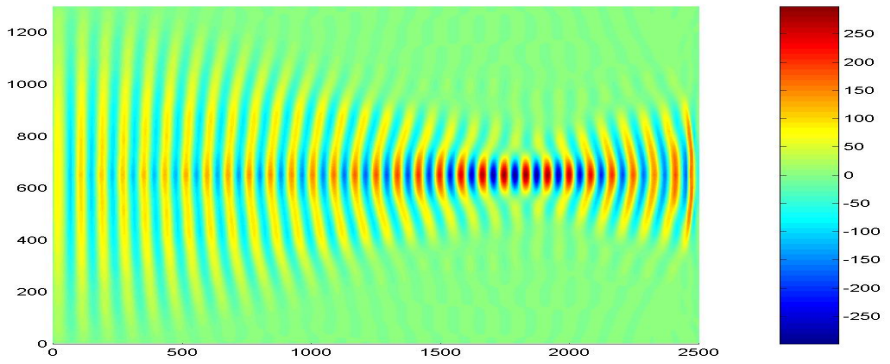

(c)

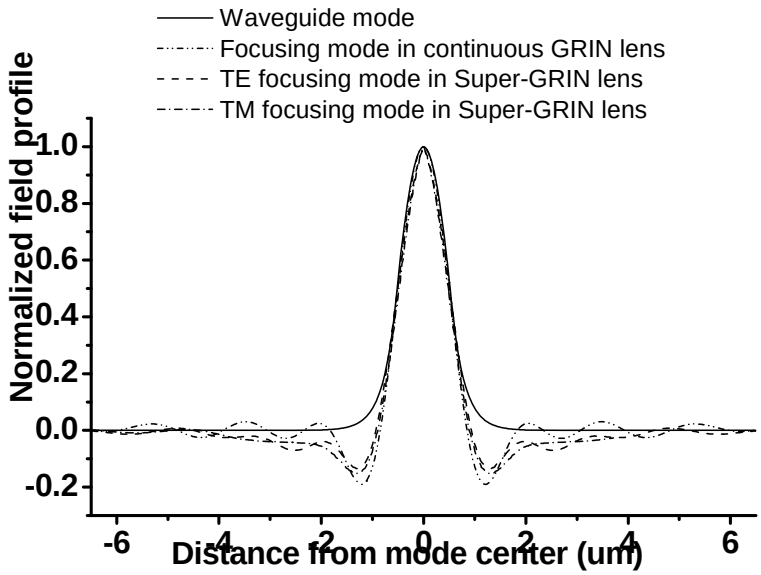

(d)

Fig. 6.3 FDTD simulated field pattern for fiber mode propagating inside lenses (vertical size (V) 13μm, horizontal size (H) 25μm), (a) TE light (E field) in the continuous index GRIN lens, (b) TE light (E field) in the Super-GRIN lens with TiO_2 / SiO_2, (c) TM light (H field) in the Super-

GRIN lens with TiO_2 / SiO_2, (d) mode profile at the focusing point of the Super-GRIN lens and continuous GRIN lens, compared to mode profile of the matched III-V waveguide (core thickness 1.1μm, core / cladding refractive index 3 / 2.8).

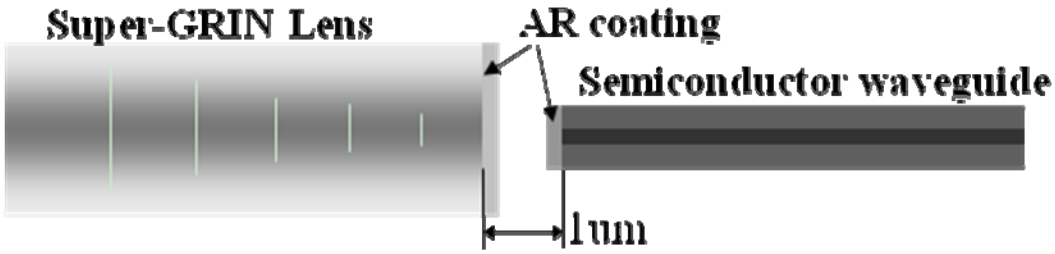

(a)

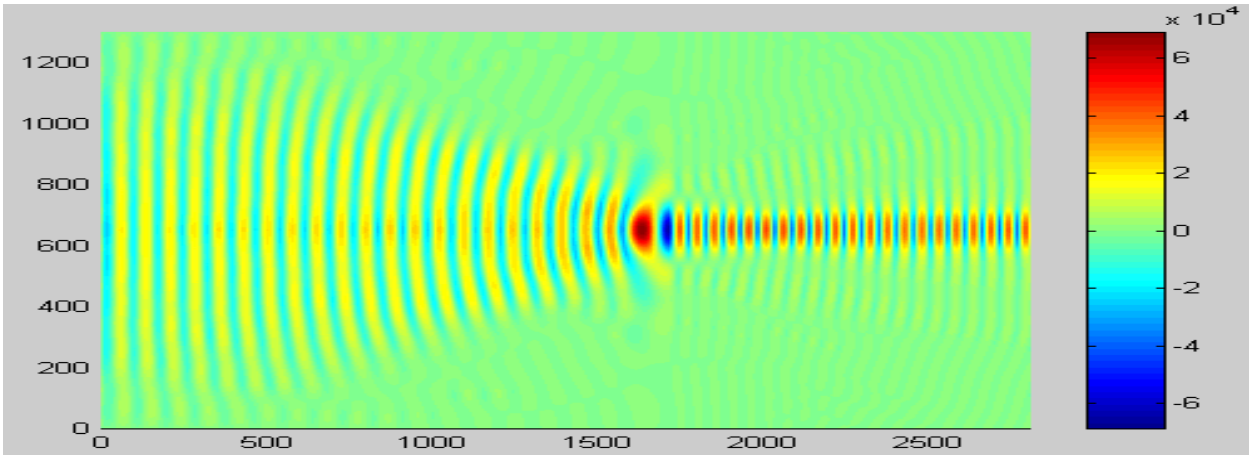

(b)

Fig. 6.4 Focusing in Super-GRIN lens from optical fiber mode to III-V waveguide with air gap and AR coating, (a) structure, (b) FDTD simulated TE light E-field pattern (V×H=13μm×28μm).

To act as a focusing lens from optical fiber to III-V semiconductor waveguide, the facet of the Super-GRIN lens should not touch the waveguide; we shorten the length of the lens by ~1μm to slightly less than ¼ pitch so the focusing point will be outside the lens. AR coating is added to both the lens facet and the waveguide facet to avoid Fresnel mismatch. The configuration and FDTD simulated field pattern is illustrated in Fig. 6.4. Both the input energy from the fiber and the output energy from the waveguide are collected numerically. The result shows that 95.3% of the input energy is coupled into the waveguide. In comparison, a continuous-index GRIN with identical configuration has 97.7% coupling efficiency. The two-material system only introduces 2.4% additional loss.

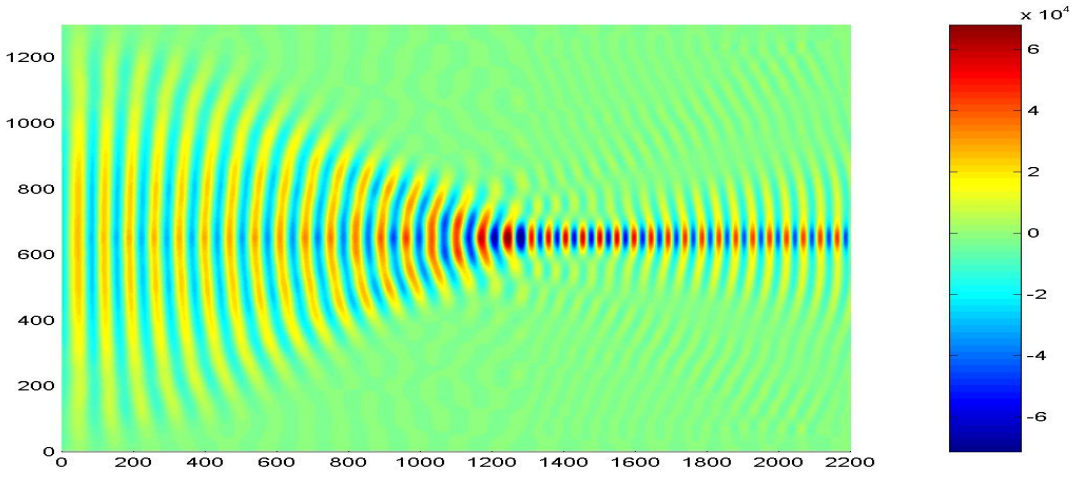

(a)

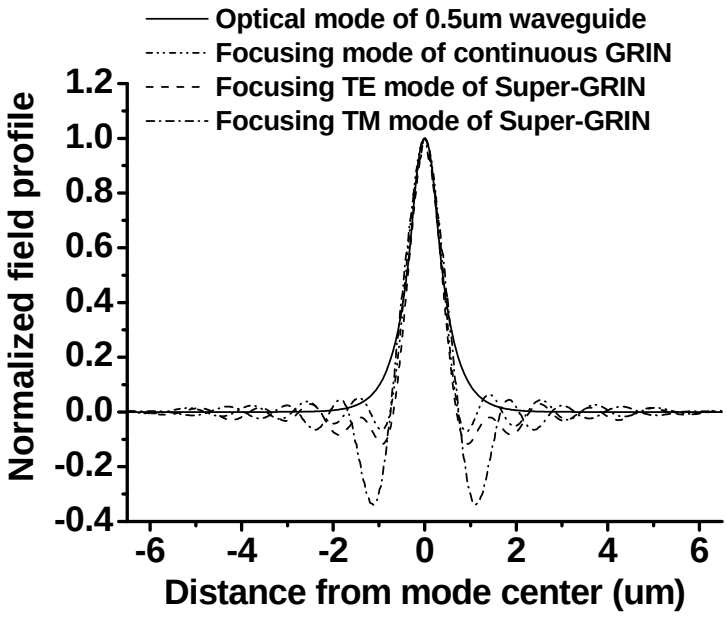

(b)

Fig. 6.5 FDTD simulation of a Super-GRIN lens with n_R=1.45 and n_0=2.17. (a) Simulated TE light E-field pattern (V×H=13μm×22μm) showing optical fiber mode focused to 0.5μm III-V waveguide (core/cladding refractive index 3.35 / 3.2, core thickness 0.5μm). (b) Mode profile at the focusing point of the Super-GRIN lens and continuous GRIN lens, compared to mode profile of the matched III-V waveguide.

In order to reach even smaller spot size we simulated a Super-GRIN lens with n_R=1.45 (all SiO_2) and n_0=2.17 (SiO_2 20nm TiO_2 80nm), giving NA=1.6. The fiber mode is focused to a III-V waveguide with core thickness 0.5μm and core-cladding refractive index difference 3.35-3.2. The FWHM focused spot size is 0.53μm. The simulation result is shown in Fig. 6.5, where 89.5% of the fiber mode energy is coupled into the mode-matched nano-waveguide. In

comparison, a continuous-index GRIN with identical configuration has 92.2% coupling efficiency. The two-material system only introduces 2.7% additional loss compared to the continuous GRIN lens.

6.4 Conclusion

In conclusion, we have discussed the theory and design for a super-high numerical aperture multi-layer gradient index lens. We show that focusing spot size as small as 0.53μm and NA=1.6 (at λ=1.55μm) can be achieved potentially with TiO_2 / SiO_2 material system, which are materials widely used in DWDM thin film filters that have similar or more stringent thin-film deposition requirements. The employment of only two materials and thin film structure makes the scheme attractive in practical fabrication process. Other material systems with even higher Δn are possible as long as the required deposition and fabrication process exists. The scheme is versatile in that the multilayer deposition will allow arbitrary refractive index profiles to be employed, resulting in lenses capable of other wave front transformations. The examples discussed in here are for vertical focusing with planar deposition of thin films, either waveguide taper or etched cylindrical lens can be used to realize the focusing for the horizontal dimension. If coaxial deposition is possible, the same principle can be readily extended to 2-dimentional Super-GRIN lenses.

CHAPTER VII DISCUSSION AND FUTURE PLAN

7.1 Summary of Achievements

The main achievements of the thesis can be summarized as follows:

Firstly, we report a new computational model of material media capable of modeling the nanostructure and electronic dynamics of sophisticated active materials often needed in photonic device simulations. The media that can be modeled include solid-state and semiconductor type media, as well as molecular and atomic type media. This model is computationally efficient for incorporating into the FDTD electrodynamics simulation. The model is based on a multi-energy-level multi-electron quantum system in which the electron dynamics is governed by the Pauli Exclusion Principle and the dynamical Fermi-Dirac Thermalization. The medium is described by a set of rate equations derived quantum mechanically. The formulation is based on the basic minimal-coupling Hamiltonian extended to incorporate multiple electrons via second quantization using Fermion creation and annihilation operators. The set of rate equations and dipole equation describing the model are obtained without the usual rotating-wave approximations and can be applied to the regimes at near or far off-resonance as well as high field intensity. We show that the Fermi-Dirac thermalization can be incorporated via a temperature-dependent carrier hopping process, which mimics thermal carrier excitations. This dynamical process enables the simulation of carrier decay from non-thermal equilibrium after

excitation to a quasi equilibrium carrier distribution governed by the quasi Fermi-Dirac distribution. In application to semiconductor, this DTEQM-FDTD model takes into account the transient intraband and interband electron dynamics, the semiconductor band structure, and carrier thermal equilibrium process for the first time in FDTD simulation, and is referred to as the Dynamical-Semiconductor-Medium FDTD (DSM-FDTD) model. The DSM-FDTD model automatically incorporates energy-state filling effect. It also incorporates the typical nonlinear optical effects associated with carrier dynamics and thermally activated carrier scattering process under transient excitation spatial-temporally. The model also allows separate electron dynamics in the conduction and valence bands. These capabilities empower the model to treat sophisticated optoelectronic and nanophotonic devices having complex geometries with full spatial-temporal solutions at the microscopic level under electrical or optical excitation. A further extension of the FDTD model to include spatial diffusion of carriers, lattice temperature heating or cooling, and carrier dependent medium parameter shifts due to many-body effects will make it a highly powerful optoelectronic and photonic device simulator. Most importantly, we show that the FDTD model is sophisticated enough to incorporate the essential multi-physical effects in complex media and yet is simple enough to achieve fast computational time. We illustrated the application of this powerful new model to FDTD computation with the simulation of the entire gain and absorption spectra of a direct-bandgap semiconductor medium, showing the carrier band filling effects with Fermi-Dirac statistics. We then illustrated the application of the FDTD model to simulating spectral hole burning of carriers under a strong optical pulse with subsequent decay to thermal equilibrium representative of ultrafast phenomena in semiconductor. To illustrate its applications to photonic devices, we simulated a microdisk laser in which a

second lasing mode is excited due to gain bandwidth broadening at high medium excitation. We also show the shift in the lasing frequency with increased excitation due to carrier-induced refractive index change.

Secondly, we address the theory and simulation result for an all optical photonic transistor device based on gain and absorption manipulation of optical interference. The main problem currently impeding the realization of practical photonic transistor is that the physical scheme involved typically required either high optical power or long interaction length, resulting in Transistor Figure of Merits (F_{PT}) that is more than 100,000 times worse than that of electronic transistors. In chapter IV, we illustrated a new physical mechanism to realize photonic transistor action involving the use of optically-controlled gain and absorption to manipulate optical interference (GAMOI), resulting in highly-efficient all-optical operations that can be used to form photonic transistors with a wide variety of functionalities (switching, amplification, logical operation, λ conversion, pulse regeneration). The illustrated use of coupled waveguides is not the only choice as other multimode optical interference devices can also be used. Simulation of exemplary devices based on typical semiconductor medium show that the photonic transistors are capable of high speed of >100Gb/s, low signal operating power in the hundreds of μW range, low power consumption of a few mW, compact size of ten of micrometers, good signal amplification, and broad optical bandwidth, resulting in a Figure of Merits F_{PT} close to that of electronic transistors and more than 10^5 times higher than $\chi^{(3)}$ or $n^{(2)}$ approaches. The operating speed and gain can be pushed higher than what we illustrated here by using higher power for the power-supply beams. The operating power and speed performances are also dependant on the medium properties such as saturation power, which may be further engineered using quantum-

confined structures. Thus, the new device concept described and simulated here will enable various new possibilities for realizing multi-functional photonic transistors that are orders of magnitudes more efficient than current approaches, and are highly attractive. In addition, to achieve the optimal performance of the GAMOI based all-optical photonic transistors requires using a combination of 1^{st} order mode and 0^{th} order mode in the optical coupler. We also presented an ultra compact mode converter capable of the easy conversion between 0^{th} and 1^{st} order mode using sub micron optical waveguide. The design theory of the mode converter is discussed. The simulation result and the fabrication result of such mode converter are also presented. This is the first simulation and fabrication of mode converter based on the π phase shifted MZI to the best of the author's knowledge.

Next, we discussed a novel type of linear-geometry micro-cavity laser. The laser uses nano-scale waveguide loops as end reflectors to achieve single directional output. To the author's knowledge, this is the first laser with such design. The compact size and high reflectivity of the micro-loop mirror allows ultra-compact laser size, which leads to potential single mode operation. We show the simulation and fabrication result for microlaser with cavity length as small as 25mm. Method to obtain higher output power from the microlaser with widened gain medium (WGM) is discussed. Low lasing threshold of ~0.4 mA is achieved.

Lastly, one potential solution for the chip to optical fiber coupling in presented in Chapter VI. We proposed the first of its kind super-high numerical aperture gradient index (Super-GRIN) lens scheme using multiple thin layers of two or more materials with large refractive index contrast. The Super-GRIN lens could facilitate the coupling from nanophotonic devices to conventional optical stricture such as single mode fibers. Specific examples of the Super-GRIN

lens with SiO_2/TiO_2 material system designed for fiber coupling to nano-waveguide are shown to have focusing FWHM spot sizes of 0.53/0.7 μm at $\lambda = 1.55$ μm (corresponding to NA ~ 1.6/1.1) with 2.7/2.4% additional loss comparing to ideal continuous index profile GRIN lenses. Using the approach, Super-GRIN lens with NA>1.5 and length<20μm can be realized with current thin-film deposition technique.

7.2 Future Works

For each of the main focus area of the dissertation, various future works can be carried out.

For the current Dynamical-Semiconductor-Medium FDTD (DSM-FDTD) model, we can further extend the FDTD model to include the following. (1) Spatial diffusion of carriers, so carrier transportation process in nanophotonic devices can be better simulated. (2) Lattice temperature heating or cooling. The temperature T in the intraband relaxation rate equations describes the local crystal lattice temperature of the medium. Currently it is set to be equal to the environment temperature; however, if necessary it can be treated as a spatial-temporal parameter $T(\mathbf{r},t)$ determined separately by thermal diffusion equation. (3) Carrier dependent medium parameter shifts due to many-body effects. (4) Spontaneous emission noise simulation, so effect such as laser linewidth can be more accurately determined. All those extensions will make the model a highly powerful optoelectronic and photonic device simulator.

For the GAMOI based photonic transistors, it is shown by simulation that such a device can be readily fabricated using III-V semiconductor quantum well structure. The fabricated

device can be either tall structure or thin-film structure and the passive-active integration could be done by using quantum well intermixing technique. The initial simulation on quantum well intermixing resolution shows that theoretically the resolution should be enough to realize the proposed device; however, it will be wise to carry out experiment to determine the actual resolution of the passive / active interface first. After that the GAMOI based photonic transistor device can be fabricated and calibrated and the result can be compared to the simulation.

For the micro-loop laser, further optimization of the micro-loop mirror can be carried out. Other configurations with different waveguide dimension and bending radius can be fabricated to show the difference in reflectivity and mode quality. In the current fabricated laser, the output is collected from the top of the laser as both ends are high reflectors. In the future we can fabricate lasers with a coupler structure at one end to achieve optimal output efficiency.

For the Super-GRIN lens, We show that focusing spot size as small as 0.53μm and NA=1.6 (at λ=1.55μm) can be achieved potentially with TiO_2 / SiO_2 material system, which are materials widely used in DWDM thin film filters that have similar or more stringent thin-film deposition requirements. The employment of only two materials and thin film structure makes the scheme attractive in practical fabrication process. However, other material systems with even higher Δn are possible as long as the required deposition and fabrication process exists. The scheme is versatile in that the multilayer deposition will allow arbitrary refractive index profiles to be employed, resulting in lenses capable of other wave front transformations. The examples discussed in this dissertation are for vertical focusing with planar deposition of thin films. If

coaxial deposition of the films is possible, the same principle can be readily extended to 2-dimentional Super-GRIN lenses.

Reference

[1]. Y. Huang, G. Xu and S. T. Ho, An Ultracompact Optical Mode Order Converter, Photon. Tech. Lett., 18, 2281 (2006).

[2]. Y. Huang and S. T. Ho, Computational model of solid-state, molecular, or atomic media for FDTD simulation based on a multi-level multi-electron system governed by Pauli exclusion and Fermi-Dirac thermalization with application to semiconductor photonics, Opt. Express, 14, 3569 (2006).

[3]. Y. Huang, Y. Xiao, G. Xu, S. Chang, Y.-G. Zhao, R. Wang, B. S. Ooi, and S. T. Ho, A Single-Directional Micro-Cavity Laser with Micro Loop Mirrors and Widen Medium Realized with Quantum-well Intermixing, Photon. Tech. Lett. 18, 130 (2006).

[4]. Y. Huang and S. T. Ho, Super-High Numerical Aperture (NA>1.5) Micro GRIN Lens based on Dual-Material Approach, Optics Letters, 30, 1291 (2005).

[5]. Y. Huang and S. T. Ho, Simulation of Current-Injection and All-Optical Nanophotonic Semiconductor Devices with Multi-Level Multi-Electron FDTD Model, IEEE Nanotechnology Materials and Devices Conference, Korea, 2006.

[6]. Y. Huang and S. T. Ho, Ultrafast Bit and Byte addressing of All-Optical Memory based on Microring Resonators for Next-Generation Optical Networks, Asia Optical Fibe Communication & Optoelectronic Exposition & Conference, Shanghai, China, 2006.

[7]. Y. Huang and S. T. Ho, A Numerically Efficient Semiconductor Model with Fermi-Dirac Thermalization Dynamics (Band-Filling) for FDTD Simulation of Optoelectronic and Photonic Devices, QELS 2005.

[8]. Y. Huang, B. Liu, S. T. Ho, G. Xu, and B. S. Ooi, Quantum Well Saturation in Ultra Short Absorptive Waveguide Section Formed by Quantum Well Intermixing, CLEO 2005.

[9]. Y. Huang, Y. Xiao, G. Xu, S. T. Ho, Y. Zhao, C. Luo, J. Wang, and B. S. Ooi, Design and Fabrication of A Micro-Cavity Laser with Transparent Micro Loop Mirror, OFC 2005.

[10]. Joyner, C.H. Zirngibl, M. Meester, J.P. , A multifrequency waveguide grating laser by selective area epitaxy, Photonics Technology Letters, IEEE, Volume: 6, Issue: 11 page(s): 1277-1279, Nov. 1994.

[11]. Talneau, A; Bouadma, N; Lebellego, Y; Slempkes, S; Ougazzaden, A; Patriarche, G; Sermage, B, Low-damage dry-etched grating on an MQW active layer and dislocation-free InP regrowth for 1.55-mum complex-coupled DFB lasers fabrication, IEEE Photonics Technology Letters. Vol. 10, no. 8, pp. 1070-1072. Aug. 1998

[12]. V. Aimez, J. Beauvais, J. Beerens, D. Morris, H. S. Lim, and B. S. Ooi, “Low-energy ion-implantation-induced quantum-well intermixing”, IEEE J. Sel. Topics in Quantum Electron., vol. 8, pp. 870-879, 2002.

[13]. D. Y. Chu, M. K. Chin, S. Z. Xu, T. Y. Chang, and S. T. Ho, "1.5 μm InGaAs/InAlGaAs Quantum-Well Microdisk Lasers," IEEE Photonics Technol. Lett. 5, 1353-1355 (1993).

[14]. W. Fang, J. Y. Xu, A. Yamilov, H. Cao, Y. Ma, S. T. Ho, and G. S. Solomon, "Large Enhancement of Spontaneous Emission Rates of InAs Quantum Dots in GaAs Microdisks," Opt. Lett. 27, 948-950 (2002).

[15]. K. Inoue, K. Ohtaka, Photonic Crystals: Physics, Fabrication and Applications, Springer.

[16]. Y. Ma, G. Chang, S. J. Park, L. W. Wang, and S.T. Ho, ""InGaAsP Thin Film Microdisk Resonators Fabricated by Polymer Wafer Bonding for Wavelength Add-drop Filters"," IEEE Photonics Technology Letters, Vol 12 , No. 11, pp. 1495 (2000).

[17]. K. S. Yee, “Numerical Solution of Initial Boundary Value Problems Involving Maxwell’s Equations in Isotropic Media,” IEEE Trans. Antennas Propag. 14, 302-307 (1966).

[18]. S. D. Gedney, "An anisotropic perfectly matched Layer-Absorbing Medium for the truncation of FDTD Lattice,” IEEE Trans. Antennas Propag. 44, 1630-1639 (1996), and references therein.

[19]. M. Okoniewski, M. Mrozowski, and M. A. Stuchly, “Simple treatment of multi-term dispersion in FDTD,” IEEE Microwave Guid. Wave Lett. 7, 121-123 (1997), and references therein.

[20]. A. S. Nagra and R. A. York, “FDTD Analysis of Wave Propagation in Nonlinear Absorbing and Gain Media,” IEEE Trans. Antennas Propag. 46, 334-340 (1998).

[21]. Y. Huang, “Simulation of Semiconductor Material Using FDTD Method”, Master Thesis, Northwestern University, June 2002. https://depot.northwestern.edu/yhu234/publish/YYHMS.pdf

[22]. S. Chang, Y. Huang, G. Chang, and S. T. Ho, “THz All-Optical Shutter based on Semiconductor transparency switching by two Optical -pulses”, OSA Annual Meeting, TuY3, Long Beach, CA, 2001.

[23]. S. T. Ho, research notes, 1998-1999.

[24]. Y. Huang, “Simulation of Semiconductor Structure Using FDTD Method”, presented to the Physics Department at Northwestern University, 15 Jan. 2002.

[25]. W. W. Chow, S. Koch, and M. Sargent III, Semiconductor-Laser Physics, Springer Verlag, Berlin, 1994.

[26]. J. Piprek, Optoelectronic Devices: Advanced Simulation and Analysis, Springer Verlag, New York, 2005.

[27]. S. Park, "Development of InGaAsP/InP Single-mode Lasers Using Microring Resonators for Photonic Integrated Circuits", PhD Thesis, Northwestern University, Dec. 2000, and references therein.

[28]. Y. Huang and S. T. Ho, “A numerically efficient semiconductor model with Fermi-Dirac thermalization dynamics (band-filling) for FDTD simulation of optoelectronic and photonic devices,” 2005 Technical Digest of the Annual Conference on Lasers and Electro-Optics, Paper QTuD7, Baltimore, MD, May 2005.

[29]. S. T. Ho, P. Kumar, and J. H. Shapiro, "Quantum Theory of Nondegenerate Multiwave Mixing (I) - General Formulation," Phys. Rev. A 37, 2017-2032 (1988).

[30]. S. T. Ho and P. Kumar, "Quantum Optics in a Dielectric: Macroscopic Electromagnetic-Field and Medium Operators for a Linear Dispersive Lossy Medium - A Microscopic Derivation of the Operators and their Commutation Relations," J. Opt. Soc. Am. B 10, 1620-1636 (1993).

[31]. S. T. Ho, P. Kumar, and J. H. Shapiro, "Vector-Field Quantum Model of Degenerate Four-Wave Mixing," Phys. Rev. A 34, 293-303 (July 1986).

[32]. J. J. Sakurai, Advanced Quantum Mechanics, Addison Wesley, 1967.

[33]. in semiconductor corresponds to the spatially localized operator .

[34]. William H. Louisell, Quantum Statistical Properties of Radiation, Wiley-Interscience, New York, 1990.

[35]. For example, if three upper levels can decay to a single ground level, then each upper level will be associated with a transition dipole so that the total number of dipoles involved will be three, which is equal to the number of the upper levels.

[36]. R. F. Kazarinov, C.H. Henry, and R. A. Logan, “Longitudinal mode self-stabilization in semicondcutor lasers”, J. Appl. Phys. 53, 4631-4644 (1982).

[37]. S. Marrin, B. Deveaud, F. Clerot, K. Fuliwara, and K. Mitsunaga, “Capture of Photoexcited Carriers in a Single Quantum Well with Different Confinement Structures,” IEEE J. Quantum Electron. 27, 1669-1675 (1991).

[38]. L. A. Coldren and S. W. Corzine, Diode lasers and photonic integrated circuits, Wiley, John & Sons. 1995.

[39]. J. L. Oudar, D. Hulin, A. Migus, A. Antonetti, and F. Alexandre, “Subpicosecond spectral hole burning due to nonthermalized photoexcited carriers in GaAs,” Phys. Rev. Lett. 55, 2074-2077 (1985).

[40]. D. Y. Chu, M. K. Chin, S. Z. Xu, T. Y. Chang, and S. T. Ho, "1.5 μm InGaAs/InAlGaAs Quantum-Well Microdisk Lasers," IEEE Photonics Technol. Lett. 5, 1353-1355 (1993).

[41]. W. Fang, J. Y. Xu, A. Yamilov, H. Cao, Y. Ma, S. T. Ho, and G. S. Solomon, "Large Enhancement of Spontaneous Emission Rates of InAs Quantum Dots in GaAs Microdisks," Opt. Lett. 27, 948-950 (2002).

[42]. J. P. Zhang, D. Y. Chu, S. L. Wu, W. G. Bi, R. C. Tiberio, C. W. Tu, and S. T. Ho, "Photonic-Wire Laser," Phys. Rev. Lett. 75, 2678-2681 (1995).

[43]. Georgios I. Papadimitriou, Chrisoula Papazoglou, and Andreas S. Pomportsis, “Optical Switching: Switch Fabrics, Techniques, and Architectures”, Journal of Lightwave Technology, Vol.21, No.2, pp384-403, Feb. 2003.

[44]. S. T. Ho, C. E. Soccolich, W. S. Hobson, A. F. J. Levi, M. N. Islam, and R. E. Slusher, "Large Nonlinear Phase Shifts in Low-Loss AlXGa1-XAs Waveguides Near Half-Gap," App. Phys. Lett. 59, 2558-2560 (1991).

[45]. R. P. Espindola, M. K. Udo, D. Y. Chu, S. L. Wu, R. C. Tiberio, P. F. Chapman, D. Cohen, and S. T. Ho, "All-Optical Switching with Low-Peak Power in Microfabricated AlGaAs Waveguides," IEEE Photon. Tech. Lett., 7, 641-643 (1995).

[46]. Y.-H. Kao, T. J. Xia, M. N. Islam, and G. Raybon, "Limitations on ultrafast optical switching in a semiconductor laser amplifier operating at transparency current," J. Appl. Phys. 86, 4740-4747 (1999).

[47]. B. Dagens, C. Janz, D. Leclerc, V. Verdrager, F. Poingt, I. Guillemot, F. Gaborit, and D. Ottenw¨alder, "Design Optimization of All-Active Mach–Zehnder Wavelength Converters," IEEE Photon. Tech. Lett. 11, 424-426 (1999).

[48]. M.L. Ma˘sanovic´, V. Lal, J. S. Barton, E. J. Skogen, L. A. Coldren, and D. J. Blumenthal, "Monolithically Integrated Mach–Zehnder Interferometer Wavelength Converter and Widely Tunable Laser in InP," IEEE Photon. Tech. Lett. 15, 1117-1119 (2003).

[49]. D. Cotter et al., "Nonlinear Optics for High-Speed Digital Information Processing," Science, 286, 1523-1528 (1999).

[50]. S.M. Jensen, "The nonlinear coherent coupler," IEEE J. Quantum Electron. QE-18, 1568-1571 (1982).

[51]. C.C.Yang, all-optical ultrafast logic gates that use asymmetric nonlinear directional couplers, Optical Letters, Vol. 16, No. 21, November 1991. pp 1641-1643

[52]. J. C. Campbell, F. A. Blum, D. W. Shaw, and K. L. Lawley, GaAs electro-optic directional-coupler switch, Applied Physics Letters, Vol. 27, No. 4, 202-204, August 1975.

[53]. G. H. B. Thompson, "Analysis of Optical Direction Couplers that Include Gain or Loss and Their Application to Semiconductor Slab Dielectric Guides", Journal of Lightwave Technology, Vol. LT-4, No. 11, 1986, 1678-1693

[54]. Amnon Yariv, Optical Electronics in Modern Communications, 5th edition, Oxford University Press, New York, 1997.

[55]. Terji Durhuus, Benny Mikkelsen, Carsten Joergensen, Soeren Lykke Danielsen, and Kristian E. Stubkjaer, "All-Optical Wavelength Conversion by Semiconductor Optical Amplifiers", Journal of Lightwave Technology, Vol.14, No.6, pp942-954, Dec.1996.

[56]. W.Idler, K. Daub, G.Laube, M. Schiling, P. Wiedemann, K. Dutting, M. Klenk, E. Lach, and K.Wunstel, "10 Gb/s Wavelength Conversion with Integrated Multiquantum-Well-Based 3-Port Mach-Zehnder Interferometer", IEEE Photonics Technology Letters, Vol.8, No.9, pp1163-1165, Sept. 1996

[57]. C. Joergensen, S.L. Danielsen, T.Durhuus, B. Mikkelsen, K.E. Stubkjaer, N.Vodldani, F.Ratovelomanana, A. Enard, G.Glastre, D.Rondi, and R. Blondeau, "Wavelength Conversion by Optimized Monolithic Integrated Mach-Zenhder Interferometer", IEEE Photonics Technology Letters, Vol.8, No.4, pp521-523, April. 1996

[58]. M.D.Vaughn and D.J. Blumenthal, "All-Optical Updating of Subcarrier Encoded Packet Headers with Simultaneous Wavelength Conversion of Baseband payload in Semiconductor Optical Amplifiers", IEEE Photonics Technology Letters, Vol.9, No.6, pp827-829, June 1997

[59]. B. Dagens, C. Janz, etc. "Design optimization of all active MZ wavelength converter", IEEE Photo. Tech. Lett. Vol. 11, No. 4, (1999) p424-426.

[60]. S. P. Majumder, etc. "Performance analysis of an all-optical wavelength converter based on XPM in semiconductor optical amplifiers", Optics & Laser Technology, 35(2003) 261-265.

[61]. R. J. manning and G. Sherlock, “Recovery of a phase shift in ~12.5 ps in a semiconductor laser amplifier”, Electronics Letters, Vol. 31 No. 4, 307-308

[62]. Liu Xianbing, and Ye Peida, “Analysis of TOAD switching characteristics considering the gain and phase response of a semiconductor optical amplifier to control pulses”, microwave and optical technology letters, Vol. 24, No.6, March 2000, p374-377.

[63]. Michael G. Kane, Ivan Glesk, Jason P. Sokoloff, and Paul R. Prucnal, “Asymmetric optical loop mirror: analysis of an all-optical switch”, Applied optics, Vol. 33, No. 29, Oct. 1994, p6833-6841

[64]. K.I. Kang, T. G. Chang, I. Glesk, and P. R. Prucnal, “Demonstration of ultrafast, all-optical, low control energy, single wavelength, polarization independent, cascadable, and integratable switch”, APL, 67(5), July 1995, p605-607

[65]. Y.H.Kao, T.J.Xia, M.N Islam G. Raybon, “limitation on ultrafast optical switching in a SOA operating at transparency current”, JAP, 86(9). 4740-4747

[66]. R. P. Espindola, M. K. Udo, D. Y. Chu, S. L. Wu, R. C. Tiberio, P. F. Chapman, D. Cohen, and S. T. Ho, "All-Optical Switching with Low-Peak Power in Microfabricated AlGaAs Waveguides," IEEE Photonics Technology Letters, Volume 7, No. 6, pp. 641-643 (June 1995).

[67]. Shigeru Nakamura and Kazuhito Tajima, “Analysis of subpicosecond full switching with a symmetric Mach-Zehnder All-Optical switch”, Jpn. J. Appl. Phys. Vol. 35 (1996), p1426-1429.

[68]. K. Tajima, S. Nakamura, and Y. Sugimoto, “Ultrafast polarization discriminating MZ all optical switch”, APL, 67(25),18, Dev 1995, p3709-3711

[69]. K. Tajima, “All-optical switch with switch-off time unrestricted by carrier lifetime”, Jpn. J. Appl. Physics. Vol 32, (1993) p. L 1746-1749

[70]. Shigeru Nakamura, Yoshiyasu Ueno, and Kazuhito Tajima, “Ultrafast (200-fs switching, 1.5-Tb/s demultiplexing) and high repetition (10GHz) operation of a polarization discriminating symmetric MZ all optical switch”, IEEE photonics technology letters, Vol. 10, 11 Nov. 1998 p. L 1575-1577

[71]. P. Bai et al., “A 65nm Logic Technology Featuring 35nm Gate Lengths, Enhanced Channel Strain, 8 Cu Interconnect Layers, Low-k ILD and 0.57 μm2 SRAM Cell,” Technical Digest of the 2004 International Electron Devices Meeting, San Francisco, 657 (2004).

[72]. Brian R. Bennett, etc., carrier-induced change in refractive index of InP, GaAs and InGaAsP, IEEE Journal of Quantum Electronics, Vol. 26, No. 1, 1990, pp 113-122.

[73]. Byung-Tak Lee and Sang-Yung Shin, “Mode-order converter in a multimode waveguide”, Optics Letters, vol. 28, No. 18, pp. 1660-1662, 2003.

[74]. A. A. Ishaaya, etc, “Conversion of a high-order mode beam into nearly Gaussian beam by use of a single interferometric element”, Optics Letters, vol. 28, No. 7, pp. 504-506, 2003.

[75]. Y. Ma, S. J. Park, L. W. Wang, and S. T. Ho, " "Ultracompact multimode Interference 3-dB coupler with strong lateral confinement by deep dry etching"," IEEE Photonics Technology Letters, vol. 12, no. 5, pp. 492-494, 2000.

[76]. Sean L. Rommel,etc, “Effect of H2 on the etch profile of InP/InGaAsP alloys in Cl2:Ar:H2 inductively coupled plasma reactive ion etching chemistries for photonic device fabrication”, J. Vac. Sci. Technol. B, vol. 20, no. 4, pp. 1327-1330, 2002.

[77]. J. P. Zhang, D. Y. Chu, S. L. Wu, W. G. Bi, R. C. Tiberio, C. W. Tu, and S. T. Ho, "Directional Light Output from Photonic-Wire Lasers," IEEE Photon. Technol. Lett., vol. 8, no. 8, pp. 968–970, Aug. 1996.

[78]. J. P. Zhang, D. Y. Chu, S. L. Wu, W. G. Bi, R. C. Tiberio, R. M. Joseph, A. Taflove, C. W. Tu, and S. T. Ho, "Nanofabrication of 1-D Photonic Bandgap Structures Along Photonic Wire," IEEE Photon. Technol. Lett., vol. 8, no. 4, pp. 491-493, Apr. 1996.

[79]. J. P. Zhang, D. Y. Chu, S. L. Wu, W. G. Bi, R. C. Tiberio, C. W. Tu, and S. T. Ho, "Photonic-Wire Laser," Phys. Rev. Lett., vol. 75, no. 14, pp. 2678-2681, Oct. 1995.

[80]. D. Y. Chu, M. K. Chin, S. Z. Xu, T. Y. Chang, and S. T. Ho, "1.5 μm InGaAs/InAlGaAs Quantum-Well Microdisk Lasers," IEEE Photon. Technol. Lett., vol 5, no. 12, pp. 1353-1355, Dec. 1993.

[81]. K. Shin, M. Tamura, A. Kasukawa, N. Serizawa, S. Kurihashi, S. Tamura, and S. Arai, “Low threshold current density operation of GaInAsP-InP laser with multiple reflector microcavities,” IEEE Photon. Technol. Lett., vol. 7, pp. 1119–1121, Oct. 1995.

[82]. T. Baba, M. Hamasaki, N. Watanabe, P. Kaewplung, A. Matsutani, T. Mukaihara, F. Koyama, and K. Iga, “A novel short-cavity laser with deep-grating distributed Bragg reflectors,” Jpn. J. Appl. Phys., vol. 35, no. 2b, pp. 1390–1394, 1996.

[83]. Y. Yuan, T. Brock, P. Bhattacharya, C. Caneau, and R. Bhat, “Edge emitting lasers with short-period semiconductor/air distributed Bragg reflector mirrors,” IEEE Photon. Technol. Lett., vol. 9, pp. 881–883, July 1997.

[84]. E. H. of ling, R. Werner, F. Sch¨afer, J. P. Reithmaier, and A. Forchel, “Short-cavity edge-emitting lasers with deeply etched distributed Bragg reflectors,” Electron. Lett., vol. 35, no. 2, pp. 154–155, 1999.

[85]. T. Mukaihara, N. Yamanaka, N. Iwai, T. Ishikawa, and A. Kasukawa, “1.3 m GaInAsP lasers integrated with butt-coupled waveguide and high reflective semiconductor/air Bragg reflector (SABAR),” Electron. Lett., vol. 34, no. 9, pp. 882–884, 1998.

[86]. Y. Huang, Y. Xiao, G. Xu, S. T. Ho, Y. Zhao, C. Luo, J. Wang, and B. S. Ooi, “Design and Fabrication of a Micro-Cavity Laser with Transparent Micro Loop Mirror,” presented at the OFC conference, Anaheim, CA, USA, 2005.

[87]. K. S. Yee, “Numerical solution for initial boundary value problems involving Maxwell’s equations in isotropic media,” IEEE Trans. Antennas and Propagation, vol. 41, pp. 302-307, 1966.

[88]. M. K. Chin, C. Youtsey, W. Zhao, T. Pierson, S. L. Wu, Z. Ren, and S. T. Ho, "Ultra-Compact Directional Couplers and Race-Track Microcavity Resonators as Building Blocks for WDM Devices," Conference on Lasers and Electro-Optics, CPD22/1, 1999.

[89]. Y. Huang, “Simulation of Semiconductor Material Using FDTD Method”, Master Thesis, Northwestern University, June 2002. https://depot.northwestern.edu/yhu234/publish/YYHMS.pdf.

[90]. S. Chang, Y. Huang, G. Chang, and S. T. Ho, “THz All-Optical Shutter based on Semiconductor transparency switching by two Optical -pulses”, OSA Annual Meeting, TuY3, Long Beach, CA, 2001.

[91]. S. T. Ho, research notes, 1998-1999.

[92]. Y. Huang, “Simulation of Semiconductor Structure Using FDTD Method”, presented to the Physics Department at Northwestern University, 15 Jan. 2002.

[93]. L. A. Coldren, and S. W. Corzine, Diode lasers and photonic integrated circuits. Wiley, John & Sons. 1995.

[94]. V. Aimez, J. Beauvais, J. Beerens, D. Morris, H. S. Lim, and B. S. Ooi, “Low-energy ion-implantation-induced quantum-well intermixing”, IEEE J. Sel. Topics in Quantum Electron., vol. 8, pp. 870-879, 2002.

[95]. J. P. Zhang, D. Y. Chu, S. L. Wu, W. G. Bi, R. C. Tiberio, C. W. Tu, and S. T. Ho, "Photonic-Wire Laser", Physical Review Letters, Volume 75, No. 14, pp. 2678-2681 (October 1995).

[96]. A. Yariv, Optical Electronics in Modern Communications (New York: Oxford, 1997).

[97]. K. Iga, “Theory for gradient-index imaging,” Applied Optics, vol. 19, April 1980, pp. 1039–1043.

[98]. D. T. Moore, “Gradient-index optics: a review,” Applied Optics, vol. 19, April 1980, pp. 1035–1038.

[99]. J. E. Samuels and D. T. Moore “Gradient-index profile control from mixed molten salt baths”, Applied Optics, 29 (1990) 4042-50.

[100]. B. Messerschmidt, U. Possner, A. Pfeil, and T. Possner, “Diffraction-limited gradient-index (GRIN) microlenses with high numerical apertures produced by silver ion exchange in glass: diffusion modeling and process optimization”, in Inorganic Optical Materials, Proc. SPIE 3424, 88-96 (1998).

[101]. K. S. Yee, “Numerical solution for initial boundary value problems involving Maxwell’s equations in isotropic media,” IEEE Trans. Antennas and Propagation, vol. 41, 1966, pp. 302-307.

[102]. C. Gomez-Reino, M.V. Perez, and C. Bao, Gradient-Index Optics: Fundamentals and Applications (Springer, 2002).

[103]. D. Rafizadeh, and S. T. Ho, "Numerical analysis of vectorial wave propagation in waveguides with arbitrary refractive index profiles" Optics Communications, Vol. 141, pp. 17-20 (August 1997).